TECHNISCHE UNIVERSITÄT WIEN

DISSERTATION

Experiments with momentum-correlated atom pairs trapped in a double-well potential

von

Dott. Mag. Filippo Borselli

[redacted]

ausgeführt zum Zwecke der Erlangung des akademischen Grades eines

Doktors der Naturwissenschaften

unter der Leitung von

Univ.-Prof. Dipl.-Ing. Dr. techn. Hannes-Jörg Schmiedmayer

E141, Atominstitut

eingereicht an der

Technischen Universität Wien

Fakultät für Physik

Vienna, May 2022

Filippo Borselli

Gutachter:

H.-J. Schmiedmayer

A. Smerzi

P. Walther

"L'inferno dei viventi non è qualcosa che sarà…è già qui, è quello che formiamo stando insieme tutti i giorni. Due modi ci sono per non soffrire. Il primo riesce facile a molti: accettare l'inferno e diventarne parte fino a non vederlo più. Il secondo è rischioso ed esige attenzione ed apprendimento continui: cercare e riconoscere chi e cosa in mezzo all'inferno, non è inferno, e farlo durare e dargli spazio."

Italo Calvino

"Wenn wir einen Menschen hassen, so hassen wir in seinem Bild etwas, was in uns selber sitzt. Was nicht in uns selber ist, das regt uns nicht auf."

Herman Hesse

Abstract

Since the discovery of Bose-Einstein condensation in 1995, many beautiful experiments have followed that have taken advantage of its macroscopical quantum properties. Different laboratories worldwide have achieved various goals, from purely theoretical and fundamental investigations to applications in metrology, quantum simulation of more complex systems, atom interferometry, and quantum information. Atom chip technology enables trapping Bose gases and creating versatile confining geometries: on the one hand, it provides a miniaturized circuit where low static currents can generate strong confining magnetic traps for cold atomic ensembles; on the other hand, a combination of static and oscillating currents can modify to a substantial degree the confining geometry, for example by creating a double-well configuration.

Nearly ten years ago, our group in Vienna transformed an optimally excited Bose gas into an atomic gun, shooting pairs of atoms moving in opposite directions along a single atom-waveguide potential created below the atom chip. These momentum-correlated pairs of atoms showed nearly zero atom-number squeezing between the two momenta modes demonstrating the highly correlated nature of the emission and were later referred to as twin-atom beams.

The fundamental idea motivating this project was: can we arrange the twin-atom emission to happen in a double-well configuration? And if that is so, can we then produce an atomic qubit in the double-well spatial degree of freedom? We show that, given our setup, the emitted double twin atoms are expected to be in a maximally entangled state of the double-well's left and right well states. Even though we cannot directly prove entanglement yet, we show that there is strong evidence for it. Firstly, we demonstrate the state inversion of a 1d Bose gas in a double-well potential for the first time and estimate the percentage of the transferred population by a fit of the observed final state evolution. Secondly, we characterize the emission with atom-number squeezing techniques and second-order correlation analysis. Both methods point to the generation of a maximally entangled state of two atoms, and, in particular, the second-order correlation analysis reveals the presence of two-particle interference effects.

Zusammenfassung

Seit der Entdeckung von Bose-Einstein Kondensation habe sich viele Experimente deren makroskopischen Quanteneigenschaften zunutze gemacht. Labore weltweit haben verschiedene Ziele erreicht, von rein theoretischen und grundlegenden Untersuchungen bis hin zu Anwendungen in der Metrologie, Quantensimulation komplexer Systeme, Atominterferometrie und Quanteninformation.
Die Atomchip-Technologie ermöglicht das Einfangen von Bose-Gasen und die Erzeugung flexibler Fallengeometrien: Einerseits stellt der Atomchip einen miniaturisierten Schaltkreis bereit, in dem niedrige statische Ströme starke einschließende magnetische Fallen für kalte atomare Ensembles erzeugen können; andererseits kann eine Kombination aus statischen und oszillierenden Strömen die Fallengeometrie in erheblichem Maße modifizieren, beispielsweise durch das Erzeugen eines Doppelmuldenpotentials.
Vor fast zehn Jahren verwandelte sich in unserer Gruppe in Wien ein optimal angeregtes Bose-Gas in eine Atomkanone, die Atompaare schoss, die sich in entgegengesetzte Richtungen entlang eines einzelnen Atom-Wellenleiter-Potentials bewegten, das unter dem Atomchip erzeugt wurde. Diese impulskorrelierten Atompaare zeigten gequetschte Atomzahlfluktuationen von nahezu null zwischen den beiden Impulsmoden, was die stark korrelierte Natur der Emission demonstriert, und wurden später als Zwillingsatomstrahlen bezeichnet.
Die grundlegende Idee, die dieses Projekt motivierte, war: Können wir die Zwillingsatomemission so anordnen, dass sie in einem doppelmuldenpotential stattfindet? Und wenn dem so ist, können wir dann ein atomares Qubit im räumlichen Freiheitsgrad des Doppelmuldenpotentials erzeugen? Wir zeigen, dass aufgrund unseres Aufbaus erwartet wird, dass sich die emittierten Doppelzwillingsatome in einem maximal verschränkten Zustand des linken und rechten Zustands des Dopplemuldenpotentials befinden. Auch wenn wir die Verschränkung noch nicht direkt beweisen können, zeigen wir, dass es starke Indizien dafür gibt. Wir demonstrieren zum ersten Mal die Zustandsumkehr eines 1d-Bose-Gases in einem Doppelmuldenpotential und schätzen den Prozentsatz der übertragenen Population durch Anpassung der beobachteten Endzustandsentwicklung ab. Des Weiteren charakterisieren wir die Emission mit Atomzahl-Squeezing-Techniken und Korrelationsanalysen zweiter Ordnung. Beide Methoden weisen auf die Erzeugung eines maximal verschränkten Zustands zweier Atome hin, und insbesondere die Korrelationsanalysen zweiter Ordnung offenbarten das Vorhandensein von Zwei-Teilchen-Interferenzeffekten.

Acknowledgments

This thesis work is the outcome of the years I spent as a Ph.D. student at the Atominstitut research facility in Vienna from September 2016 till March 2020 and then in a hybrid form, home-office and Atominstitut from March 2020 till May 2022. Very extraordinary things have happened around us during this time, which unfortunately will not be part of this research. This long time that I spent at the Atominstitut was shared with amazing colleagues and friends, both great physicists and human beings, from whom I learned a lot and spent the most valuable time together. The list of people I want to thank is huge, but I will here mention only some:

- Jörg Schmiedmayer for the trust he had and the opportunity he gave me to work in his international group, for sharing his fantastic physics intuition, and for letting us always go after the new ideas that eventually came up the way. His encouragement and curiosity were always of great inspiration to me.
- Marie Bonneau, without whom this adventure would not have started. She kindly replied to my email in the Summer of 2016, and this led to many important events in my life.
- Mira Maiwöger and Tom Astner for being the amazing buddies you are, helping me out in my ordinary life-or-death situations, the fluffy unicorns, the ATI cooking, and for all the "Ridicoloso" non-sense.
- Camille Lévêque for showing me how to embody the good old values, the friendship, the trust, the moral law and the french cheese. Merci for all those hiking, skiing, and climbing we shared, for always being there for me.
- Mohammadamin Tajik for the fruitful discussions on the Badner Bahn, on our way back home from the city center,
- Wenzel Kernsten for letting me practice German with him,
- João Sabino for teaching me portuguese and being the best nata to my pastel,
- Paranjape Pradyumna for the many Apfelstrudel and Buchteln in Café Hawelka,
- Kjeld Beeks for the lovely surprise on my 30th birthday during COVID-19's first wave,
- the old and new Rb2 team, Marie Bonneau, Rugway Wu, Marine Pigneur, Mira Maiwöger, Ferhat Loubar, Tiantian Zhang, Yevhenii Kuriatnikov, Maximilian Prüfer, for the science and the dedication to work, the endless electronic noise hunts, the vacuum leaks, the exchange of the dispensers and the bottom window, the teamwork, the team meetings, but also the lab music playlists and the successful BEC making.

- Grazie Federica, the first Italian I met when I arrived in Austria. Thanks for the initial help, the constant presence, the joy, the elegance, the culture, and, most importantly, your optimism.

- Marta, Claudia, Marco, Giulia, Francesco, Giulia C., and Florian for all the time we spent together in Vienna, the meals we shared, the parties, the victorious Euro cup, the fun, the car tours, everything.

  Lastly, I want to thank my wonderful family, my two loving parents, Paolo and Gianna, my two brothers, Tommaso and Giovanni, and my grandparents, Carlo, Lidiana, Renzo, and Anna. Without your unconditional love, life would be much harder.

Contents

List of Figures

Chapter 1

Introduction

Can we efficiently produce correlated pairs of atoms and, at the same time, envision an experimental configuration that allows quantum entanglement [1, 2]? Since the famous EPR paper of 1935 [3] and over the last many decades, several efforts were made into the generation of nonclassical states and investigation of their properties, since these states find application in fundamental research [4] and quantum technologies [5] as quantum-enhanced metrology [6–8], imaging [9], and quantum information and quantum communication [2, 10, 11].
While the photonic community has been researching nonclassical states of light and their applications for many decades, the interest has grown only recently among the atomic community. In particular, only a few groups working with Bose-Einstein condensates around the globe have devoted their ultracold gases machines to the generation and characterization of correlated pairs of atoms [12–17].
The fundamental idea at the basis of this thesis project stems from Ref. [18]. In this thesis work, we present an optimally excited one-dimensional Bose-Einstein condensate that becomes the source for an atom-laser of double twin-atom beams (DTBs), i.e., atom pairs highly correlated in their momenta along an atomic waveguide (twin atoms) that can be detected on either side of a double-well potential. The presence of the double waveguide has two advantages: on the one hand, it forces the emission to happen along the waveguide; hence it is more efficient than experiments where the emission happens in free space [12, 19, 20]. On the other hand, the presence of two such parallel waveguides from the double-well potential allows the possibility for the twin pair to be emitted into either the left waveguide (L waveguide) or into the right waveguide (R waveguide); hence an entangled state of two atoms only involving motional degrees of freedom is attainable, in principle. We measure momentum correlations between the atoms in the twin pairs and observe a fringe pattern in the normalized second-order correlation function $G^{(2)}$ that stems from a two-particle interference phenomenon.

1.1 The experiment in short

Our project aims at generating highly correlated pairs of rubidium-87 atoms via spontaneous parametric down-conversion from a one-dimensional Bose-Einstein condensate (BEC) trapped in a double waveguide magnetic confinement below an atom chip.
We excite the system by controlled deformations of the trapping potential mainly along one of the transverse, highly confining directions, which we will refer to as the double-well axis. The deformations are achieved by radio-frequency (rf) dressing of

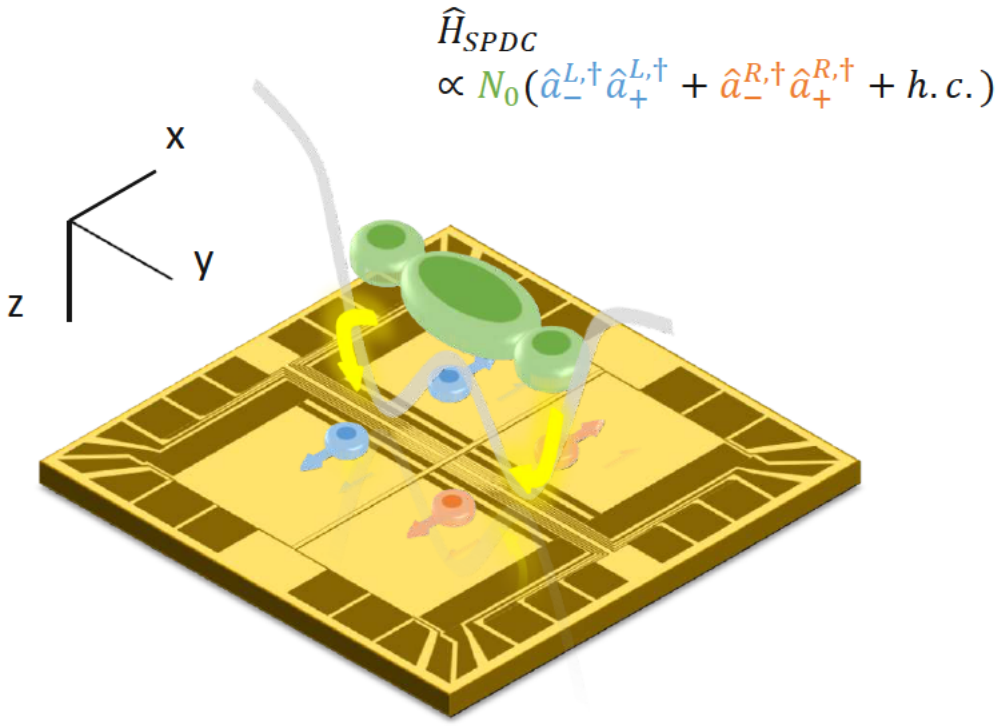

Figure 1.1: Illustration of the experiment described in this thesis (not in scale). A Bose-Einstein condensate (green) is trapped in the second vibrational excited mode of a double waveguide potential (gray), generated by an atom chip (golden, not drawn to scale). Collisions among atoms in the excited condensate generate pairs of momentum-correlated pairs of atoms in a superposition of left (light blue) and right (orange) states.

the atomic magnetic states until we reach a final double waveguide configuration. The optimal-control theory was employed to compute the best trajectory for the rf amplitude (control parameter) to transfer the atoms to the second vibrational mode of the double-well.
Once enough atoms are populating the excited vibrational mode, they can decay back into the lowest vibrational modes of the double-well in the form of pairs of atoms moving in opposite directions along the elongated axis, which we named double twin-atom beams (DTBs, see Fig. 1.1).
The emitted DTB atoms constitute our main subject of investigation. These carry two labels: the momentum at which they separate from the source (first atom and second atom) and the position (left or right) along the double-well axis, perpendicular to the direction in which they move. In other words, they constitute an example of two atomic qubits, which find applications both in theoretical research and in metrological and quantum computing applications.
The detection stage consists of a free fall step, tens of milliseconds long, during which expansion of the atomic wave function takes place, followed by a fluorescence imaging stage where all the atoms (remaining BEC and DTBs) cross a thin sheet of nearly resonant light. The fluorescence photons scattered by the atoms are finally collected by a high-NA objective and focused onto an EMCCD camera.

1.2 General topics

Bose-Einstein condensation is the starting point of our experiments with matter waves. We produce a one-dimensional Bose-Einstein condensate (BEC) using magneto-optical trapping and subsequent evaporation cooling from a background gas of rubidium-87 particles.
Optimal control theory (OCT), applied to many-body quantum systems and their dynamics, allows computing the optimal trajectory across the values of an external control parameter to reach some final state of the system. In our case, the radiofrequency dressing amplitude used to modify the chip trap potential from single to double-well geometry constitutes the external parameter under optimal control investigation. Moreover, the second transverse vibrational state of the final double-well potential used to produce double twin-atom beams is the source state to be reached.
Atom chip is the primary experimental tool in our laboratory. It carries microscopic wire structures (10 to 80 μm in width, 1 μm of thickness up to several mm in length) used to produce inhomogeneous magnetic fields that, in combination with homogeneous external magnetic fields, can be used to trap atoms below its surface. Furthermore, it features wires capable of delivering radiofrequency fields to generate versatile trapping schemes, among which the possibility to create double-well potentials of variable barrier heights.
Correlated and entangled pairs constitute a fundamental tool in the hands of a quantum engineer with a wide range of possible applications, from probing fundamental questions concerning the nature of the quantum world to building blocks for quantum communication and computing, to sensors and development of metrological devices. In particular, freely propagating massive objects have the advantage that their mass could probe the interplay between quantum phenomena (entanglement) and gravity (mass).
Twin-atom beams are pairs of atoms highly correlated in their momentum external

degree of freedom. In 2011, our group discovered a way to produce them from a one-dimensional BEC trapped in a waveguide and motionally optimally excited through OC techniques. Unlike other methods that involve collisions of two condensates or the superposition of a laser lattice (where the twin atoms are emitted into the solid angle with equal probability), collisional de-excitation of an excited BEC in an atom waveguide potential forces the emission to happen along the waveguide axis. This restricted geometry increases the efficiency of the twin atom emission compared to previously mentioned experiments.

Double twin-atom beams (DTBs) Building upon the previous work on twin atoms of 2011, the fundamental achievement of this thesis work is to reach the same level of correlations between twin atoms but in a double waveguide scheme. This critical step enables the possibility of assigning a second spatial label to the atoms, ideally so that the particles become entangled. Aside from its importance per se in fundamental physics research, entanglement constitutes the basis of a wide range of quantum information processes, such as quantum cryptography, quantum teleportation, and quantum metrology.

Atom optics The characterization of the correlated emission happens in momentum space, using a long time of flight imaging. When the atoms are released from the magnetic trap, they fall under gravity, and at the same time, their wavepackets expand along the double-well axis due to the conversion of the confining potential energy into kinetic energy. This operation acts as the matter-wave analog of a beam splitter: the expansion mechanism mixes the initially separated left and right-well wavepackets, making it impossible to distinguish them at the detection site. Furthermore, the long[1] time of flight allows for resolving the momentum components of the wavepackets at the time of their release from the trap. In other words, at the detector site, we are imaging the wavepackets in momentum space rather than in position space. This operation acts as the matter-wave analog of far-field imaging of a light beam.

1.3 Outline

The thesis is organized as follows.

The **first part** (Chapter 2) contains the main theoretical ideas behind Bose-Einstein condensation, in particular in an elongated trap.

The **second part** (Chapter 3) describes the experimental setup, with a focus on the radiofrequency dressing of the internal atomic states and the imaging system that constitute the main tools for achieving the goal of generating double twin atoms and characterizing them.

The **third part** (Chapter 4) introduces the main object of this thesis report: the double twin atom beams (DTBs). These are atomic beams consisting of pairs of atoms with opposite momentum, flying away from the central BEC (at rest). We want to show that they are in a maximally entangled state of the left and right well of the final double-well potential. We investigate the theory behind the DTB emission process (Section 4.1). We then describe the state inversion mechanism that allows transforming an elongated BEC into the source of double twin atoms (Section 4.2). A theoretical calculation of the elements of the transition matrix shows that the predicted double twin atom state is maximally entangled (Section 4.3). A possible extension to a fermionic system is discussed (Section 4.3.3). Section 4.4 contains a detailed description of the image processing methods used during the analysis of the data is

[1] compared to the inverse of the transverse trap frequency

presented and some possible extensions. We finally discuss the important concepts of atom-number squeezing (Section 4.5) and of second-order correlation functions (Section 4.6) that are later widely used for the analysis of the experimental data in Chapter 5.

The **fourth part** (Chapter 5) outlines the main results of this thesis work. We start by characterizing the efficiency of the state inversion procedure, in Section 5.1. Then, in Section 5.2, we verify the twin character of the DTB emission using the number-squeezing parameter. In Section 5.3, we analyze the data with number-squeezing techniques (Section 5.3.1), and density-density correlation functions (Section 5.3.2). This last analysis, in particular, constitutes the main result of the thesis, that is the detection of a two-particle interference effect with density-density correlation techniques.

Lastly, in the **fifth part** (Chapter 6), we give a hint of some possible future directions. In Section 6.1, we discuss a more general description of the DTB state in terms of the spontaneous parametric down-conversion effects. This generalization was recently added to discuss the more general solution to the emission process in the realistic scenario of a multi-pair emission. In Section 6.2, we observe how the atom-atom correlations evolve in time. Finally, in Section 6.3, we see how a simple modification of the DTB procedure can lead to a modified density-density correlation pattern. This last part constitutes a significant and exciting result on state control and manipulation that may lead to further developments on this subject. In Section 6.4 we discuss possible new experimental tools. In particular, the inclusion of two Bragg deflectors would allow performing a Bell test of quantum mechanics in a configuration where massive particles entangled in a spatial degree of freedom are freely moving away from each other. Such a Bell test configuration is ideal for investigating the relationship between the quantum realm and the gravitational world.

Chapter 2

Theoretical bits

2.1 Elements of Bose-Einstein condensation

There is a fundamental dichotomy between bosonic and fermionic particles in the quantum realm. Bosons are characterized by an integer spin (photons, ^{87}Rb atoms, etc.) and have a friendly character, and like to come in groups of many peers. In contrast, fermions have a half-integer spin (electrons, neutrons, protons, etc.) and are incredibly unsocial and do not like the company of any other particle sharing the same quantum numbers with them. Due to the exclusion principle, first formulated by W. Pauli for electrons in the attempt to explain the anomalous Zeeman effect [21], no more than one fermionic particle with all identical quantum numbers can occupy the same quantum state. The exclusion principle does not apply to bosons, which can all "condense" in the same quantum state. When a significant fraction of the atoms shares the same quantum state, we witness a macroscopically enhanced quantum effect. In this enhancement of the otherwise tiny quantum effects lies the interest in the Bose-Einstein condensation.
This section will discuss Bose-Einstein condensation and how it can be derived using thermodynamic considerations. Moreover, it will deal with the case of the trapped quasi-condensate.

2.1.1 Ideal Bose gas

Let us consider a gas of N bosonic atoms (integer spin) confined in a 3d box of volume V at a temperature T. Each particle in the box will have a thermal velocity v_T associated with that temperature. In the context of the particle-wave duality, as de Broglie first pointed out [22], we can associate a matter-wave with a massive particle. In terms of matter waves, this translates into a de Broglie thermal wavelength associated with each atom $\lambda_T = h/mv_T$, where m is the atomic mass and h is Planck's constant. Another critical length scale of the system is the inter-particle distance $d_0 = (N/V)^{-1/3}$, set by the number of particles present in a fixed region of space. When the temperature is lowered enough such that $d_0 \leq \lambda_T$, we reach quantum degeneracy [23] i.e., all degrees of freedom of the gas must be treated quantum mechanically. New effects may appear, among which the onset of Bose-Einstein condensation (BEC) describes the situation of a macroscopic population of the lowest energy state available.
The value of the temperature at which quantum effects start becoming important, or critical temperature T_c, the condensed fraction, and other thermodynamic quantities strongly depend on the particular energy spectrum of the system under investigation, which in turn depends on the dimensionality, confining geometry, in-

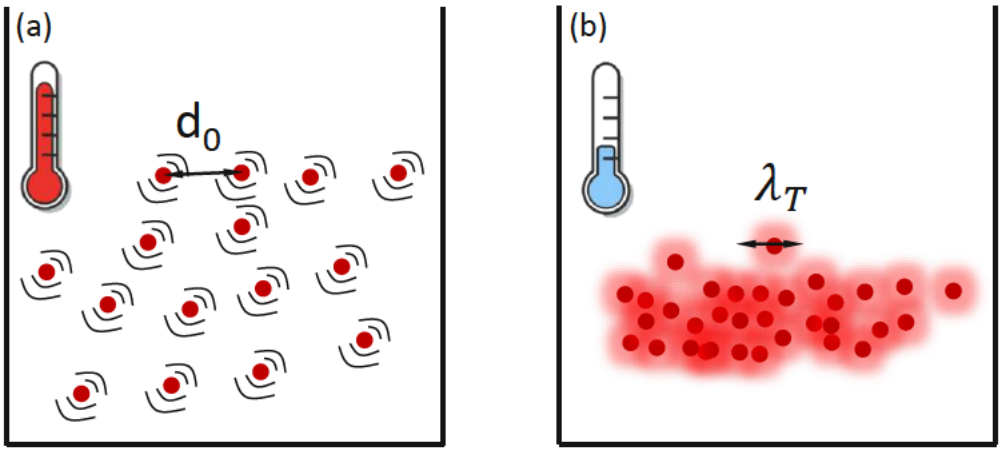

Figure 2.1: (a) Hot gas: particles have high kinetic energy and the gas can still be treated classically. d_0 represents the mean inter-particle distance. (b) Ultra-cold gas of bosons: particles have negligible kinetic energy, and the gas shows quantum mechanical properties. $\lambda_T \gg d_0$ is the de Broglie wavelength associated to each particle.

homogeneity of the atomic sample. It has been shown, for example (see [24]), that no condensation is predicted for dimensionality $d \leq 2$ for a Bose gas confined in a box-like potential. In the previous mentioned case of N bosons confined in a 3d box potential, condensation starts at the critical temperature T_{3d} given by [25]:

$$k_B T_{3d} = \frac{h^2}{2\pi m}\left(\frac{1}{g_3(0)}\frac{N}{V}\right)^{2/3} \tag{2.1}$$

where $g_3(\mu/k_BT)$ is the 3d Bose function and μ the chemical potential and where

$$g_3(0) = \zeta(\frac{3}{2}) = 2.612, \tag{2.2}$$

with $\zeta(x)$ being the Riemann zeta function.

Harmonic trap case

Following [26], let us now consider the case of a cold gas trapped in a harmonic confinement in the general case of d dimensions and write the potential V and the energies $\varepsilon_{n_x n_y n_z}$ as:

$$V(\vec{r}) = \frac{1}{2}m(\omega_x^2 x^2 + \omega_y^2 y^2 + \omega_z^2 z^2), \quad \varepsilon_{n_x n_y n_z} = \sum_{i=x,y,z}(n_i + \frac{1}{2})\hbar\omega_i, \tag{2.3}$$

where n_x, n_y, n_z are non-negative integer numbers.
The single-particle ground state, obtained for $n_x = n_y = n_z = 0$ is given by:

$$\phi_0(\vec{r}) = \left(\frac{m\omega_{ho}}{\pi\hbar}\right)^{3/4} \exp\left[-\frac{m}{2\hbar}(\omega_x x^2 + \omega_y y^2 + \omega_z z^2)\right], \tag{2.4}$$

where we defined the geometric mean of the oscillator frequencies

$$\omega_{ho} = (\omega_x\omega_y\omega_z)^{1/3}. \tag{2.5}$$

At zero temperature, when all the atoms occupy the lowest state, the density profile of the cloud is $n(\vec{r}) = N\left|\phi_0(\vec{r})\right|^2$; hence its amplitude is proportional to the number of atoms in the ground state. Its size is given by:

$$a_{ho} = \left(\frac{\hbar}{m\omega_{ho}}\right)^{1/2} \tag{2.6}$$

and is independent of N.
At finite temperature, some of the atoms will occupy higher states. The density profile associated with these "hot" atoms is much larger than the condensate radius $a_{ho} \sim 1\ \mu$m, and we can use this information to reveal the condensed fraction. For example, if we approximate the thermal distribution with a classical Boltzmann distribution such that $n_{cl}(r) \propto \exp\left[-V_{ext}(r)/k_BT\right]$ for $V_{ext}(r) = 1/2m\omega_{ho}^2 r^2$, the width of the thermal cloud is given by $R_T = a_{ho}(k_BT/\hbar\omega_0)^{1/2}$. In the limit $k_BT \gg \hbar\omega_{ho}$ we get $R_T \gg a_{ho}$. In the Fourier space, when looking at the momentum profiles of both the thermal and condensed fractions, the profiles will also be different; hence we can identify the condensate in the momentum space. In the previous example, after a long time of flight, the width of the condensate is proportional to $(a_{ho})^{-1}$, and the width of the thermal part is proportional to $(k_BT)^{1/2}$, which is how the first BEC reveal took place [27,28].
The shape of the trapping potential defines the symmetry of the problem. In our case, as we will later discuss in the thesis, we deal with axial symmetry. This means we can define an axial or *longitudinal* coordinate x and a radial or *transverse* coordinate $r_\perp = \sqrt{y^2+z^2}$, with the corresponding angular frequencies, $\omega_\parallel = \omega_x$ and $\omega_\perp = \omega_y = \omega_z$.

2.1.2 Weakly interacting Bose gas

Most of the remarkable different quantum regimes that can be achieved for ultracold atoms in lower dimensions depend on the interactions between atoms. For this reason, it is helpful to introduce here the general description of interacting Bose gases. In second quantization formalism, the general Hamiltonian for an interacting gas of Bosons is given by:

$$\hat{H}_{tot} = \int \mathrm{d}\vec{r}\hat{\Psi}^\dagger(\vec{r},t)\hat{H}_0\hat{\Psi}(\vec{r},t) + \frac{1}{2}\iint \mathrm{d}\vec{r}\,\mathrm{d}\vec{r}'\hat{\Psi}^\dagger(\vec{r},t)\hat{\Psi}^\dagger(\vec{r}',t)V(\vec{r}-\vec{r}')\hat{\Psi}(\vec{r}',t)\hat{\Psi}(\vec{r},t), \tag{2.7}$$

where $\hat{H}_0 = -\hbar^2\nabla^2/(2m) + V_{ext}(\vec{r},t)$ is the single-particle Hamiltonian with the confinement potential V_{ext}, and where V represents only the atom-atom interaction term. In this formalism, the collective Bose field operator is given in terms of the single-particle annihilation operator $\hat{a}_i$ corresponding to modes with wave functions ψ_i:

$$\hat{\Psi}(\vec{r},t) = \sum_{i=0}^{M} \psi_i(\vec{r},t)\hat{a}_i(t). \tag{2.8}$$

In the case of a very dilute gas, where particles have little chance to encounter themselves, we can replace the general $V(\vec{r}-\vec{r}')$ term by a pseudo-potential $g\delta(\vec{r}-\vec{r}')$, where the coupling constant g is linked to the scattering length a_s by:

$$g_{3d} = \frac{4\pi\hbar^2 a_s}{m}. \tag{2.9}$$

With this approximation, we can rewrite Eq. (2.7) as:

$$\hat{H}_{tot} = \int \mathrm{d}\vec{r} \left[\hat{\Psi}^\dagger(\vec{r},t)\hat{H}_0\hat{\Psi}(\vec{r},t) + \frac{g_{3d}}{2}\hat{\Psi}^\dagger(\vec{r},t)\hat{\Psi}^\dagger(\vec{r},t)\hat{\Psi}(\vec{r},t)\hat{\Psi}(\vec{r},t) \right]. \tag{2.10}$$

Instead of trying to solve the full Heisenberg equation corresponding to the Hamiltonian above, one common approach is to adopt a mean-field description and replace the operator for the condensate mode $\hat{\Psi}_0(\vec{r},t)$ that has a macroscopic population N_0 with a complex field $\psi_0(\vec{r},t)$:

$$\hat{\Psi}_0(\vec{r},t) = \psi_0(\vec{r},t) + \hat{\delta}(\vec{r},t). \tag{2.11}$$

This ansatz, known as the *Bogoliubov approximation* [29], leads to the well known Gross-Pitaevskii equation (GPE) for the condensate wave function $\psi_0(\vec{r},t)$:

$$i\hbar\frac{\partial}{\partial t}\psi_0(\vec{r},t) = \left[-\frac{\hbar^2}{2m}\nabla^2 + V_{ext}(\vec{r},t) + g_{3d}\left|\psi_0(\vec{r},t)\right|^2 \right] \psi_0(\vec{r},t). \tag{2.12}$$

Its static counterpart can be found with the substitution $\psi_0(\vec{r},t) = \psi_0(\vec{r})e^{-i\mu t/\hbar}$:

$$\mu\psi_0(\vec{r}) = \left[-\frac{\hbar^2}{2m}\nabla^2 + V_{ext}(\vec{r},t) + g_{3d}\left|\psi_0(\vec{r},t)\right|^2 \right] \psi_0(\vec{r},t), \tag{2.13}$$

where μ represents the chemical potential. A typical solution of the static GPE equation for a trapped BEC can be found in the case of the chemical potential μ being larger than the trap level spacing $\hbar\omega_{ho}$. In this case, we can neglect the kinetic term in Eq. (2.13), known as the Thomas-Fermi (TF) approximation, and solve for $n_0(\vec{r})$ to obtain:

$$n_0(\vec{r}) = \begin{cases} g_{3d}^{-1}[\mu - V_{ext}(\vec{r})], & \text{for } \mu > V_{ext}(\vec{r}) \\ 0, & \text{otherwise} \end{cases}. \tag{2.14}$$

The Thomas-Fermi profile $n_0(\vec{r})$ of Eq. (2.14) corresponds to an inverted parabola with radius l_i:

$$l_i = \sqrt{\frac{2\mu}{m\omega_i^2}}, \tag{2.15}$$

along the i direction. As we will see in the following, in the case of a BEC in a very elongated trap with transverse symmetry, the Thomas-Fermi approximation $\mu \gg \hbar\omega_x$ is well satisfied along the elongated x direction.

One-dimensional trapped Bose gas

Low-dimensional Bose gases were the subject of an intensive theoretical investigation, initially without the possibility of any experimental test. Here we collect the main points worth mentioning for understanding the raw material of this thesis work: the trapped 1d quasi-condensate of ^{87}Rb atoms, following the review [30].
The usual conditions for treating a system as one-dimensional are defined by the relation between its typical energy scales. Consider a Bose gas confined in a cigar-shaped trap where $\omega_\perp \gg \omega_\parallel$. Its typical energy scales are the chemical potential μ, its thermal energy k_BT, and its transverse and longitudinal energies $\hbar\omega_\perp$ and $\hbar\omega_\parallel$ respectively. We can describe the system as one-dimensional (1d) when both the chemical potential and the thermal energies are small compared to the strength of

the transverse confinement: $\mu, k_B T \ll \hbar\omega_\perp$. Along y, z the condition $\mu \ll \hbar\omega_\perp$ invalidates the Thomas-Fermi approximation, and the wave function along this direction approaches the single-particle ground state ϕ_0 of the confining potential [31]. In this case, we talk about the "freeze-out" of the transverse dynamics, the condensate being in the transverse ground state $\Psi_\perp = \phi_0(y)\phi_0(z)$. As we will see later, when twin pairs are emitted with non-negligible kinetic energy in such 1d geometry, they can only move along the longitudinal axis, where the potential is shallow, and dynamics are still possible. The radius of the single-particle ground state ϕ_0 is given by:

$$l_\perp = \sqrt{\frac{\hbar}{m\omega_\perp}}. \tag{2.16}$$

Suppose the radial extension of the wave function $l_\perp = (\hbar/m\omega_\perp)^{1/2}$ is much larger than the characteristic radius of the inter-atomic potential R_e. In that case, the interaction among particles has a 3d character and can be described by the 3d scattering length $a_s \ll a_\perp$. In this case, we can average the 3d interaction over the radial density profile to obtain an effective 1d scattering amplitude [32]:

$$g_{1d} = \frac{2\hbar^2 a_s}{m a_\perp^2} = 2\hbar\omega_\perp a_s. \tag{2.17}$$

However, along the elongated x direction where the condition $\mu \gg \hbar\omega_x$ holds one can use Eq. (2.15) to compute the size of the condensate along this direction.

Different regimes

It is possible to identify different regimes of a one-dimensional Bose gas. Consider first a homogeneous gas. The one-dimensional Lieb-Liniger Hamiltonian defines its properties:

$$\hat{H}_{1d} = \int \mathrm{d}x \left[-\frac{\hbar^2}{2m}\hat{\Psi}^\dagger(x)\tfrac{\partial^2}{\partial x^2}\hat{\Psi}(x) + \frac{g_{1d}}{2}\hat{\Psi}^\dagger(x)\hat{\Psi}^\dagger(x)\hat{\Psi}(x)\hat{\Psi}(x) \right], \tag{2.18}$$

where we introduced the one-dimensional interaction constant:

$$g_{1d} = g_{3d} \int |\phi(y)|^4 \,\mathrm{d}y \int |\phi(z)|^4 \,\mathrm{d}z. \tag{2.19}$$

The parameter $\gamma = E_{int}/E_{kin} = \frac{g_{1d} m}{\hbar^2 n}$ distinguishes two regimes: (a) weakly interacting regime ($\gamma \ll 1$) is characterized by "high densities". In this limit, a mean-field theory (see Eq. (2.12)) is well justified and condensation is possible. Also, $\mu \ll \hbar\omega_\perp$ holds, so the transverse dynamics is frozen; (b) lower densities along the longitudinal dimension determine the Tonks-Girardeau regime ($\gamma \gg 1$), where bosons start exhibiting some fermionic properties. In this thesis, we will only be concerned with the first type.

Trapped quasi-condensates

Early theoretical studies focused on low-dimensional Bose gases with repulsive interactions. We already mentioned that no condensation is expected at finite temperature in the thermodynamic limit for spatially homogeneous systems, which is physically due to large phase fluctuations and a consequent finite coherence length [33]:

$$\lambda_c = \frac{2\hbar^2 n}{mT}, \tag{2.20}$$

where n represents the one-dimensional atomic density that in our experiment with $N \geq 800$ atoms has typical values of $n \geq 30\,\text{atoms}/\mu\text{m}$.
We introduce the *local density approximation* (LDA): assuming that the density varies slowly with respect to the relevant length scales, we consider the gas locally homogeneous so that we can still apply all the previous theoretical machinery. The entire gas is at thermal equilibrium with the temperature T and the global chemical potential μ_0. However, the local chemical potential μ is shifted by the external potential: $\mu(x) = \mu_0 - V_{ext}(x)$ (cross-over regime, see [34]).
In this thesis, we work with a Bose-Einstein condensate (BEC) of ^{87}Rb trapped in a cylindrical trap below an atom chip. If the relevant energy for a BEC (chemical potential μ) is much smaller than the energy $\hbar\omega_\perp$ associated with the transverse level-spacing, any dynamics along this direction is frozen. The Hamiltonian describing such a system is the Gross-Pitaevskii equation (GPE) for 1d systems [35]:

$$\left[-\frac{\hbar^2}{2m}\frac{d^2}{dx^2} + V_{trap}(x) + g_{1d}N\left|\psi(x)\right|^2 - \mu \right]\psi(x) = 0, \tag{2.21}$$

where $\psi(x)$ denotes the longitudinal BEC wavefunction, μ is the chemical potential, V_{trap} is the trapping potential, and g_{1d} is the effective one-dimensional coupling strength.
^{87}Rb has a positive scattering length, which means it is mutually repulsive at low temperatures. Also the coupling constant g_{1d} present in the short-range interaction term between particles is positive since

$$g_{1d} = 2\hbar^2\omega_\perp a_s, \tag{2.22}$$

where $a_s = 5.2$ nm for the $|F = 1, m_F = -1\rangle$ state of ^{87}Rb [36]). When dealing with around 800-1500 atoms trapped in an elongated trap with $\omega_\perp \simeq 2\pi \times 1$ kHz and $\omega_\parallel \simeq 2\pi \times 12$ Hz, we can assume that

$$\mu = g_{1d}n_0, \tag{2.23}$$

where $n_0 \simeq 30\,\text{atoms}/\mu\text{m}$ is the central density. We can then compute the Thomas-Fermi radius l_x along the longitudinal direction as:

$$l_x = \sqrt{\frac{2\mu_0}{m\omega_\parallel^2}} \simeq 23\,\mu\text{m}. \tag{2.24}$$

On the other hand, considering a temperature of the condensate of $T = 40$ nK one obtains that the coherence length $\lambda_c \propto T^{-1}$ from Eq. (2.20) is

$$\lambda_c \simeq 8.3\,\mu\text{m}. \tag{2.25}$$

2.2 Quantum collisions

Let us consider a gas made of neutral atoms, and let us call d the relative distance between two atoms of the gas. When neglecting the magnetic dipole term, we get a contact potential $V(d)$ of the Lennard-Jones type:

$$V(d) = \frac{C_{12}}{d^{12}} - \frac{C_6}{d^6}. \tag{2.26}$$

In a very dilute gas, the most likely collisions involve two atoms at a time. These are generally elastic collisions, i.e., the two atoms will bounce off each other, and

no molecule is formed. Three-body collisions are the first case where the presence of a third entity allows the conservation of the total momentum, allowing for the formation of molecules and atom losses (inelastic collisions).
From a classical point of view, given the potential in Eq. (2.26), two atoms that come close enough can interact via a Van der Waals $\propto -1/d^6$ type of attractive force and for a short time (short-range interaction), hence give rise to a collision.
Quantum mechanically (see the distinction between the classical and quantum theory based on the comparison between the de Broglie wavelength λ_T and the inter-particle distance d in Section 2.1.1), the Hamiltonian describing two interacting atoms with masses m_1 and m_2 and momenta $\vec{p}_1$ and $\vec{p}_2$ is given by:

$$\hat{H} = \frac{\hat{p}_1^2}{2m} + \frac{\hat{p}_2^2}{2m} + V\left(|\vec{r}_1 - \vec{r}_2|\right). \tag{2.27}$$

Let us assume an isotropic potential (as it is the van der Waals one for example) and rewrite Eq. (2.27) in the center-of-mass (CoM) coordinates:

$$\hat{H} = \frac{\hat{P}^2}{2M} + \frac{\hat{p}^2}{2\mu} + V(r) \tag{2.28}$$

where $M = m_1 + m_2$, $\mu = 1/(m_1^{-1} + m_2^{-1})$, $P = p_1 + p_2$, $p = p_1 - p_2$. Since the P-term is just a constant, we can neglect it. The correspondent Schrödinger equation reads:

$$\left[\frac{\hat{p}^2}{2\mu} + V(r)\right]\Psi(\vec{r}) = E\Psi(\vec{r}) \tag{2.29}$$

where $r = |\vec{r}_1 - \vec{r}_2|$ and $E = \frac{\hbar^2 k^2}{2\mu}$ with $k = k_1 - k_2$. We seek for solutions of the type:

$$\Psi(\vec{r}) = \Psi_{in}(\vec{r}) + \Psi_s(\vec{r}) \to e^{ikz} + f(k,\theta)\frac{e^{ikr}}{r}, \quad \text{for } r \gg b \tag{2.30}$$

where Ψ_{in} and Ψ_s are the incident and scattered wave components, and we assumed the collision happened along z. The right arrow describes the limit at large distances $r \gg b$, where b is the range of the potential. This limit is interesting in most cases since we usually need to know how the particles behave far from the collision point, where we expect the wavefunction linked to the particle to be the solution of the free Schrödinger equation. The amplitude of scattering $f(k,\theta)$ is such that:

$$\frac{d\sigma}{d\Omega} = \left|f(k,\theta)\right|^2, \tag{2.31}$$

where σ is the cross section and Ω the solid angle. From partial wave analysis (see [37]) one can write:

$$f(k,\theta) = \frac{1}{k}\sum_{l=0}^{\infty}(2l+1)P_l(\cos\theta), e^{i\delta_l(k)}\sin\delta_l(k) \tag{2.32}$$

as a special case for a central, static potential.
Let us now consider the limit of low energy (ultracold gases). Let us write the $\Psi(\vec{r})$ as an expansion in the partial waves basis:

$$\Psi(\vec{r}) = \sum_{l=0}^{\infty}\sum_{m=-l}^{m=+l}\frac{u_{lm}(r)}{r}Y_{lm}(\theta,\phi). \tag{2.33}$$

Since $V(r)$ is isotropic (no explicit dependence on azimuthal angle ϕ) one can retain only the term $m = 0$ in the expansion:

$$\Psi(\vec{r}) = \sum_{l=0}^{\infty} \frac{u_l(r)}{r} P_l(\cos\theta). \tag{2.34}$$

We rewrite Eq. (2.29) in cylindrical coordinates to obtain:

$$\left[-\frac{\hbar^2}{2\mu}\partial_r^2 + \frac{\hbar^2 l(l+1)}{2\mu r^2} + V(r) - E \right] u_l(r) = 0, \quad \forall l \tag{2.35}$$

where the $l(l+1)$ term is a centrifugal term that generates a repulsive potential for atoms, i.e., it acts as a potential barrier that needs to be overcome for the atoms to come into contact and collide. In the limit of low energies, only the $l = 0$ term will give rise to collisions and scattering of two atoms off each other: this represents the so-called s-wave approximation, for which one finds:

$$\begin{aligned} \delta_0(k) &= -ka \\ \sigma &= \frac{4\pi}{k^2}\sin^2(-ka) \simeq 4\pi a^2, \end{aligned} \tag{2.36}$$

where a is the scattering length.
Let us now consider the case of two identical particles coming close enough to be able to interact via the Lennard-Jones potential of Eq. (2.26). Since the particles are indistinguishable, quantum statistics plays an important role. In particular, the general expression for the differential cross-section of Eq. (2.31) reads:

$$\frac{d\sigma}{d\Omega} = \frac{1}{2}\left| f(k,\theta) + \epsilon f(k,\pi-\theta) \right|^2 \tag{2.37}$$

where $\epsilon = 1$ stands for bosonic particles and $\epsilon = -1$ stands for fermionic particles. The cross section is then given by:

$$\sigma = \frac{8\pi}{k^2}\sum_{l=0}^{\infty}(2l+1)(1+\epsilon(-1)^l)\sin^2\delta_l(k), \tag{2.38}$$

where $l = 0, 2, 4...\infty$ (positive *even* integer numbers) for bosons and $l = 1, 3, 5...\infty$ (positive *odd* integer numbers) for fermions. This means that at very low temperatures (when only the lowest values of l are relevant), the cross-section has different values for bosons (B) and fermions (F). In particular, we get $\sigma_B = 8\pi a^2$ and $\sigma_F = 0$. In s-wave approximation, fermions do not interact and behave as an ideal noninteracting gas due to their statistics.

2.3 Twin-atom entanglement in double-well potentials

More than 30 years ago, Ghosh and Mandel sent twin photons entangled in momentum through a double slit and measured two-photon coincidence detections in far field [38]. They then observed conditional[1] fringes, which were later shown to be related with entanglement [39]. Our system constitutes the matter analog of such an optical experiment in that we use atoms instead of photons and atomic waveguides instead of optical beam splitters.

[1] Conditional in the sense that they only show up when correlating the detection events of the twin photons.

The primary system under investigation will be the twin particles that move away from the main BEC (see Section 4.2). Following the recent publication on this matter [18], we here want to summarize the general methods to perform state tomography of twin-atom states in double-well potentials.
A pair of atoms generated at the same time and moving away from the central BEC with opposite momenta $\pm p_0 = \pm\hbar k_0$ is called a twin pair [40]. An atom from a twin-atom source (Fig. 2.2) can be trapped in a double waveguide, where the presence of each atom in the pair in either the left $|L\rangle$ or right $|R\rangle$ well forms the basis states of a qubit (see Fig. 2.3).

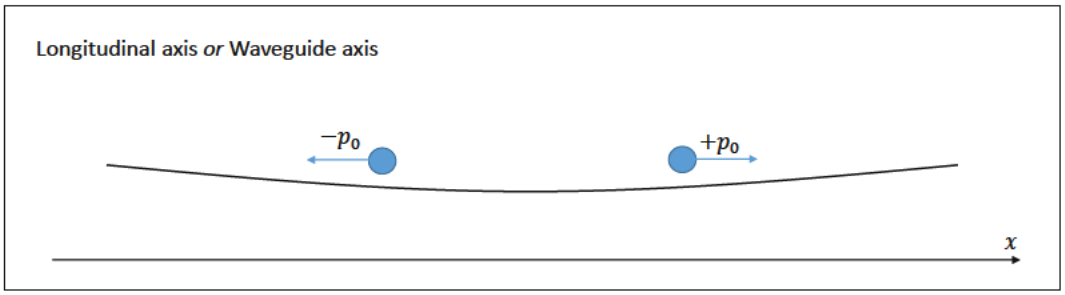

Figure 2.2: Twin atoms: a pair of simultaneously emitted atoms moving with opposite momenta $\pm p_0$ along the waveguide axis or longitudinal axis constitute a twin pair.

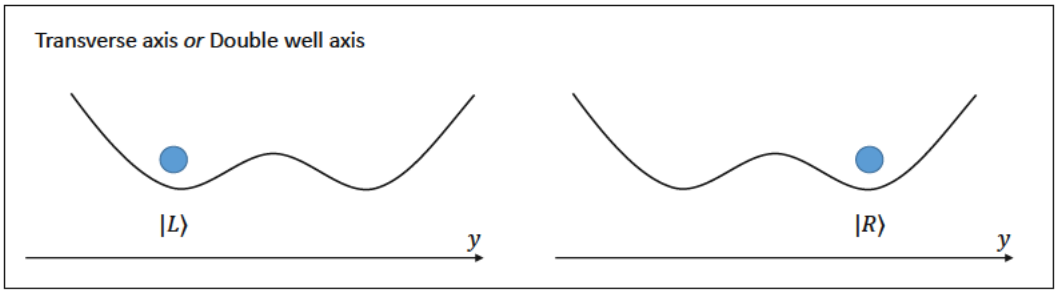

Figure 2.3: Twin atoms in a double waveguide: a pair of simultaneously emitted atoms moving with opposite momenta $\pm p_0$ along the waveguide axis or longitudinal axis (not drawn here) are trapped in a double-well potential along the transverse axis.

We can use the momentum degree of freedom to distinguish the atoms and call the particle with momentum $p_1 = -p_0$ along the waveguide axis to be atom 1, and therefore the particle with momentum $p_2 = +p_0$ along the waveguide axis to be atom 2. In this case, we deal with two distinguishable qubits with negligible interactions. We can also consider each atom as indistinguishable and assign to it a momentum label $\{1,2\} = \{-p_0, +p_0\}$, and a position label $\{|L\rangle, |R\rangle\}$. In this view, there are four single-particle modes available for two indistinguishable atoms: $|L_1\rangle, |R_1\rangle, |L_2\rangle, |R_2\rangle$. In case of twin pairs, the two-atom state is limited to the symmetric Hilbert space $\mathcal{H}_{pair} = \{|LL\rangle, |LR\rangle, |RL\rangle, |RR\rangle\}$, with $|ij\rangle = 1/\sqrt{2}(|i\rangle_1 \otimes |j\rangle_2 + |j\rangle_2 \otimes |i\rangle_1)$, since for one atom with momentum $-p_0$ (label 1) the second one has momentum $+p_0$ (label 2).
We want to be able to characterize the two-atom state $|\Psi\rangle \in \mathcal{H}_{pair}$ without any assumptions on its purity or existence in a certain subspace of $\mathcal{H}_{pair}$. The characteriza-

tion of a two-particle state must rely on two-particle properties. For this reason, one starts by looking at the second-order correlator

$$G^{(2)}(\xi_1,\xi_2) = \langle\hat{\Psi}^\dagger(\xi_1)\hat{\Psi}^\dagger(\xi_2)\hat{\Psi}(\xi_1)\hat{\Psi}(\xi_2)\rangle = \mathrm{Tr}[\hat{\rho}\hat{\Psi}^\dagger(\xi_1)\hat{\Psi}^\dagger(\xi_2)\hat{\Psi}(\xi_1)\hat{\Psi}(\xi_2)], \quad (2.39)$$

where ξ_1 (ξ_2) are the coordinates of the first (second) atom, and $\Psi(\xi_n)$ is the wavefunction of the n-th atom.
The real part of the atom-atom correlator in Eq. (2.39) is experimentally accessible either by looking at the left and right components of the two-particle state separately (position measurement) or by letting them overlap and interfere (momentum measurement). We can obtain different information on the initial state by preparing different experimental sequences, which we have named as *separation* procedure when we perform a position measurement, and *interference* procedure when we measure in momentum space.
In our experimental setup, we are limited by the difficulty of emitting and detecting only one pair at a time. Our detector [41] cannot reliably distinguish single atoms from electronic noise. For this reason, we mostly rely on number-squeezing techniques that do not require identifying the partner of each atom and use $G^{(2)}(\xi_1,\xi_2)$ based analysis only on those data sets where it is strictly required while keeping the average pair emission as low as possible.
The two detection schemes that are, in principle, available to our setup (position and momentum-space-based detection schemes) are equivalent to the experiment performed by Ghosh and Mandel [38].

2.4 Bell tests of Quantum Mechanics

In 1935 Albert Einstein, Boris Podolsky, and Nathan Rosen (EPR) wrote a paper [3] where the following paradox was presented in order to challenge the quantum mechanical theory and save a local-realistic point of view.
Let us consider two half-integer spins in the two-particle singlet state $|\psi^-\rangle$ at two far locations identified by the indices $1(2)$:

$$|\psi\rangle \propto |1+,2-\rangle - |1-,2+\rangle \quad (2.40)$$

where we fixed a certain direction z for the spin projections and where $|1\pm\rangle$ ($|2\pm\rangle$) are the two eigenstates of S_{1z} (S_{2z}) along the same direction. If the observer $\mathcal{O}_1$ at location 1 measures the spin component S_{1z} of spin 1 and finds the result $+1/2$, then when $\mathcal{O}_2$ at location 2 measures S_{2z} we can predict with certainty that he will find the result $-1/2$, given the state in Eq. (2.40).
The EPR authors assumed that the measurement on spin 1 by $\mathcal{O}_1$ cannot influence the state of spin 2 at the remote location. However, we can indeed predict the result of the measurement of spin 2 given the result of the measurement on spin 1. Therefore, concluded the EPR authors, S_{2z} must be a pre-existing element of reality. This way of reasoning is called *local realism*. A paradox arises from the fact that the state in Eq. (2.40) cannot be factorized as the product of the separate single-particle spin states in any of the x,y,z-directions. Therefore, also S_{2x} (and S_{2y}) should possess the same pre-existing property. This clashes with the requirements imposed by the uncertainty principle on non-commuting observables (S_z and S_x or S_y in this case), which cannot simultaneously have well-defined values in a quantum state.
Although this paradox was presented by the authors as a challenge against the nonlocal quantum mechanical view of the world and was intended as a mere thought experiment or *Gedankenexperiment*, in 1964's paper by J. S. Bell "On the Einstein Podolsky Rosen Paradox" [42], he derives an inequality for the value of an observable

linked to the measurements carried out by the two distant observers which, if not satisfied, rules out the possibility of hidden variables and EPR's attempt to save both local-realism and quantum mechanical prediction. Since 1972 physicists worldwide have tested Bell's inequalities in the laboratory with more and more refined experiments and techniques. All the experiments so far, whether with photons [43–48] or massive particles like protons [49], ions [50], electrons [51], or internal states of atoms [52] have confirmed the non-local predictions of quantum mechanics.

Chapter 3

The experimental setup

This chapter will mention the main components of the experimental setup, internally referred to as the Rb2 experiment, to distinguish it from the other Rubidium-87-based experiment at the Atominstitut in Vienna. We will only pay attention to those most relevant parts to produce double twin-atom beams and detect them. The setup did not change significantly from previous works [53–55], to which we refer the interested reader for more information.
In short, our recipe for a Bose condensate contains five main ingredients: gaseous rubidium atoms, ultra-high vacuum technology, two main laser sources, magnetic trapping, and evaporative cooling. In addition to these basic ingredients, we use radiofrequency dressing techniques to modify the shape of the confining potential.
Compared to previous setups, we replaced the empty rubidium dispensers and the large bottom window of the science chamber. Lastly, we implemented a new absorption camera (see Section 3.4.1) to replace the previous one, which failed.

3.1 The main experimental components

The Rb2 machine is a complex setup, with several parts working together to create a Bose-Einstein condensate of rubidium atoms and manipulate it. It comprises ultra-high vacuum components (main chamber, three or four different vacuum pumps, pressure monitoring), electro-optical elements (rubidium rods, atom chip, and its supplies, magnetic fields supplies, rf-field generators, lasers, mirrors, beam-splitters, AOMs, fibers), and monitoring and control system (various computer stations, the ADwin control), to name a few. Let us now review in more detail some of them.

3.1.1 Vacuum technology

Part of the work of this thesis was opening the vacuum system and replacing the empty rubidium dispensers. We also replaced the large window below the science chamber during this procedure.
As we mentioned in the theoretical sections, Bose-Einstein condensation happens at extremely low temperatures of tens of nK. Even if these temperatures are impressively low, no cryogenic device is required. Apart from the atoms, all the other instruments used in our laboratory are at room temperature.
Instead, the price we need to pay to reach some of the coldest temperatures in the whole Universe is ultra-high vacuum (UHV) technology. A low background pressure of the order of 10^{-11} mbar is necessary to prevent atom loss and heating due to collisions with background atoms at room temperature. For this reason, we need

to first achieve UHV by a combination of different pumps characterized by different pressure ranges.
The UHV main pump is an Agilent ion getter pump[1]. Such technology aims first to ionize any background atom or molecule and trap them inside the Titanium made cathodes. The ion pump works in the pressure range 10^{-11}-10^{-8} mbar. To cover the range from atmospheric pressure to 10^{-8}, we used a Rough pump and a Turbo Molecular pump. There are also two side UHV pumps: one Titanium Sublimation Pump (TSP) and one Non-Evaporative Getter (NEG) pump. The first is activated roughly every two weeks, while the latter is a passive pump that acts like a sponge and helps capture background atoms that stick to its large surface. A UHV Gauge at the science chamber monitors the pressure p_c inside the science chamber. If $p_c \leq 1 \times 10^{-10}$ mbar, we have a stable and reproducible BEC production. If not, one can still activate the TSP pump to try restoring the proper pressure inside.

3.1.2 Rubidium source

Rubidium atoms are stored in dispensers made of metallic rods in a Rubidium chromate compound. A water-cooled side flange holds the metallic rods located on one of the eight side apertures of the octagonal-shaped stainless-steel science chamber, while copper feed-troughs provide the current. Increasing the current running through the dispensers produces a higher Rubidium background pressure since more atoms are released due to the Joule effect. Because we only have one chamber, the atomic flow must be regulated. It is higher in the first half of the experimental cycle when atoms are gathered together in a magneto-optical trap. In the second half of the cycle, the current in the metallic rods is decreased to avoid collisions with background atoms at higher temperatures, resulting in heating and losses. Water cooling helps cool down the rods faster and stops the Rubidium flow in the second part of the experimental cycle.

3.1.3 The science chamber

Our experiment features a single-chamber design. The price we need to pay for a more compact setup than experiments with two chambers is a longer experimental cycle since the higher and lower background phases mentioned before coexist in the same chamber.
One window aperture hosts the rubidium source, and the other seven apertures of the octagonal chamber provide optical access. A large window at the bottom is used to image the atoms after their release from the trapping potentials.

3.1.4 The copper structure

On top of the science chamber, a flange with water-cooling connectors hosts the mounting for the atom chip connections. It comprises two different structures: one is made of large 5-mm thick copper wire connectors for high DC currents up to 60 A; a second, more internal structure, comprises a 36-pin feedthrough structure to connect to the thinner atom chip wires.
The copper wires are a flat U-shaped wire, a smaller Z-shaped wire with a length of 4 mm, and two bars. We use them as follows (see Fig. 3.1):

[1] Varian StarCell, 500 L/s

- A large H-structure connected to form a U-shaped copper wire is used with an external bias field to produce the magnetic quadrupole field needed during the magneto-optical trap (MOT) phase. It is also used later in the experimental cycle as an antenna for evaporative cooling when carrying an oscillating current (in blue in Fig. 3.1).
- A Z-shaped copper wire separated by a gap from the larger U-structure, combined with an external bias field and Ioffe field, produces an intermediate large volume trap (green).
- Two I-shaped wires running along y serve either as Stern-Gerlach separators for the different magnetic m_F states or for additional longitudinal confinement (red).

3.1.5 The atom chip

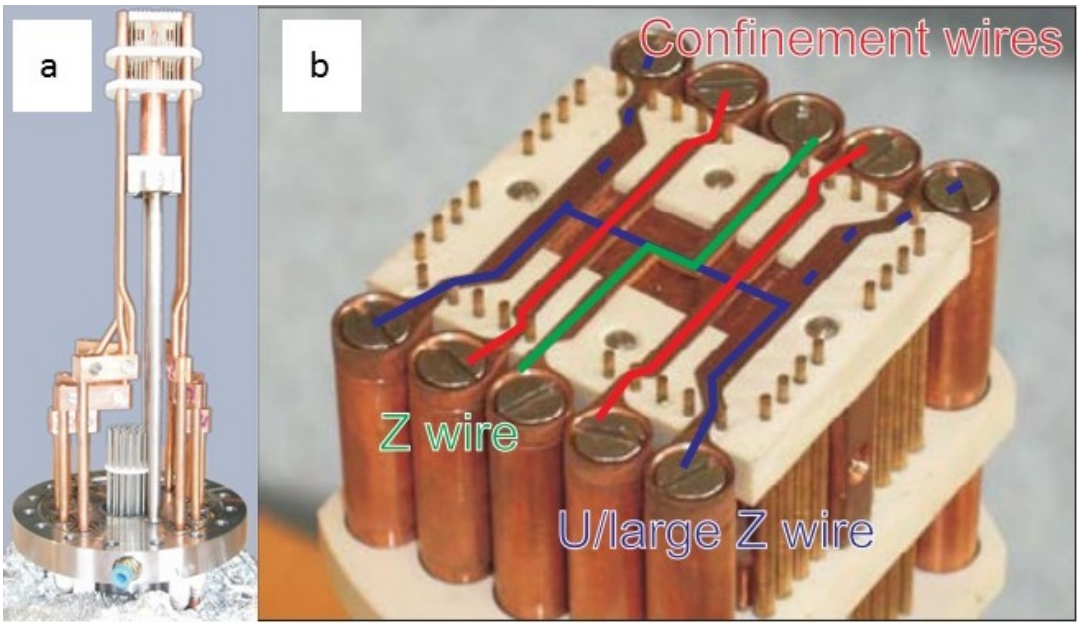

Figure 3.1: Adapted from Ref. [56]. (a) The chip mounting. (b) Schematics of the copper wire structure below the atom chip surface. Z-, U-, and I-shaped wires are depicted in green, blue, and red, respectively.

The actual atom chip lies on top of the aforementioned copper structure. It was designed and manufactured at the Weizmann Institute in the group of I. Bar-Joseph in Israel by Sönke Groth using different lithographic techniques [53].
A sketch of the layout appears in Fig. 3.2. Its gold surface serves as a mirror during the MOT phase. It has a double-layer structure, enabling a three-wire H-shaped trapping scheme where wires from different layers can cross each other. As the main structure for trapping, it uses a straight wire of 80 μm width on the most external chip layer along the longitudinal x axis, in conjunction with a pair of perpendicular (along y) wires on the deeper layer, of 500 μm width, responsible for the weak longitudinal confinement. Finally, 10 μm-wide wires running alongside the main wire are used as antennae for radiofrequency dressing (Section 3.3).
The atom chip wires are much thinner than the copper wires underneath and can carry currents up to 1 A. The current driver for each wire is floating and connected

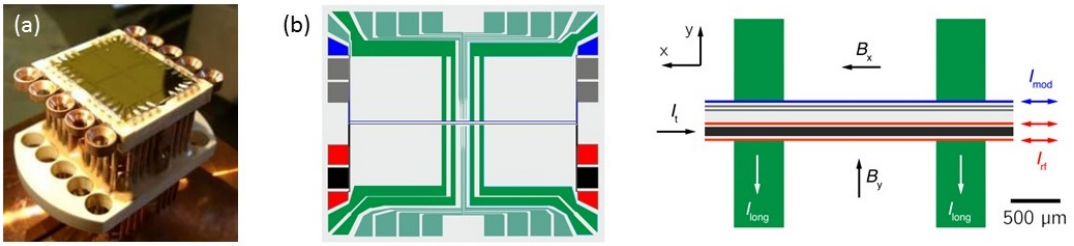

Figure 3.2: Adapted from Ref. [56]. (a) The atom chip. (b) Schematics of the wire structure of the most external layer used to generate the final chip trap. Left: an overview. The connection pads are placed all around the chip except in the central regions to avoid obstruction of imaging beams. Red, green, and black pads correspond to the wires used in this thesis. Right: zoom on the central part, where the actual experiment occurs. Black: main trapping wire. Green: longitudinal confinement wires. Red: radiofrequency wires. Blue: not used.

to an independent set of car batteries ($\pm$12 V) to supply the wire and the current source. When used continuously, the car batteries need to charge every week or when the voltage reaches 12 V.

3.1.6 Laser system

Lasers are a fundamental ingredient in every ultracold atom setup, which allowed physicists to achieve all the steps needed to go from a gas of neutral atoms at room temperature to a quantum condensate. They serve many tasks, from slowing down the atoms emitted by the rubidium dispensers, cooling and gathering them below the atom chip's surface, to optical pumping them in the right magnetic state for the following magnetic trapping stage (see Section 3.2). Furthermore, they detect the atoms after they have been released from the chip trap (see Section 3.4).
In the Rb2 setup there are two main lasers, one addressing the lowest hyperfine state of ^{87}Rb ($F = 1$), internally referred to as *repumper laser*, and the other addressing the second hyperfine ground state ($F = 2$), referred to as *cooler laser*, as showed in Fig. 3.3. Both cooler and repumper lasers originate from an ECDL structure. Only the cooler laser is amplified with a MOPA system before being injected into a single-mode fiber.
All the laser beams in the experiment come from a frequency-shifted cooler or repumper beam. Frequency shifting is done via single or double-pass acousto-optic modulators (AOMs).
A scheme of the laser setup is shown in Fig. 3.4. The cooler laser (red) and the repumper laser (orange) are generated in separate boxes for thermal and acoustic isolation. Both lasers undergo free-Doppler spectroscopy, and then the cooler undergoes two amplification stages. In July 2018, we exchanged the tapered-amplified (TA) laser chip at the first amplification stage. We currently operate the TA at 1240 mA and produce around 130 mW of optical power from the optical fiber: 90 mW is used for imaging (absorption and light-sheet beams) and pumping $F = 2$; 40 mW is used to seed a second amplification system, referred to as BoosTA[4]. We currently operate the BoosTA at 1850 mA of current, which outputs around 600 mW of optical power at the exit of the optical fiber, devoted to the MOT beams entirely.
The repumper beam outputs around 35 mW at the exit of the first optical fiber and

[4]Toptica Photonics BoosTA

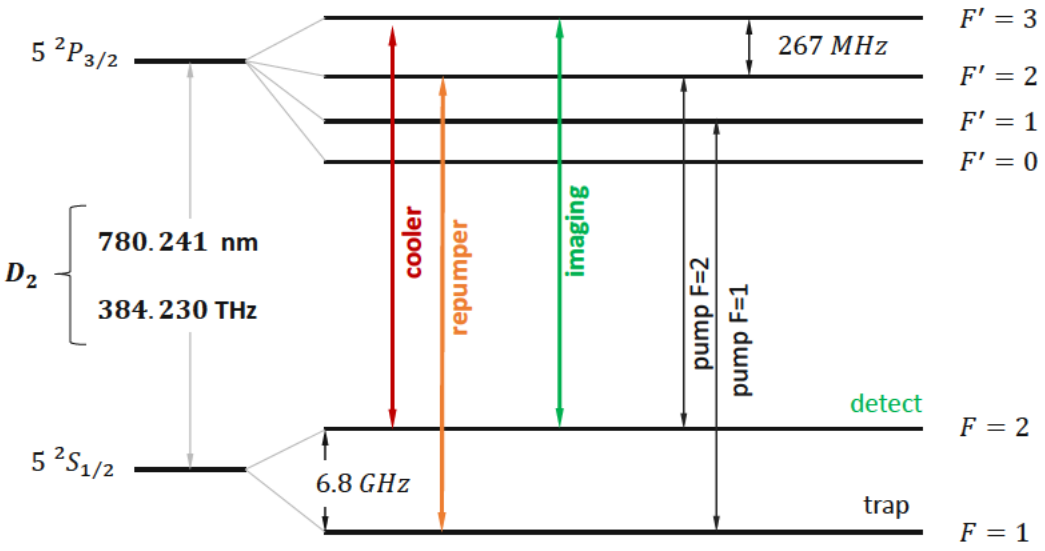

Figure 3.3: D_2 line of ^{87}Rb. More information on rubidium can be found in [58].

does not require any further amplification. It is used to repump the atoms into the cycling transition $F = 2 \rightarrow F' = 3$ during the MOT and molasses phase and bring atoms back into the imaging transition later on during detection. Part of the repumper beam serves as a pump for the $F = 1 \rightarrow F' = 1$ transition, which enables optical pumping into the trappable state $|F = 1, m_F = -1\rangle$.

3.1.7 External coils

Lasers alone are not enough to cool down atoms, and we use external magnetic fields produced by external coils placed all around the science chamber to support lasers in the MOT phase and later in the atom chip phase. Because of the different magnitude of the magnetic fields required at these two different stages of the experimental cycle, two sets of coils of different sizes are present in the experiment. They are arranged in a Helmholtz configuration and can generate homogeneous magnetic fields in all the spatial directions to complement the inhomogeneous fields from the atom chip. The first set (six coils, a pair for each spatial direction) comprises thicker coils that generate fields up to tens of Gauss of intensity, internally referred to as "Big" coils/fields. The second set (six coils in all directions) generates fields up to a few Gauss, internally referred to as "Small" coils/fields.

3.1.8 Radio-frequency electronics

In Rb2 we use a combination of static and oscillating radiofrequency (rf) fields [59]. A Hamiltonian with uncoupled adiabatic eigenstates, so-called dressed states [60], describes the atoms under the influence of the combined magnetic fields. Using such adiabatic dressed states potentials, we can achieve well-controlled coherent splitting and simultaneous tight confinement of the atomic motion, even far away (several tens of microns) from the chip surface.
Modulated currents are produced using digital arbitrary waveform generators[5]. Re-

[5]Tabor Electronics

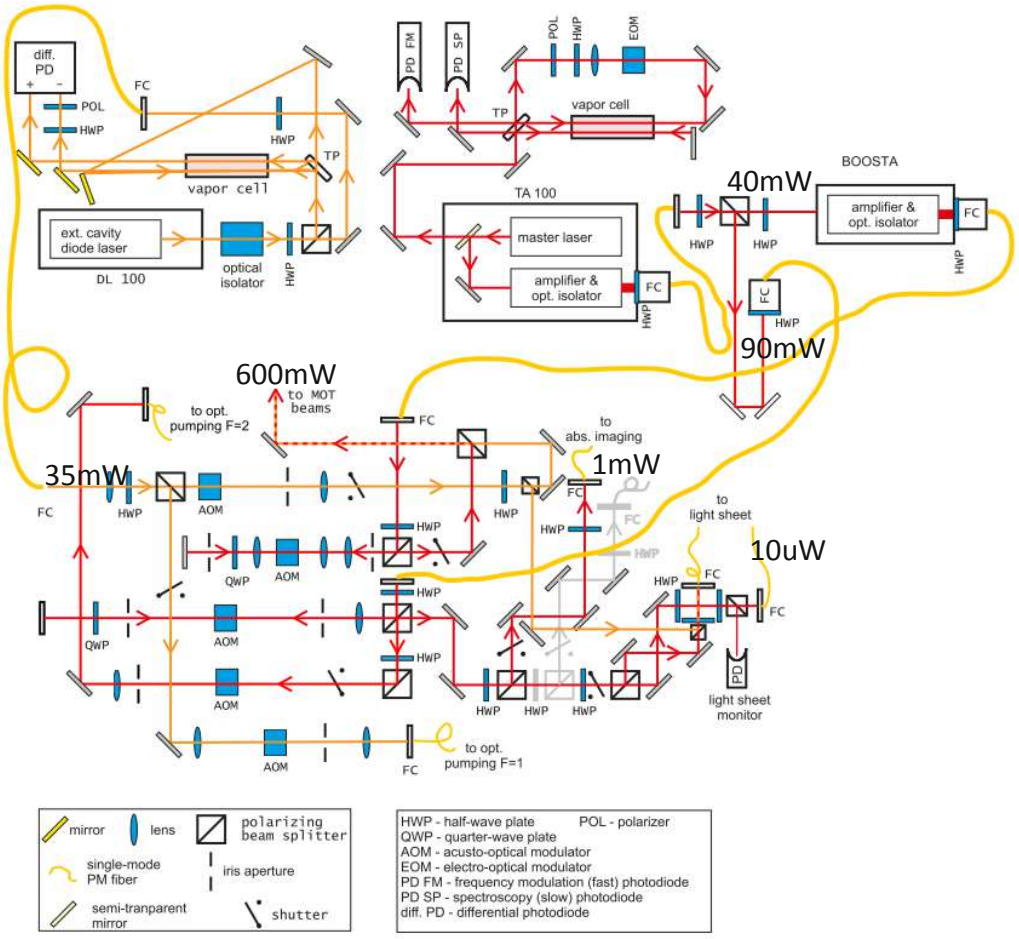

Figure 3.4: From [57]. The beam paths of the cooler (red) and repumper (orange) lasers are indicated. The grayed-out part corresponds to a previously used longitudinal absorption-based imaging scheme, not used anymore. On the upper part of the panel, we see the two beams that are generated in separate boxes for thermal and acoustic isolation. Doppler-free spectroscopy is performed on both beams[3]. The beams are then amplified and brought to the lower panel via single-mode polarization-maintaining fibers. On the lower panel, the beams are frequency shifted using AOMs and finally guided to their final locations, either in free-space (MOT) or single-mode fibers (imaging, optical pumping).

cently a new device replaced the Tabor instruments[6]. The oscillating currents of different amplitudes and frequencies are sent to the U-shaped copper wire for evaporative cooling, and to the two radiofrequency wires on the atom chip for radiofrequency dressing (see Fig. 3.2).
The modification of the potential is achieved by rf fields oscillating at a frequency resonant with the energy difference among the magnetic sublevels of the hyperfine ground state of ^{87}Rb. In the case of evaporative cooling, we employ an rf field with constant amplitude and ramp down the rf frequency until the hotter atoms have left the trap. During the rf dressing stage, we instead send out a fixed rf frequency and vary the amplitude according to the optimal trajectory or OCT ramp (see Section 4.2.2 and Fig. 4.4).

3.2 Preparation of quasi-condensates

Each experimental cycle lasts approximately 34 s. Each time the cloud is loaded and imaged, it is lost under gravity, and the cycle starts again iteratevely. The sci-

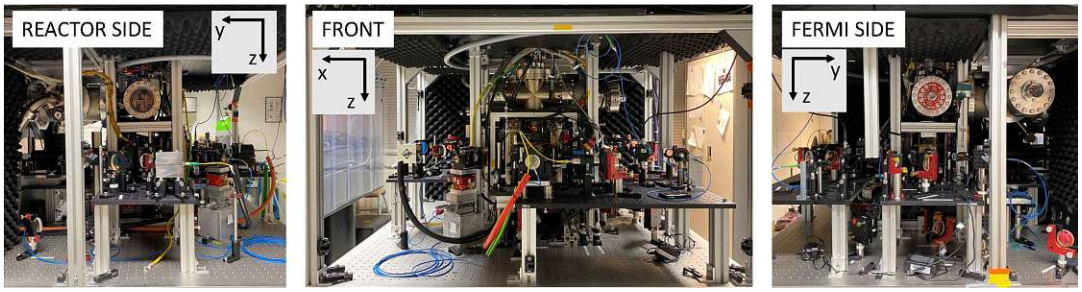

Figure 3.5: Picture of the experiment, the science chamber, and elements surrounding it from different points of view: front, reactor side (side facing the nuclear reactor facility at the Atominstitut), fermi side (fermi is the way we internally refer to the lab next door). The x,y, and z axis are defined with respect to the main experimental components.

ence chamber is where the experiment takes place. It is kept at ultrahigh vacuum at around 10^{-11} mbar (during the MOT phase, the pressure is higher) and has several windows to optically access its central core where the cold atomic ensemble is.
A Magneto-Optical Trap (MOT) is used to collect, trap and slow down rubidium atoms from the background vapor. The atoms are then cooled down and moved up by optical molasses and then optically pumped to the weak field seeking state $|F = 1, m_F = -1\rangle$ of ^{87}Rb. The Z-shaped wire from the copper structure creates a magnetic Ioffe-Pritchard trap that traps the cold atoms from the molasses. After a first compression and evaporative cooling stage within the Z-trap, the atoms are transferred to the atom chip trap and undergo a further evaporative cooling stage. Eventually, the condensate is released, atoms fall under gravity, and are finally detected in time-of-flight (TOF), either by absorption or fluorescence imaging techniques.
In Fig. 3.5 we show an overview of the current Rb2 setup, from different orientation, denoted, from left to right, “Reactor side”,“Front view”, and “Fermi side”. The experiment lies in a single optical table and comprises two parts: lasers are prepared and fiber injected on one half of the optical table; on the other half, the experiment takes place in the octagonal science chamber.

[6]Keysight 33622A.

3.2.1 Theory of magnetic trapping of neutral atoms

Let us now review the physics behind static magnetic traps. In general, the interaction of a magnetic dipole moment $\vec{\mu}$ of an atom with an external magnetic field $\vec{B}$ can be expressed as (see [58]):

$$H_B = \frac{\mu_B}{\hbar}(g_S\vec{S} + g_L\vec{L} + g_I\vec{I}) \cdot \vec{B}, \tag{3.1}$$

which leads to a ground state energy shift given by:

$$\Delta E_B = \vec{\mu} \cdot \vec{B}, \tag{3.2}$$

where Bohr's magneton is given by $\mu_B = e\hbar/(2m_e) \simeq h \cdot 1.4$ MHz/G with m_e the electron mass, and μ the atom magnetic moment defined by the relation:

$$\vec{\tau} = \vec{\mu} \times \vec{B}, \tag{3.3}$$

where we introduced the torque $\vec{\tau}$ exerted on the atom by the external field $\vec{B}$.
Maxwell's equations restrain the search of trappable states to low-field seekers, i.e., atomic states for which the state with lowest energy corresponds to the magnetic dipole moment $\vec{\mu}$ being anti-parallel to the external field $\vec{B}$.
If the magnetic moment $\vec{\mu}$ of the atom has a component perpendicular to the external field, the atom undergoes a Larmor precession around the external magnetic field due to the torque $\vec{\tau}$ with a frequency given by:

$$\omega_L = g_F\mu_B|\vec{B}|/h, \tag{3.4}$$

known as Larmor frequency. Since the field orientation changes in space, the atom will see a change of $\vec{B}$ as it spins around it. The adiabaticity criterion states that if the relative change of the magnetic field is small compared to the Larmor frequency, i.e., if the condition:

$$|\partial\vec{B}/\partial t| < \omega_L|\vec{B}|, \tag{3.5}$$

holds, then the atom's precession can follow the external field adiabatically, which means the atom will remain in its magnetic substate m_F even if the quantization axis will continuously rearrange its direction following the magnetic field orientation. In this case, the interaction takes the form of a potential:

$$V_{mag}(\vec{r}) = m_F g_F \mu_B |\vec{B}(\vec{r})|, \tag{3.6}$$

where F, m_F are the hyperfine quantum number and its projection along the quantization axis, and g_F is the hyperfine Landé factor given by (see [58]):

$$g_F \simeq g_J \frac{F(F+1) - I(I+1) + J(J+1)}{2F(F+1)}. \tag{3.7}$$

The hyperfine structure of ^{87}Rb in its ground state ($5^2S_{1/2}$) is given by (see [58]):

$$H_{hfs} = A_{hfs}\vec{I} \cdot \vec{J}, \tag{3.8}$$

which leads to a ground state hyperfine energy splitting:

$$\Delta E_{hfs} = \frac{1}{2}A_{hfs}K \simeq 6.8\,\text{GHz}, \tag{3.9}$$

where

$$K = F(F+1) - I(I+1) - J(J+1), \tag{3.10}$$

and A_{hfs} is the magnetic dipole constant. Depending on the intensity of the magnetic interaction, different regimes occur. If the energy shift ΔE_B due to the interaction with the external magnetic field is small compared to the energy scale of the hyperfine structure (F, m_F) of the ground state of ^{87}Rb atoms, we can treat H_B as a perturbation of the zero-field eigenstates of the hyperfine Hamiltonian H_{hfs}, so the interaction Hamiltonian becomes:

$$H_B = \mu_B g_F \vec{F} \cdot \vec{B}. \tag{3.11}$$

The corresponding energy splitting (to lowest order) is given by:

$$\Delta E_{|F,mF\rangle} = \mu_B g_F m_F B, \tag{3.12}$$

which is known as *anomalous Zeeman effect*.
For increasing values of the external magnetic field, a more general formula is available in an explicit form to compute the energy levels in the $J = 1/2$ ground state of the ^{87}Rb manifold, known as *Breit-Rabi formula* [58]:

$$\begin{aligned} E^{+}_{|Jm_J Im_I\rangle} &= -\frac{\Delta E_{hfs}}{2(2I+1)} + g_I \mu_B (m_I + 1/2)B + \frac{\Delta E_{hfs}}{2} F^{+}(x), \\ E^{-}_{|Jm_J Im_I\rangle} &= -\frac{\Delta E_{hfs}}{2(2I+1)} + g_I \mu_B (m_I - 1/2)B - \frac{\Delta E_{hfs}}{2} F^{-}(x), \end{aligned} \tag{3.13}$$

where $m_I = (-3/2, -1/2, 1/2, 3/2)$ are the projections of the nuclear magnetic moment quantum number I along the quantization axis, $g_I = -0.000995$ is the nuclear g-factor, and $F^{\pm}(x) = \sqrt{1 + \frac{4(m_I \pm 1/2)x}{2I+1} + x^2}$ where we defined:

$$x = \frac{(g_J - g_I)\mu_B B}{\Delta E_{hfs}}. \tag{3.14}$$

In Fig. 3.6, we display the level structure of ^{87}Rb lowest manifold as a function of an external magnetic field B, as prescribed by Eq. (3.13) (apart from the lowest state in the upper manifold for which we used the formula given by [58] for the Paschen-Back regime). In green, we show the states that can be trapped in the minimum of a static magnetic potential landscape (low-field seekers). It is possible to distinguish a weak-field region where F is still a good quantum number (anomalous Zeeman effect regime), followed by an intermediate region of magnetic field values where the different hyperfine states mix and I, J become the good quantum numbers (Breit-Rabi formula for the hyperfine states). For even larger magnetic field values, the hyperfine Hamiltonian of Eq. (3.8) perturbs the strong-field eigenstates $|Jm_J Im_I\rangle$, known as *Paschen-Back regime*.
We exploit the magnetic interaction of atoms in their ground state with an external field to generate magneto-optical or purely magnetical trapping schemes. For ^{87}Rb atoms only the states $|F = 1, m_F = -1\rangle$, $|F = 2, m_F = 1\rangle$, and $|F = 2, m_F = 2\rangle$ (in green and red in Fig. 3.6) can be used to trap atoms in free space around regions where the field modulus presents a local minimum. In the Rb2 experiment, we trap the ground state $|F = 1, m_F = -1\rangle$ (in red in Fig. 3.6) to whom corresponds a magnetic moment $\mu = m_F g_F \mu_B = 0.70$ MHz/G.
Let us now review some possible trapping geometries for neutral atoms with a finite magnetic moment in an external static magnetic field. The simplest trapping scheme

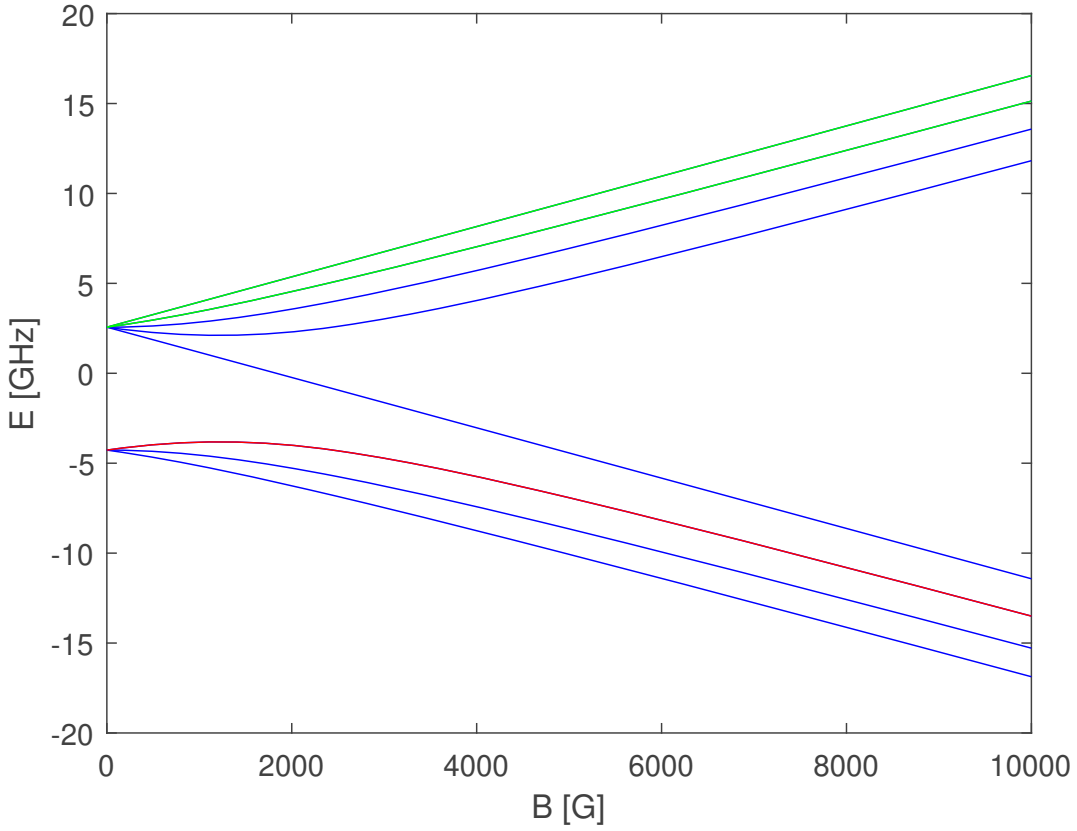

Figure 3.6: Energy structure of ^{87}Rb hyperfine ground states in the presence of an external magnetic field, calculated using Eq. (3.13). The energy of the lowest state of the upper manifold was calculated using the Paschen-Back formula [58]. In green and red are the low-field seeking states. In red is the state we used to trap atoms during this thesis.

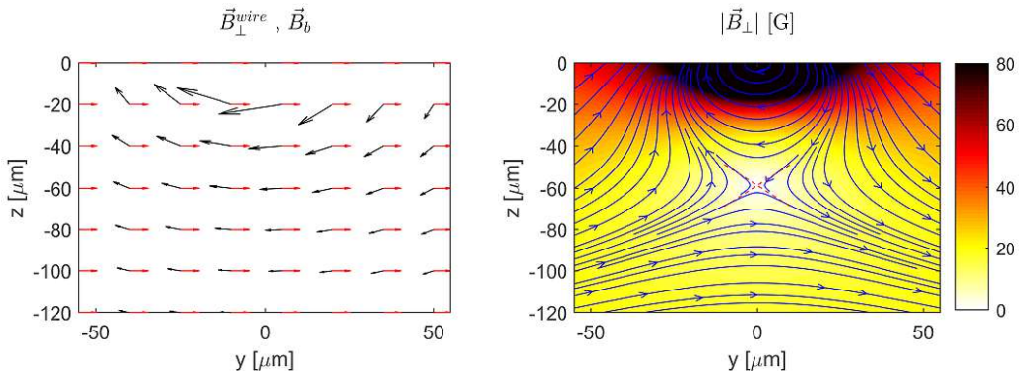

Figure 3.7: **Static transverse yz trapping scheme. Left:** Magnetic field distribution $\vec{B}_\perp^{wire}$ generated by an infinite wire running along x (direction of the current flow entering the page, x axis not drawn) and positioned at $(y,z) = (0,0)$, calculated using the Biot-Savart's law of Eq. (3.15) (in black); uniform magnetic bias field $\vec{B}_b$ along y axis (in red). **Right:** Modulus of the magnetic field distribution resulting from an infinite wire along x and a uniform field along y, producing a quadrupole field centered at $d_0 \simeq 60$ μm, assuming a value of $B_b = 34.1$ G and $I = 1$ A (typical values of the final chip trap).

is a quadrupole trap. The main idea is that for the transverse yz part, the inhomogeneous field generated by a single current-carrying wire is canceled by an external field (bias field) at one position in the yz plane. An extra homogeneous field along x will realize the Ioffe-Pritchard radial trap by lifting the zero-field minimum (Ioffe field) to avoid atom losses due to Majorana spin flips.

Transverse confinement Assuming an infinitely thin wire carrying a current i_t along x, the absolute value of the magnetic field B_{wire} generated at a distance d is given by:

$$B_{wire} = \frac{\mu_0}{2\pi}\frac{i_t}{d}, \tag{3.15}$$

known as the Biot-Savart's law.

Adding a homogeneous bias field of modulus B_b along y cancels the transverse field at a distance d_0 given by:

$$d_0 = \frac{\mu_0 i}{2\pi B_b}. \tag{3.16}$$

Around this zero-field minimum, a two-dimensional quadrupole configuration is generated with axes tilted by 45° with respect to y,z (see Fig. 3.7) with a field gradient given by:

$$|\partial B/\partial y| = |\partial B/\partial z| = |B_b/d|. \tag{3.17}$$

For typical parameters in the final atom chip trap, $B_b = 34.1$ G, $i = 1$ A, we find $d = 58.6$ μm and transverse field gradients $|\partial B/\partial y| = |\partial B/\partial z| = 0.6$ G/μm.

A simple quadrupole configuration with the value of the magnetic field modulus growing linearly in all directions starting from a local zero-field minimum must be excluded because of Majorana losses. Since the quantization axis has no definite orientation in space around the zero-field value at the trap's center, atoms can quickly escape into other magnetic states and be lost. A widespread solution is the Ioffe-Pritchard trap, which is also implemented in Rb2. It consists of a transverse quadrupole trap that superimposes a homogeneous field B_I along the longitudinal x axis, produced by the Ioffe coils. This extra Ioffe field B_I will determine the lowest

Larmor frequency experienced by the atoms in the trap, internally referred to as *trap bottom*.
The total harmonic potential in the transverse $\perp$ direction is then given by:

$$V_\perp(y,z) = V_0 + \frac{1}{2}m\omega_\perp^2(y^2+z^2), \tag{3.18}$$

with

$$V_0 = \mu B_I, \tag{3.19}$$

$$\omega_\perp = \sqrt{\frac{\mu}{m}}\frac{B'}{\sqrt{B_I}} \propto \frac{B_b^2}{i_t\sqrt{B_I}}, \tag{3.20}$$

where $B_I = 1.18$ G is the modulus of the magnetic field at the trap center, to which corresponds a trap bottom $\omega_0 = V_0/h \approx 824$ Hz, and $\omega_\perp \approx 2\pi \times 4.14$ kHz.
The chip trap allows much stronger confining traps than geometries using only external coils, exploiting the tiny distances (a few tens of micrometers) achievable between the trapping wires and the atoms. In order to increase the trapping frequency, it is simply necessary to move the trap center closer to the chip by varying the bias field intensity. In particular, higher bias fields achieve a cancellation of the trapping wire magnetic distribution closer to the atom chip surface, at a location where the transverse magnetic field gradients are higher (see Eq. (3.17) and Fig. 3.7).
Longitudinal confinement The trapping scheme discussed above produces an atomic waveguide with tight and isotropic transverse confinement in the yz-plane. The most common solution to trap atoms along the longitudinal x direction is to use a pair of wires located at a distance $L/2$ on each side of the main trapping wire and orthogonal to it. Let us discuss the case of the final trap and then see the variations of this scheme used during the U-MOT and Z-trap phases in their sections.
During the final chip trap, Rb2 uses a pair of H-wires running along y at a distance $L/2 = 1$ mm from the trap center. When a current i_H is sent through each of them with the same orientation, a field along x is produced, which gives rise to a magnetic potential $V_H(x) = V_{TB} + \frac{1}{2}m\omega_x^2x^2$ with

$$V_{TB} = g_F m_F \mu_B (B_0 + \frac{4d\mu_0 i_h}{\pi L^2}), \tag{3.21}$$

$$\omega_x = \sqrt{\frac{g_F m_F \mu_B}{m}}\frac{4\mu_0}{\pi L^2}\frac{i_H}{\sqrt{B_0}} \propto \frac{i_H}{\sqrt{B_0}},$$

provided $z, d \ll L$. Since L is much larger than the other length scales, the longitudinal potential is much more shallow. The total three-dimensional trap can then be approximated by an elongated harmonic potential. For typical current $i_H = 0.5$ A along the H-wires, we get a 10% correction to the trap bottom due to the longitudinal confinement and a typical longitudinal trapping frequency $\omega_x = 12$ Hz, which yields an aspect ratio $\omega_\perp/\omega_x \sim 200$.

3.2.2 U-MOT and molasses

In the first half of the cycle (18 s) the dispensers of rubidium atoms are heated up and the gas is liberated into the chamber. At the same time, lasers and uniform magnetic fields are switched on and are used to pre-cool the background vapor in a magneto-optical trap (MOT) a few centimeters below the atom chip.
The laser beams used for the MOT phase are four beams tuned to the $F = 2 \leftrightarrow F' = 3$ closed transition of the D2 line of the atoms (see Fig. 3.3). Because one direction in

space is occupied by the atom chip, we make use of a mirror U-MOT configuration [61], where two of the six beams used in a conventional MOT are replaced by the reflections off the chip surface of two beams impinging at an angle of 45°.
The transverse quadrupole field is approximated by the current running through the U wire together with a homogeneous bias field parallel to the wire plane and perpendicular to the central bar of the U connector. The bias field can be rotated in the plane parallel to the wire and this will move the trap minimum, but the field always vanishes at the trap minimum [62]. Along the longitudinal direction, the minimum of the potential is displaced from the central point of the bar, in a direction opposite to the location of the side wires. A more symmetric quadrupole can be created by using three wires in an H configuration, as for the final atom chip trap.
An additional laser beam, the repumper beam, tuned with the $F = 1 \leftrightarrow F' = 2$ optical transition is superimposed with the goal of bringing back in the cooling transitions atoms that fell in the dark $F = 1$ state (see Fig. 3.3).
MOT beams and fields are on for 17 s, then the MOT is held in place for 1.5 s during which dispensers are switched off and the residual gas is pumped away by the vacuum pumps to avoid collisions with the trapped atoms. Moreover the optical power of the MOT beams is decreased to reduce the effect of light-induced collisions within atoms.

3.2.3 Magnetic Z-trapping and evaporative cooling

After the U-MOT phase where only lasers and external coils are involved, atoms are optically pumped into the $|F = 1, m_F = -1\rangle$ state, which is one of the low-field seekers of the ^{87}Rb ground state manifold (Fig. 3.6).
The Z-shaped wire within the copper structure below the atom chip is ramped up together with an external bias field (Big bias) to achieve a three-dimensional Ioffe-Pritchard trap. In fact, due to the wire's shape, the currents of the side bars now add up instead of canceling each other like in the U geometry, leading to a non-vanishing field minimum [62]. However, since the absolute field magnitude at the trap bottom is too high, a counterbalancing anti-Ioffe field is superimposed in the opposite direction [53].
In order to further cool down the atomic ensemble, an oscillating radiofrequency field tuned with the splitting energy between the different Zeeman substates removes the hotter[7] atoms from the trap. The remaining atoms collide and rethermalize to a lower temperature. The rf field is continuously ramped down to lower frequencies in order to remove more and more atoms, thus reaching lower temperatures.
The U-shaped wire is used as a rf antenna because of its vicinity with the atoms position. The resolution of this method is limited by the chemical potential of the BEC to $\simeq 2$ kHz [63].

3.2.4 Atom chip phase

The main trapping wire together with the H-shaped wires running perpendicularly achieve a Ioffe-Pritchard trapping scheme, where the Ioffe field points along the same direction of the field along x generated by the H wires. The H wires are located at a distance $L/2 = 1$ mm on each side of the main trapping wire. Typical parameters for the currents used are $i = 1$ A for the main wire, and $i_H = 0.5$ A for the H wires,

[7] With higher kinetic energies.

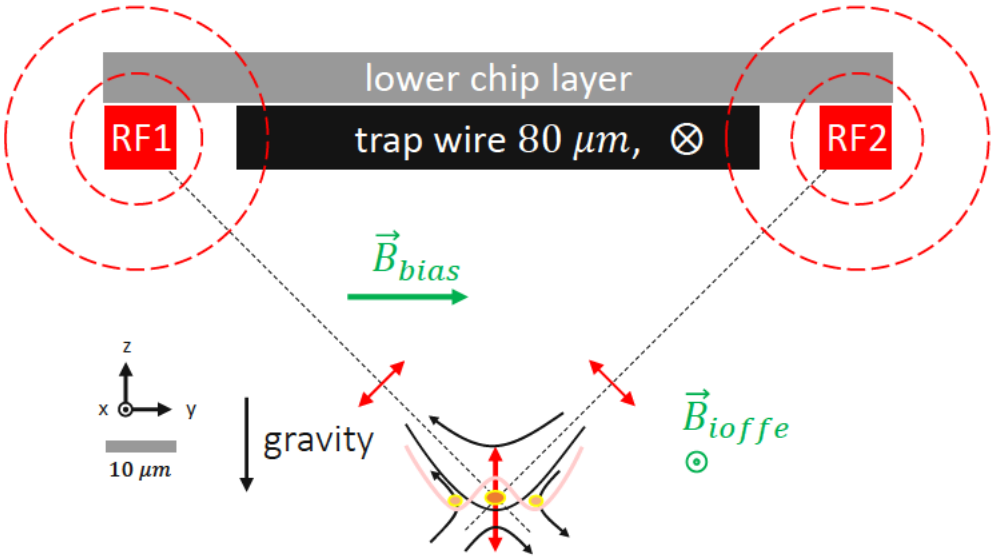

Figure 3.8: Schematics of the atom chip layout. A current i_t along the main trapping wire (80 μm wide) together with the external homogeneous bias field $\vec{B}_{bias}$ along y (quadrupole potential) and Ioffe field $\vec{B}_{ioffe}$ along x make up a nearly harmonic trapping potential (black curve). Broad wires along y and placed at a distance $L/2 = 1$ mm on each side of the trap center provide the longitudinal confinement (not drawn, see Fig. 3.2. Oscillating radiofrequency dressing currents are sent to the rf wires RF1, RF2 wires (10 μm wide) parallel to the main wire, leading to a radiofrequency field polarization along z (red arrows). The rf fields are responsible for the dressed states potential and, ultimately, when a certain rf amplitude is reached, lifting up a barrier at the center of the static potential allows the adiabatic splitting of a single waveguide to a double waveguide for atoms (red curve).

while for the homogeneous external fields we have $B_b = 34.1$ G for the bias field, and $B_0 = 1.07$ G for the Ioffe field.
With these settings an elongated trap is produced, that has a trap bottom $\nu_{TB} \simeq 820$ kHz, a perpendicular trap frequency $\omega_\perp = 2\pi \times 4.14$ kHz, and a longitudinal trap frequency $\omega_\parallel = 2\pi \times 12$ Hz.

3.3 Radio-frequency dressing

As we saw in the previous section, static magnetic field distributions can be used to trap neutral atoms and achieve tightly confining traps. However, if the goal is to efficiently and adiabatically split the harmonic trap into two separate potential wells, static fields alone present some disadvantages. Most importantly, the resulting potential will not be very tight (a factor 500 less compared to atom chip-based traps) [59, 63]. Coherent splitting and recombination of matter waves were demonstrated in [60] using a combination of static fields and oscillating radiofrequency (rf) fields fully integrated on an atom chip.
In magnetic radiofrequency dressing we couple the magnetic substates of an hyperfine state, in our case the Zeeman levels of the $F = 1$ manifold, separated by around 700 kHz. Let us review in some detail the physics behind rf induced adiabatic dressed states potentials following [56, 57, 59], starting from the Rb2 experi-

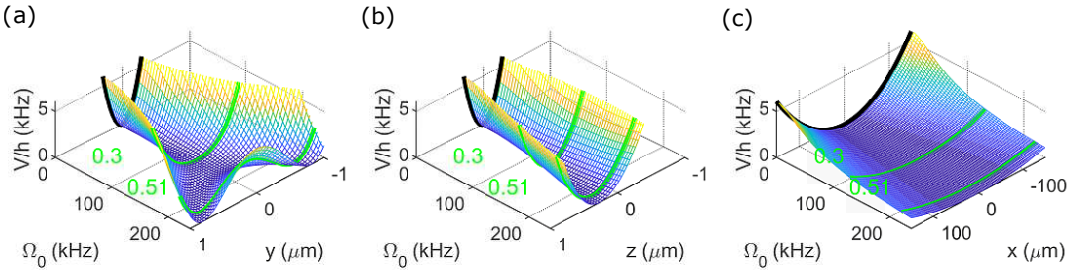

Figure 3.9: Effects of rf dressing on the three spatial directions. (a) Potential along the double-well y direction in rotating wave approximation, as a function of the coupling strength at the trap bottom Ω_0. The static trap is displayed for comparison (black curve). Highlighted in green the potential curves at $R_f = 0.3$ and $R_f = 0.51$, respectively the first and the final traps created during the optimal control ramp to initialize the source state in the DTB sequence (see Chapter 4). (b) Potential along the vertical z axis in rotating wave approximation, as a function of the coupling strength at the trap bottom Ω_0. All the curves have the same meaning as in (a). From this plot, we can see how a tight single wave guide confinement is maintained at all times along the vertical z axis during the DTB sequence. (c) Potential along the longitudinal x axis. Notice the much larger range of 100 μm used. Here the potential is much more shallow compared to the transverse directions.

mental configuration in Fig. 3.8.
As we couple magnetic substates of an atom trapped in a static, spatial varying magnetic field landscape $B_S(\vec{r})$ to an oscillatory field $\vec{B}_{RF}(\vec{r},t)$ with frequency ω, the resulting potential landscape is given by:

$$V_{RF}(\vec{r}) = h\sqrt{\delta^2(\vec{r}) + \Omega^2(\vec{r})} \tag{3.22}$$

with detuning $\delta(\vec{r}) = \nu_L(\vec{r}) - \nu(\vec{r})$ from the atoms' Larmor frequency at the trap bottom ω_L, and coupling strength or Rabi frequency $\Omega(\vec{r}) = \frac{1}{2}\mu_B \widetilde{m}_F B_{RF,\perp}(\vec{r})$, where $B_{RF,\perp}(\vec{r})$ represents the perpendicular component of the rf field with respect to the local static field. We can also define the Rabi frequency at the trap bottom $\Omega_0 = \frac{1}{2} g_F \widetilde{m}_F \mu_B B_{RF,0}$, where $B_{RF,0}$ is the magnitude of the perpendicular component of the rf field with respect to the static field.
The static potential is approximately harmonic and isotropic along the transverse axis in the yz plane. When the rf amplitude is increased (with a constant frequency), the potential becomes anisotropic and flattens along a direction that depends on the polarization of the rf field [57]. The dressing is only along the direction perpendicular to the rf polarization. Typical parameters for the rf dressing in our experiment are an rf field of $B_{RF} \approx 0.68$ G peak-to-peak amplitude ($R_f = 0.51$, see Section 4.2.2), corresponding to a coupling $\Omega_0 \approx 220$ kHz, at a frequency red-detuned by $\delta_0 = -54$ kHz near the trap bottom with $\nu_L = 824$ kHz.

3.4 Detection

3.4.1 Absorption imaging

Absorption imaging is used to estimate the atom number of the ultracold ensemble. We recently replaced the old camera with a new one that communicates via a single cable with a computer. We currently take absorption pictures of the atoms with a

Table 3.1: Main specifications of the current absorption camera.

Quantum Efficiency at 780 nm	40 %
Resolution	2048 px x 1088 px
Max. Frames Per Second	165 fps
Pixel Size	5.5 μm x 5.5 μm
Dark Noise	13.9 e^-
Saturation Capacity	9.3 ke^-
Dynamical Range	56.5 dB
Signal-to-noise Ratio	39.7 dB

BASLER® acA2000-165 μm USB 3.0 camera featuring a CMOS sensor (CMV2000). In Table 3.1 we summarize its main features.
The sensor (with its housing for the reading out) was aligned on a mechanical trail comprising the previous lens system [64].
The number of atoms N_i on a pixel i of the CMOS sensor is given by [56]

$$N_i = \frac{A}{\sigma_S} \ln\left(\frac{S_{0,i}}{S_i}\right), \tag{3.23}$$

where $S_{0,i}$ and S_i correspond to the signal (arbitrary units) detected in that pixel with and without atoms (only light beam present), respectively. To achieve this result, two images are acquired, separated in time by 10 ms. A/σ_S is equal to the number of atoms in the pixel column required to achieve unit optical density. The value of the object-space pixel size $\sqrt{A}$ was measured to give $A = 11.8\ \mu m^2$ [56]. In the limit of low intensities and sigma polarized absorption beam, the value of σ_S was estimated to be $\sigma_S = 3\lambda^2/(2\pi) \approx 0.291\ \mu m^2$ [58].
A Matlab script was written to communicate with the new camera. Practically, we take two images with a 800 μs exposure time at specific time steps dictated by an external TTL signal controlled by an ADwin channel, one with and the second without atoms.

3.4.2 Fluorescence imaging

Our fluorescence-based imaging system consists of a nearly resonant sheet of light made of two counter-propagating laser beams with extremely thin focus (20 μm minimum radius) paired with a high-NA objective placed below the vacuum chamber and an EMCCD camera [8]. The thin light sheet serves as a selective element that avoids collecting photons from the cloud as a whole at the same time, which would result in a blurring effect due to layers that are not in focus. Instead, each slice is imaged separately, and the signal from different vertical layers gets summed up.
Fluorescence imaging is conceptually different from absorption imaging. Since it aims to collect the photons re-emitted by the atoms in the full solid angle, the detector can be placed at any location regarding the incident light. The portion of photons that can be collected with respect to the full solid angle makes up the geometrical factor $f_g = \frac{\Omega}{4\pi} \approx \frac{NA^2}{4}$, where Ω is the solid angle covered by the stop of the objective and NA the numerical aperture of the imaging system. Around 2% of all photons emitted by the atoms are collected on an EMCCD sensor placed below the atom chip and converted into electrons. The conversion factor amounts to typical values of $m =$ 10-30 photons detected per single atom for typical light-sheet power of

[8] Andor iXon+ 897

$\approx \mu$W. The photon-per-atom parameter m is crucial to converting the fluorescence signal detected with our light-sheet camera to atom numbers. In principle, single atom recognition is possible and was already demonstrated in this system [41]. In practice, due to deterioration and aging of the camera, the electronic signal has recently increased and made it extremely difficult to achieve single-atom detection. The imaging objective leads to a magnification of $M = 4$, which in turn gives an object-space pixel size of 4 μm, since the physical pixel area is 16x16 μm^2 [56].
If the two counter-propagating laser beams are not overlapping or their power is unbalanced, a light-pressure effect can appear in the fluorescence picture. We currently aligned the imaging system such that the focus corresponds to pictures being taken after a time-of-flight $t_{TOF} = 44$ ms.

Far-field regime for the transverse direction

The final position x_F of a trapped particle along a certain spatial direction x after its release from the trap at time $t = 0$ and a time-of-flight $t_{TOF} \equiv t_F$ reads $x_F = x_0 + \dot{x}_0 \cdot t_F = x_0 + p_0/m \cdot t_F$, where x_0 ($\dot{x}_0 = p_0/m$) represents the initial position (velocity) of the particle in the trap at the moment of the release and p_0 its initial momentum. Assuming a harmonic trapping ($\dot{x} = i\omega_x x$) with angular frequency ω_x along the x axis, we derive the expression $x_F = x_0 + i\omega_x x_0 \cdot t_F = x_0 + p_0/m \cdot t_F$. The condition of the final position expressing the initial momentum of the particle in the trap at the moment of the release is then $p_0/m \cdot t_F \gg x_0$, which translates into the requirement $i\omega_x x_0 \cdot t_F \gg x_0 \rightarrow t_F \gg 1/\omega_{x,y,z}$, independently of the spatial direction we are referring to.
In our experimental setup we have $\omega_x \simeq 2\pi \cdot 10$ Hz and $\omega_{y,z} = 2\pi \cdot 2$ kHz, which corresponds to $1/\omega_x \simeq 16$ ms and $1/\omega_{y,z} \simeq 0.1$ ms. Since in our setup $t_F = 44$ ms, the condition $t_F \gg 1/\omega_{x,y,z}$ is well satisfied along the transverse y, z axes and only partly satisfied along the x axis. This shows that the transverse expansion of the atomic cloud after its release from the chip trap is fast compared to t_{TOF}, hence the fluorescence image of the final cloud shows the in-situ momentum distribution along the y axis.

Chapter 4

Double twin-atom beams

This chapter introduces the main subject of this thesis work: the double twin-atom beams system and the quantum state originating from it.
In Section 4.1 we give a theoretical description of our system, starting from Ref. [56] and the more recent [65]; Section 4.2 presents the experimental procedure to generate the DTB atoms and Section 4.3 introduces the calculation from Igor Mazets that shows what output state we expect with our current trap geometry. Finally, in Section 4.4, we explain the main methods used for the analysis of the data in Chapter 5.

4.1 Theoretical background

The theoretical description of the system relies on Ref. [65]. The novelty of this thesis work is the use of double waveguide confinement for the twin atoms. This part is crucial to be able to generate a maximally entangled state.
Let us first consider a dilute 3d gas trapped in a waveguide potential $V(\vec{r})$. Considering only s-wave scattering events among the atoms inside the condensate, the general Hamiltonian describing the system reads:

$$\hat{H} = \int \mathrm{d}\vec{r} \left\{ \hat{\psi}^\dagger(\vec{r}) \left[-\frac{\hbar^2}{2m}\nabla^2 + V(\vec{r}) \right] \hat{\psi}(\vec{r}) + \frac{g_{3d}}{2} \hat{\psi}^\dagger(\vec{r})\hat{\psi}^\dagger(\vec{r})\hat{\psi}(\vec{r})\hat{\psi}(\vec{r}) \right\}, \tag{4.1}$$

where $g_{3d} = 4\pi\hbar^2 a_s/m$ describes the strength of the interactions characterized by s-wave scattering length a_s and atomic mass m.
To simplify the Hamiltonian of Eq. (4.1), we take into account the geometry of the trapping potential $V(\vec{r})$. The trapping potential constitutes an atom waveguide (the atoms are loosely confined along one direction but tightly confined transversally), which allows us to derive an effective one-dimensional model of the system's dynamics, where only the dependence on the spatial x direction is explicit. Considering the vibrational transverse energy levels $n_{y,z}$, the quasi-condensate is initially formed in the transverse ground state $(n_y, n_z) = (0, 0)$.
The experimental sequence used to generate double twin-atom beams (DTBs) involves an initialization stage, where the trapping potential is deformed along the y axis according to optimal control theory [66]. This allows to achieve a double-well configuration and, at the same time, *coherently* transfer the quasi-condensate from the vibrational ground state $(n_y, n_z) = (0, 0)$ to the second excited state $(n_y, n_z) = (2, 0)$ of the final double waveguide potential.
We now assume that the system is prepared in the $(n_y, n_z) = (2, 0)$ state. We can

expand the field operator of the quasi-condensate as

$$\hat{\psi}(\vec{r}) \equiv \sum_{m_x,n_y,n_z} \hat{a}_{m_x,n_y,n_z} \varphi_{m_x}(x)\phi_{n_y}(y)\phi_{n_z}(z), \tag{4.2}$$

where $\phi_{n_y}(y)$ [$\phi_{n_z}(z)$] is the harmonic oscillator basis function of the n_yth (n_zth) mode, $\varphi_{m_x}(x)$ are a set of basis function along the x dimension, and $\hat{a}_{m_x,n_y,n_z}$ the bosonic annihilation operator for the corresponding mode. A few assumptions are now made based on the cylindrical shape of the trapping potential. Since the dynamics along the vertical z direction are frozen-out, we hereafter assume $n_z = 0$ and suppress the corresponding subscript in the expansion of the bosonic field. Furthermore, we assume that only the levels $n_y = \{0, 1, 2\}$ are involved in the initialization and de-excitation stage. This assumption is justified by the anharmonicity introduced along the y axis, which brings out of resonance the energy levels with $n_y > 2$, and by symmetry reasons: the initialization ramp, which produces a barrier of the double-well and increases and decreases it iteratively until the ramp is finished, does this operation symmetrically with respect to the minima of the double-well; hence all terms involving the asymmetrical wavefunctions are drastically reduced during the initialization process. As explained in Section 5.1, this assumption is verified by looking at the evolution of the quasi-condensate wavefunction after the initialization stage. Suppose we substitute the expression of the expansion of the field operator back into Eq. (4.1). In that case, the assumptions above let us integrate the y and z dimensions to yield an effective 1D Hamiltonian. With the definition of the 1D field operator $\hat{\psi}_i(x) = \sum_{m_x} \hat{a}_{m_x,i,0}\varphi_{m_x}(x)$ where $i \equiv n_y = \{0, 1, 2\}$, we can write the 1D Hamiltonian $\hat{H} = \hat{H}_0 + \hat{H}_{int}$, where

$$\hat{H}_0 = \int \mathrm{d}x \sum_{i=0,1,2} \hat{\psi}_i^\dagger(x) \left[-\frac{\hbar^2}{2m}\frac{\partial^2}{\partial x^2} + V(x) + \delta_{i,2}\hbar\omega_y \right] \hat{\psi}_i(x), \tag{4.3}$$

is the single-body Hamiltonian, and

$$\begin{aligned}
\hat{H}_{int} = \int \mathrm{d}x \Bigg\{ & \frac{g_{00}}{2}\hat{\psi}_0^\dagger(x)\hat{\psi}_0^\dagger(x)\hat{\psi}_0(x)\hat{\psi}_0(x) \\
& + \frac{g_{11}}{2}\hat{\psi}_1^\dagger(x)\hat{\psi}_1^\dagger(x)\hat{\psi}_1(x)\hat{\psi}_1^\dagger(x) \\
& + \frac{g_{22}}{2}\hat{\psi}_2^\dagger(x)\hat{\psi}_2^\dagger(x)\hat{\psi}_2(x)\hat{\psi}_2^\dagger(x) \\
& + 2g_{01}\hat{\psi}_0^\dagger(x)\hat{\psi}_0(x)\hat{\psi}_1^\dagger(x)\hat{\psi}_1(x) \\
& + 2g_{02}\hat{\psi}_0^\dagger(x)\hat{\psi}_0(x)\hat{\psi}_2^\dagger(x)\hat{\psi}_2(x) \\
& + 2g_{12}\hat{\psi}_1^\dagger(x)\hat{\psi}_1(x)\hat{\psi}_2^\dagger(x)\hat{\psi}_2(x) \\
& + \frac{g_{01}}{2}\left[\hat{\psi}_0^\dagger(x)\hat{\psi}_0^\dagger(x)\hat{\psi}_1(x)\hat{\psi}_1(x) + h.c.\right] \\
& + \frac{g_{02}}{2}\left[\hat{\psi}_0^\dagger(x)\hat{\psi}_0^\dagger(x)\hat{\psi}_2(x)\hat{\psi}_2(x) + h.c.\right] \\
& + \frac{g_{12}}{2}\left[\hat{\psi}_1^\dagger(x)\hat{\psi}_1^\dagger(x)\hat{\psi}_2(x)\hat{\psi}_2(x) + h.c.\right] \Bigg\}
\end{aligned} \tag{4.4}$$

is the interaction Hamiltonian, where H.c. refers to the Hermitian conjugate and we defined the effective 1D coupling strengths as $g_{ij} = \int \mathrm{d}z[\phi_0^{(ho)}(z)]^4 \times \int \mathrm{d}y[\phi_i^{(ho)}(y)]^2 \int \mathrm{d}y[\phi_j^{(ho)}(y)]^2$.

The last terms in Eq. (4.4) describe the four-wave-mixing process at the basis of the bosonic pair-production. In particular, the relevant terms are the ones where two particles from the second excited state get emitted in the first excited state or in the ground state of the transverse manifold:

$$\hat{H}_{FWM} = \frac{g_{02}}{2}\int \mathrm{d}x\, \hat{\psi}_0^\dagger(x)\hat{\psi}_0^\dagger(x)\hat{\psi}_2(x)\hat{\psi}_2(x) + \frac{g_{12}}{2}\int \mathrm{d}x\, \hat{\psi}_1^\dagger(x)\hat{\psi}_1^\dagger(x)\hat{\psi}_2(x)\hat{\psi}_2(x) + \mathrm{H.c.} \tag{4.5}$$

This effective Hamiltonian describes the collisional de-excitation process, by which two atoms in the excited state $\left|n_y = 2\right\rangle$ relax to the almost degenerate first excited $\left|n_y = 1\right\rangle$ and ground state $\left|n_y = 0\right\rangle$. In doing so, they can convert the potential energy $2\hbar\omega_y$ from the strongly confining trap along y into kinetic energy along the weakly trapped longitudinal direction x [see Eq. (4.3)]. The remaining terms of Eq. (4.4) can be interpreted as spatially and time-dependent mean-field potentials in which the scattered atoms move in [65]. Assuming their energy contribution is small compared to the $2\hbar\omega_y$ energy term, their effect amounts to a general phase shift that can be ignored. Furthermore, due to the conservation of energy and approximately the momentum, the atom pairs scattered from the initial transverse excited state (where the atoms are at rest longitudinally) into the $\left|n_y = 0, 1\right\rangle$ states will then have counter-propagating longitudinal momenta $k_x \approx \pm k_0$, where k_0 is given by

$$k_0 = \sqrt{2m\omega_y/\hbar} = \sqrt{2m\epsilon}/\hbar, \tag{4.6}$$

where we defined the surplus potential energy ϵ. As we will see in Section 4.3, the degeneracy of the transverse final states $\left|n_y = 0, 1\right\rangle$ can be also represented in the left $|L\rangle$ and right well $|R\rangle$ state basis representation. This representation is the most natural one since we are here dealing with a double-well potential. Furthermore, the presence of an atom in the left or in the right well is at the basis of the qubit we want to produce. The other degree of freedom is given by the momentum assigned to each atom along the longitudinal direction, which, as we have seen, it can take approximately the two values $\pm k_0$.

4.2 Generating twin beams in a double wave guide

Double twin atom beams are produced by collisions among atoms in a one-dimensional BEC in a vibrationally excited state of a confining potential. The experimental procedure to realize such a configuration is illustrated in Fig. 4.1.
As we already have seen in Section 3.2, each experimental cycle lasts approximately 34 s. This chapter focuses on the experimental steps strictly related to the DTB generation alone and not common to any other experiment performed in this laboratory. In the following, we will divide the DTB sequence into three main steps or stages: a first part called *trap characterization* is necessary to adjust the initial potential landscape (single well); the main DTB step is the *state inversion*, where the potential (and the trapped BEC's wavefunction with it too) undergoes a series of controlled deformations computed by optimal control techniques, to transfer the atoms to the second excited state of the transverse vibrational manifold of the final double-well potential. In this way, the system is initialized for the generation of DTB pairs; a third part called *detection*, where we choose on which basis (position or momentum) we measure the atomic profiles and then image the atoms.

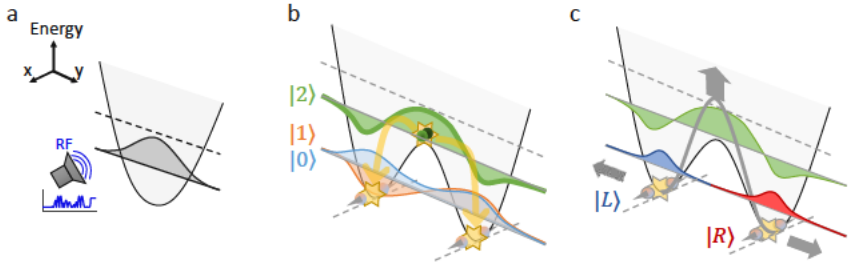

Figure 4.1: Sketch of the experimental procedure (detection step not represented). (a) The quasi-BEC (gray) lies initially in the transverse ground state of a single-well potential characterized by a tightly confined direction (y-axis or transverse axis) and a weakly confined direction (x-axis or longitudinal axis, potential curve along this axis not displayed). An rf field with variable amplitude is used to excite the condensate and reach a double-well configuration along the y-axis. (b) The final double-well potential with its vibrational states along the y-axis: the second-excited state (green), which constitutes the *source state*, the first-excited (orange), and the ground state (blue) are defined by the vibrational quantum number $n_y = \{0,1,2\}$. Two atoms from the source state can collide and decay into a twin pair (opposite momenta along the x-axis). Since the atoms in the twin pair can either be emitted in the symmetric $|0\rangle$ (blue) or the anti-symmetric $|1\rangle$ (orange) transverse state, we define the emitted two-particle state as *double twin-atom beam* (DTB) state. (c) The DTB state can also be expressed in terms of the localized left- $|L\rangle$ (blue curve) and right-well state $|R\rangle$ (red curve). The gray arrows represent the process of quickly lifting the barrier height and pushing the well's minima away from each other.

In the following, we will analyze more in detail these three fundamental steps for the generation of double twin atoms beams.

4.2.1 Trap characterization

We characterize the initial single well confinement employing two measurements: the Larmor frequency at the position of the minimum magnetic field (trap bottom) and the trap frequencies, characterizing the strength of the potential. The former is measured by radiofrequency spectroscopy: a short rf pulse is sent onto the atoms with variable frequency. It acts as a frequency selective knife that opens the trap for particles at varying frequencies by coupling them to untrapped substates. By checking the percentage of atoms left at different frequencies, we can deduce the trap bottom (see Fig. 4.2).
The second important parameter of the confining potential is its frequency along the transverse y axis direction. Here, we initiate sloshing dynamics for the atoms by suddenly changing the current running on a wire, and we record the position of their center of motion at different times (see Fig. 4.3).
Knowing these two parameters (together with the other two angular frequencies, which can be estimated similarly to ω_y) allows for characterizing the initial trap. In particular, the optimal control ramp of the rf field used to perform the state inversion mechanism to produce double twin atoms is strongly dependent on the initial trap bottom and transverse frequency. By changing the final Ioffe and bias fields, we can adjust these two initial parameters of the first trap until the trap configuration matches with the one used to optimize the ramp of the rf field for DTB generation. The parameters of the first trap are summarized in Table 4.1.

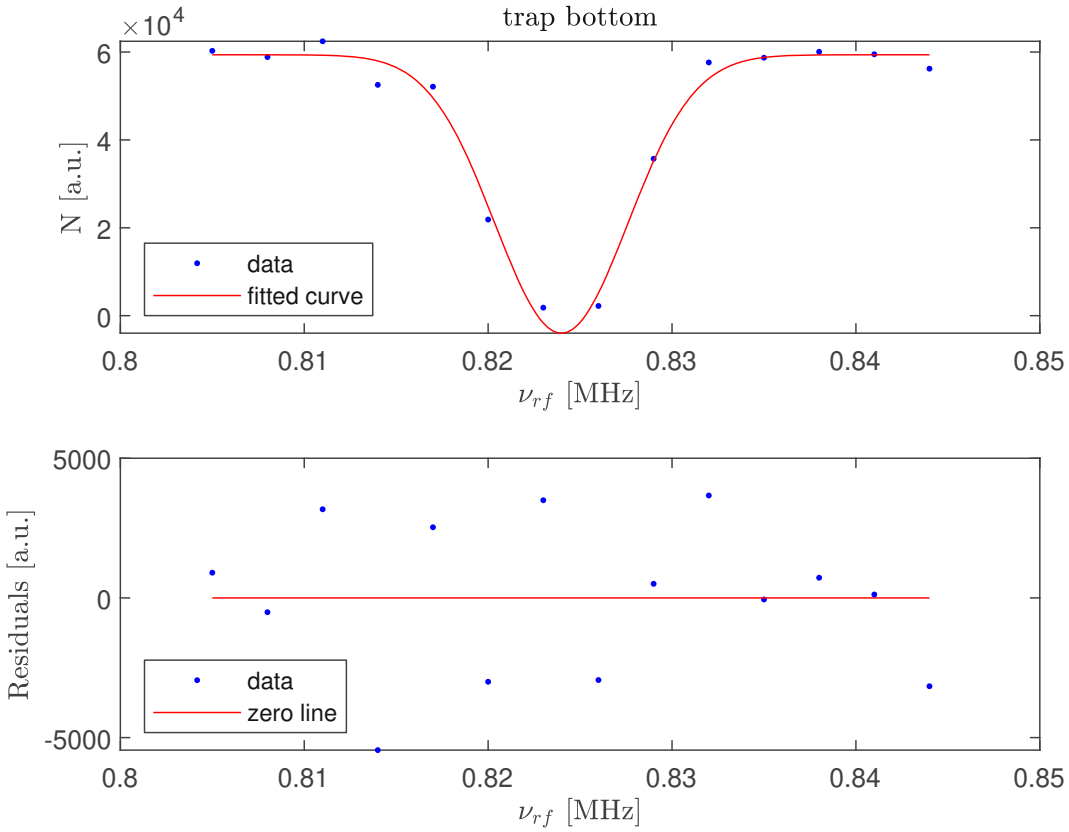

Figure 4.2: Trap bottom spectroscopy (upper panel). A weak rf pulse is applied to outcouple atoms from the trap resonantly. The maximum loss (dip) occurs when the rf frequency is equal to the Larmor frequency in the center of the trap. The fit is done using a Gaussian function (red curve). The lower panel shows the residuals plot.

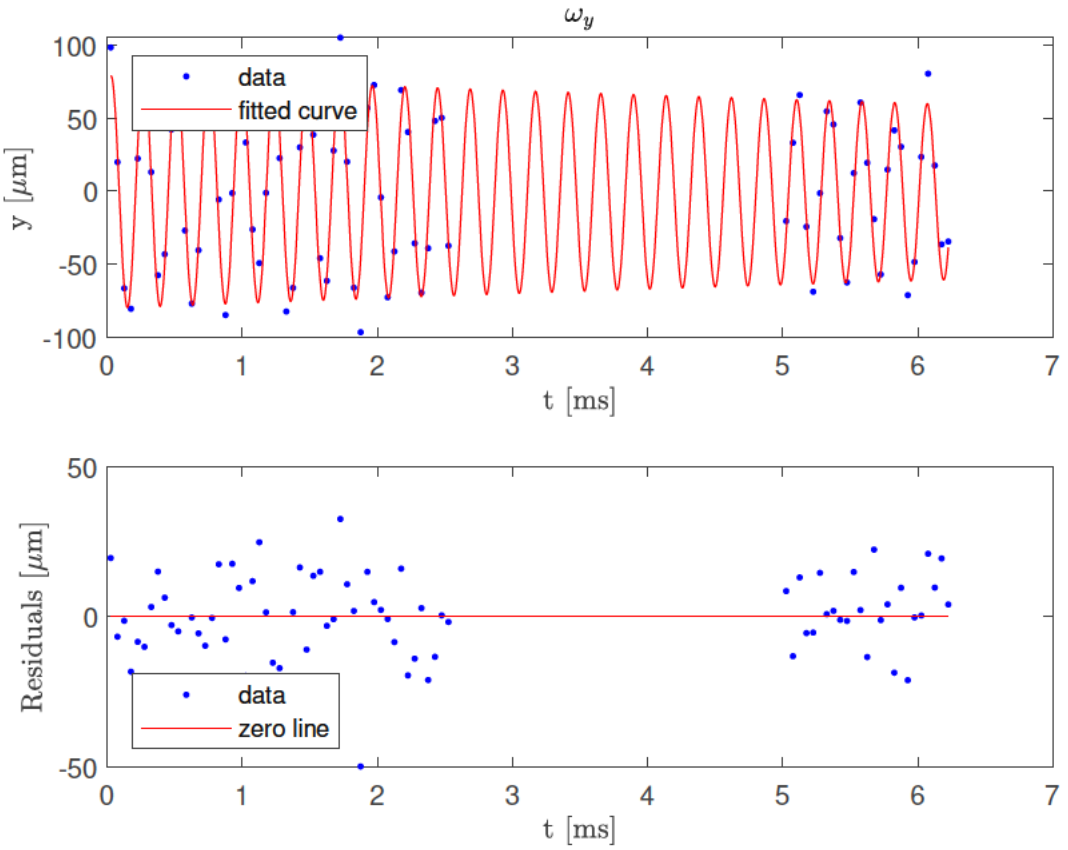

Figure 4.3: Trap frequency in transverse horizontal y direction (upper panel), obtained by exciting dipolar oscillations (sloshing) and measuring the position of the center-of-mass after expansion. The fit is done using a damped since function (red curve). The lower panel shows the residuals plot.

Table 4.1: Static (no dressing) trap calibration. Upper part: measured trap parameters, with the corresponding experimental uncertainty. Lower part: Parameters used in the chip trap simulations.

Measured parameters	
Trap bottom V_{TB}/h	824 ± 1 kHz
horizontal transverse trap freq. $\omega_y/2\pi$	4.14 ± 0.01 kHz
Settings used for simulations	
Current in main trapping wire	1 A
Current in long. confinement wires I_h	0.5 A
Bias field B_b	34.1 G
Ioffe field B_0	1.07 G
Max. rf current (each wire) I_0^{max}	80.25 mA
rf frequency	770 kHz
rf relative phase ϕ_{12}	0

4.2.2 State inversion

The experiment presented in this thesis aims at exciting a non-classical (Fock) state of the transverse confinement potential, in particular the second excited state of the transverse vibrational manifold of the final double-well potential, defined as *source state*. However, in a quantum harmonic oscillator, all states that can be addressed by a deformation of the potential are quasi-classical coherent states [67]. This statement also holds for a harmonically trapped interacting many-body system, where a quasi-classical collective oscillation at the trap frequency fully decouples from more complex internal dynamics. Hence, to transfer the condensate population into an internal excited state necessitates an anharmonic potential along the displacement direction y, where the decoupling of collective and internal dynamics breaks down. Furthermore, to be robust against excitation in the perpendicular direction z, anisotropy in the transverse plane of the potential is required, causing a detuning of trap levels between the directions [56].
We start off with a quasi-BEC formed in a harmonic trap, following a well-established sequence that we summarized in Section 3.2. Once the BEC is formed, the confining trap is dressed with a constant radiofrequency field (Section 3.3) with the goal of introducing anharmonicity and anisotropy to the potential landscape. Next, the DTB sequence takes place. The most important task we want to achieve is to go from a single to a double waveguide geometry and, at the same time, transfer the atomic population to the second vibrational state of the final double-well potential. As already shown in previous works [59, 63], in our setup, we can achieve a symmetric splitting of a single-well potential simply by increasing the amplitude of the rf dressing. The new challenge during this thesis work was to combine well-known rf dressing tools with state-of-the-art optimal control techniques that helped find the best amplitude ramp for the rf field that would achieve the transfer of the main BEC to the source state. We will explain the main idea behind the initialization process in the following.
The excitation of the condensate is based on symmetry considerations. The target wavefunction (second excited state) is symmetric with respect to the center of the double-well, and so is also the initial wavefunction (ground state of a single well). It is then possible to connect the two by a symmetric excitation that consists of a con-

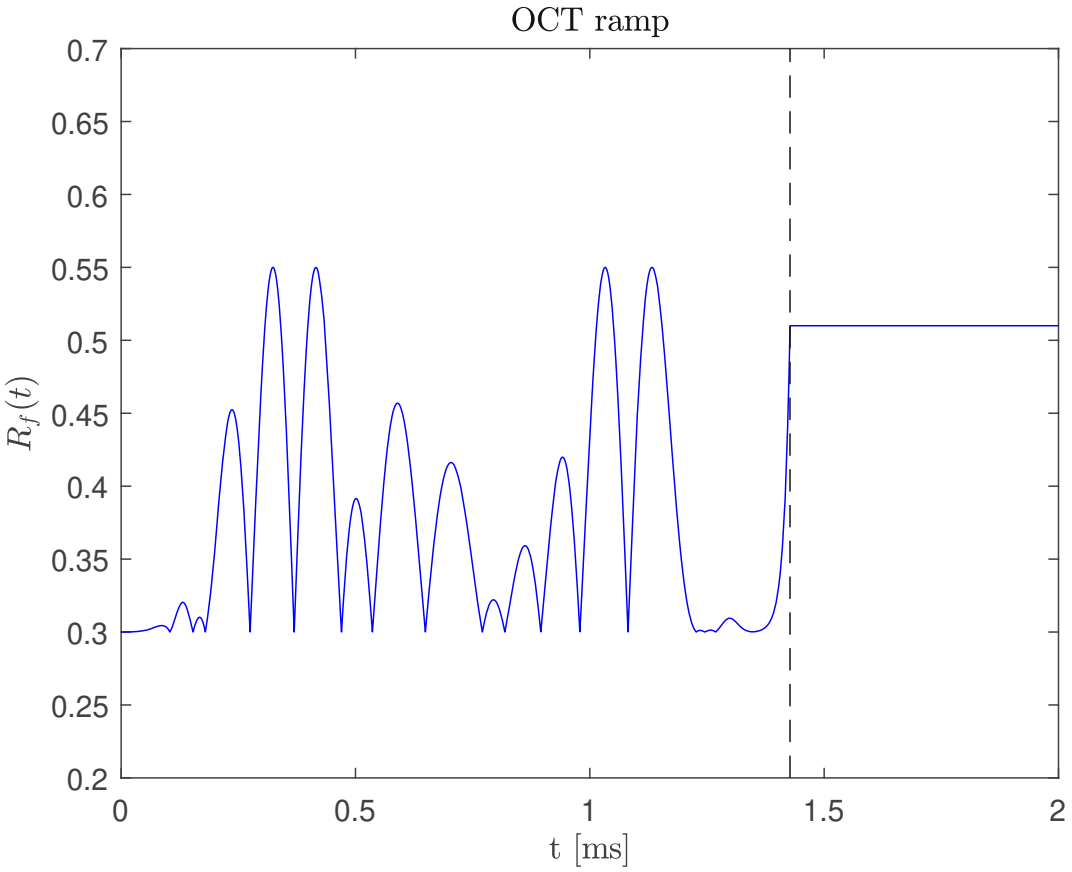

Figure 4.4: The ramp $R_f(t)$ of the amplitude of the radiofrequency field against time. The dashed black line points at the end of the initialization stage. The trap can then be switched off and the atoms imaged, or an in-trap holding time can be added. In this case, the value of the rf amplitude parameter $R_f(t)$ is kept at the final OCT ramp value of 0.51.

tinuous formation and deformation of a potential barrier at the center of the dressed single well. In particular, the method used to compute the trajectory of the barrier height versus time to perform the given task is based on a collaboration with the group of Tommaso Calarco and their initial publication on this matter [68]. We provided them with the parameters defining our harmonic confinement (see also Table 4.1) and asked them to provide us back with an amplitude ramp for the rf field necessary to achieve our goal. In Fig. 4.4 we plot the ramp of the rf dressing $R_f(t)$ versus time as a result of the optimization routine. As already mentioned, at the start of the initialization routine, the potential waveguide is only slightly dressed ($R_f = 0.3$), i.e., the trapping potential is still in a single-well configuration. At the same time, at the end of it, the atoms are trapped in a final double-well configuration, which is kept constant until the switch-off of the trap. Overall, the optimal control-based ramp or the initialization of the condensate lasts 1.4 ms.
In the following, we will report the main considerations used to compute the ramp in Fig. 4.4.

The OCT ramp

The system consists of a one-dimensional quasi-condensate, i.e., a weakly interacting bosonic ensemble that is loosely confined longitudinally but tightly confined transversally, as in previously realized optimal control experiments with atom chips [69, 70]. In the transverse direction that hereafter we denote as the y-axis, the potential is initially a single (anharmonic) well, as in Refs. [69,70], but then it is controlled dynamically using an external radiofrequency field to transform it into a double-well potential. We describe the system dynamics along the y-axis through an effective one-dimensional Gross-Pitaevskii equation, whose nonlinear Hamiltonian is given by:

$$\hat{H}_{\rm gp}[\psi,t] = -\frac{\hbar^2}{2m}\frac{\partial^2}{\partial y^2} + V(y,t) + gN|\psi(y,t)|^2. \tag{4.7}$$

Here, m is the mass of the boson, specifically of the alkali atom ^{87}Rb, $V(y,t)$ is the time-dependent potential that we manipulate optimally, g is the effective one-dimensional boson-boson coupling constant (see Ref. [70] for further details), N is the number of bosons, and $\psi(y,t)$ is the condensate wavefunction normalized to unity. We note that because of the significant separation of time scales between the transverse and longitudinal degrees of freedom, the quantum dynamics of the latter can be effectively assumed to be frozen during the excitation process in the transverse direction.
The external potential $V(y,t)$ produced by the atom chip is approximated by:

$$\begin{aligned} V(y,t) &= a_0(t) + a_2(t)y^2 + a_4(t)y^4 + a_6(t)y^6, \\ a_n(t) &= \sum_{j=1}^{6} \alpha_j^{(n)} [R_f(t)]^j \text{ for } n = 0,2,4,6, \end{aligned} \tag{4.8}$$

where the time-independent parameters $\alpha_j^{(n)}$, which are provided Table 4.2, have units of kHz/m^n.
The numerical values of the parameters $\alpha_j^{(n)}$ have been obtained by numerically fitting the simulated and experimentally calibrated potential generated by the atom chip with a polynomial of sixth order. This strategy has been adopted to simplify the numerical effort of the optimization. The dimensionless time-dependent function $R_f(t)$ is proportional to the strength of the radiofrequency field applied to the atom chip, and it is the control parameter we optimize on. In particular, we fix the maximum rf current to $I_{max} = 0.825$ A, and we define the parameter R_f as:

$$I_{RF}(t) = R_f(t) \times I_{max}, \tag{4.9}$$

where $I_{RF}(t)$ is the rf current running through the rf wires.
In the present experiment, the quasi-condensate is initially prepared in the ground state, $\varphi_0(y)$, of the initial single well potential $V(y,0)$. Our goal is to bring the quasi-condensate to the second excited state, $\varphi_2(y)$, of the external potential $V(y,t_f)$ in a double-well configuration a time t_f shorter than the decoherence time of the system. Here, the nonlinear eigenstates $\varphi_{0,2}(y)$ of the Hamiltonian in Eq. (4.7) are determined numerically by the imaginary-time technique with $N = 700$. To this end, we employ optimal control techniques to generate the optimal radiofrequency field $R_f(t)$ that minimizes the cost function defined at the final time t_f as:

$$\mathcal{J} = 1 - \left| \int_{\mathbb{R}} dy\, \varphi_2^*(y)\psi(y,t_f) \right|^2. \tag{4.10}$$

Table 4.2: The parameters $\alpha_j^{(n)}$ in units of kHz/μm^n for $n = 0, 2, 4, 6$.

j	$\alpha_j^{(0)}$	$\alpha_j^{(2)}$	$\alpha_j^{(4)}$	$\alpha_j^{(6)}$
0	54.451	74.025	-3.4221	0.2406
1	-8.6264	-19.429	24.648	-6.0581
2	3570.3	- 3309.1	1231.6	-153.85
3	-12650	18497	-8450.8	1221.2
4	25646	-46369	23425	-3661.4
5	-27546	56311	-30416	5049.5
6	12106	-26894	15268	-2663.3

Specifically, we employ the CRAB optimization method [66], and expand the radiofrequency field parameter $R_f(t)$ into a (not necessarily orthogonal) truncated basis:

$$R_f(t) = 0.3 + \frac{1}{\lambda(t) N_f} \left| \sum_{j=1}^{N_f} \left[c_j \cos\left(\frac{2\pi f_j t}{t_f}\right) + d_j \sin\left(\frac{2\pi f_j t}{t_f}\right) \right] \right| + 0.21\, e^{-8(t_f - t)}, \tag{4.11}$$

for $0 \leq t \leq t_f$. Here $N_f = 10$ denotes the total number of frequencies considered in Eq. (4.11); the multiple frequencies allow us to engineer non-trivial pulses with multiple maxima and minima, as shown in Fig. 4.4. The dimensionless function:

$$\lambda(t) = 0.5 + 10^4 \left[e^{-8t} + e^{-8(t_f - t)} \right] \tag{4.12}$$

is large and positive at $t = 0$, t_f, thereby fixing the initial and final values of the rf field. On the other hand, $\lambda(t)$ assumes the value 0.5 at intermediate times, so as to allow for variations of the rf field within the interval $(0, t_f)$. Furthermore, owing to experimental constraints, we impose the condition $0.3 \leq R_f(t) \leq 0.55\ \forall t$. We note that the field Eq. (4.11) is already given in dimensionless units, where times are rescaled with respect to $1/\omega_0$. The optimisation is carried out by varying the parameters c_j, d_j and f_j. Thus, the optimisation has been performed in such a way that the double-well potential $V(y, t_f)$ is obtained by setting $R_f(t_f) = 0.51$ at final time $t_f/\omega_0 = 1.4$ ms, while $R_f(0) = 0.3$ results in the initial single-well potential. The exponential function appearing in Eq. (4.11) and its width $1/8$ have been chosen such that it increases smoothly and monotonically to the numerical value 0.21 as $t \to t_f^-$, such that the control parameter reaches the target value $R_f(t_f) = 0.51$ and we avoid excitation of the condensate along the vertical z axis. In Fig. 4.4 the optimised curve of the parameter $R_f(t)$ is plotted against time. The values of $R_f(t)$ for $t < 0$ and $t > t_f = 1.4$ ms in Fig. 4.4 signify that $R_f(t)$ is time-dependent only for the intermediate optimization times $(0, t_f)$, while it assumes constant values outside this time-interval.

4.2.3 Detection: position and momentum measurements

After state inversion, thanks to the OCT ramp (Section 4.2.2), the main BEC is capable of emitting twin atoms in double waveguide confinement (DTB atoms). The DTB population grows with increasing holding time in the trap. We are interested in the low-pair emission regime and consider a small depletion of the source state (see Ref. [56]), so we usually directly switch off the trap at this moment of the sequence, right after the OCT ramp has finished. However, depending on the final analysis, an extra step may be necessary before the trap is switched off. We have the possibility of choosing the measurement basis to be either in position or momentum. In practice, since we observe the atomic profiles after a long time of flight, we always measure in momentum space (far-field limit). However, suppose we imprint a large transverse momentum to the left and right wavepackets right before the trap is switched off. We can separate the two wavepackets, hence performing a left and right position measurement.
In our setup, we imprint a large momentum kick to the atoms with a very fast increase of the barrier height separating the two waveguides[1]. Such a rapid increase of the barrier height results in an extra transverse acceleration that allows the left and right-well wavepackets to acquire a large transverse momentum and separate from each other after time of flight. This allows to define four distinct zones on the final picture and count the atoms in the four single-particle states separately (see Fig. 4.5.a). The goal of the *separation procedure* is to project the DTB emission into the four single-particle states $|L_-\rangle, |L_+\rangle, |R_-\rangle, |R_+\rangle$ in order to be able to measure number squeezing among any two of them (see Sections 4.5 and 5.3.1). This analysis will help us confirm the result in Eq. (4.14).
Instead, if we were to simply switch off the final trap and detect the twin beams after time of flight, we would not see four different outputs but only two since a long time of flight makes the initial position difference negligible compared to the expansion of each wavepacket (see Section 3.4.2). The *interference procedure* aims at detecting two-particle interference effects, as expected by the state expressed in Eq. (4.14). We employ a sequence where the initially separated left and right wavepackets expand and overlap.
The tight confinement along the horizontal transverse direction of the final double-well potential allows the left and right wavepackets to overlap in time-of-flight (see Fig. 4.5.b) To extract useful information from the images obtained with the interference procedure, we need to correlate the transverse profiles at different longitudinal momenta with each other and then take the average, i.e., compute the $G^{(2)}(k_y, k'_y)$ function. If we were to consider the averages directly of each transverse profile, we would only expect Gaussian profiles with no information on the coherence of the state [18].

4.3 The predicted final state

The outcome of the DTB procedure outlined in the previous Section 4.2 depends on the final double-well geometry and on the in-trap holding time after the source state initialization has happened. A crucial parameter to decide which type of state we expect is the tunneling coupling strength parameter J [57, 72, 73]. In the following, we will consider two cases: firstly, in Section 4.3.1 we will consider the situation of a decoupled double-well and almost zero in-trap holding time. Secondly, in Sec-

[1] The rf amplitude is increased from 0.51 (final double-well potential) to 0.81 in 0.025 ms

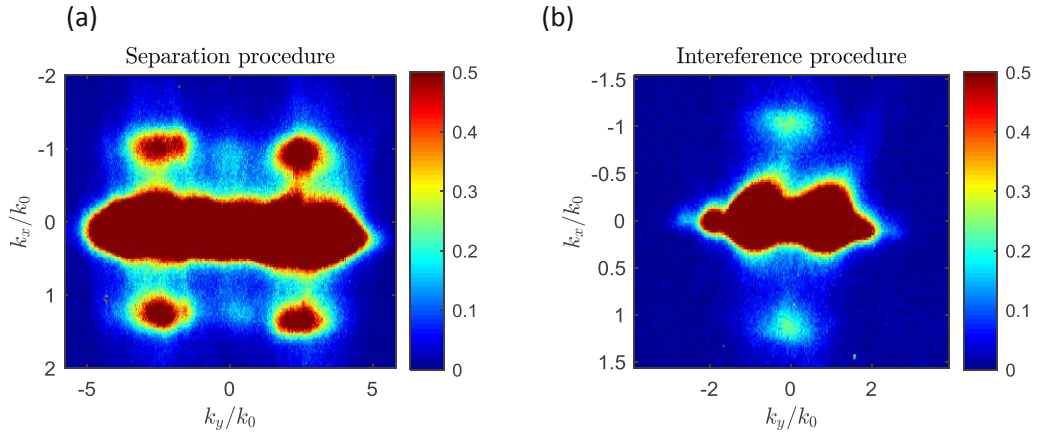

Figure 4.5: DTB emission in different measurement conditions (a) *Separation scheme*: experimental fluorescence image averaged over 825 experimental runs obtained with the separation procedure. Each run involves 2000-2200 total atoms, in average 150 of which are DTB atoms (75 pairs). The central cloud corresponds to the source state, while the emitted DTB atoms are found at $\pm k_0$. (b) *Intereference scheme*: experimental fluorescence image averaged over 1498 experimental runs obtained with the interference procedure. Each run involves 500-1100 total atoms, in average 20-50 of which are DTB atoms (10-25 pairs). The central cloud corresponds to the source state, while the emitted DTB atoms are found at $\pm k_0$. The three m_F states that were separated using a Stern-Gerlach experiment have been superimposed to the $m_F = 0$ state to help visualization.

tion 4.3.2, we will allow some tunneling dynamics between the two wells for some time before we switch off the trap and measure.

4.3.1 Zero-tunneling

The twin pair is created by s-wave scattering (δ-function interaction) between two bosonic atoms in the source state and emitted along the symmetric double waveguide with negligible overlap between the ϕ_L and ϕ_R wavefunctions relative to the transverse $|L\rangle$ and $|R\rangle$ states. In Fig. 4.6 we approximated the double-well potential by two harmonic potentials centered in $\pm x_0$ [72]. The coupling strength J governs the probability of tunneling of one particle between the two modes, which is given by [57,72]:

$$J = -\int \mathrm{d}\vec{r}\left(-\frac{\hbar^2}{2m}\nabla\phi_L\nabla\phi_R + \phi_L V\phi_R\right). \tag{4.13}$$

For $J \approx 0$, the state of the atom pair is expected to be in the maximally entangled state:

$$|\Psi_{DTB}\rangle_{(J=0)} = \frac{1}{\sqrt{2}}(|L\rangle_1|L\rangle_2 + |R\rangle_1|R\rangle_2) = \frac{1}{\sqrt{2}}(|LL\rangle + |RR\rangle), \tag{4.14}$$

where $|i\rangle_1|i\rangle_2 \equiv |i\rangle_{-k_0} \otimes |i\rangle_{+k_0}$ and $i = \{L, R\}$, and where we also adopted the notation $|LL\rangle \equiv |L\rangle_1|L\rangle_2$.
In order to explain why we expect such a state as the final outcome of our experimental procedure, let us consider a wave function

$$\Psi(\vec{r}_1, \vec{r}_2) \equiv \Psi(x_1, y_1, z_1; x_2, y_2, z_2) \tag{4.15}$$

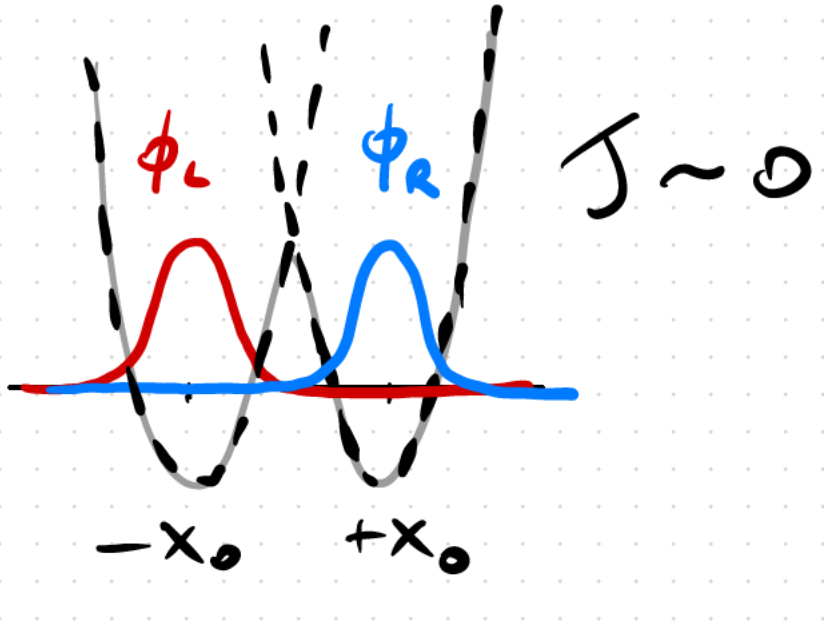

Figure 4.6: No tunneling. For large enough dressing amplitudes, the double-well potential can be approximated by two harmonic potentials, which yields analytical expressions for the tunneling term J (see text). Adapted from [57].

of two spin-polarized bosonic atoms 1 and 2. The wavefunction in Eq. (4.15) is symmetric with respect to the permutation of the coordinates (x_1, y_1, z_1) and (x_2, y_2, z_2) of the two atoms. Let us now factorize it into the longitudinal ($\parallel$) and transverse ($\perp$) parts

$$\Psi(x_1, y_1, z_1; x_2, y_2, z_2) = \Psi_{\parallel}(x_1; x_2)\Psi_{\perp}(y_1, z_1; y_2, z_2). \tag{4.16}$$

We readily see that each component of the factorized wavefunction of Eq. (4.16) must be symmetric with respect to the permutation of its coordinates, $\Psi_{\parallel}(x_1; x_2) = \Psi_{\parallel}(x_2; x_1)$ and $\Psi_{\perp}(y_1, z_1; y_2, z_2) = \Psi_{\perp}(y_2, z_2; y_1, z_1)$, in order for the total wavefunction to be non-zero at $\vec{r}_1 = \vec{r}_2$. This last property (being non-zero at $\vec{r}_1 = \vec{r}_2$) is fundamental to allow for s-wave scattering on the two-atom contact interaction pseudo-potential $\propto \delta(x_1 - x_2)\delta(y_1 - y_2)\delta(z_1 - z_2)$, where δ is the Dirac delta-function.
We can write the initial state of the two particles in the spatial basis as

$$\Psi_{in}(x_1, y_1, z_1; x_2, y_2, z_2) = \langle y_1, z_1|2\rangle\langle y_2, z_2|2\rangle\langle x_1|k_x = 0\rangle\langle x_2|k_x = 0\rangle, \tag{4.17}$$

where $\left|n_y\right\rangle = |2\rangle$ represents the transverse second-excited state and we assumed that longitudinally only the $|k_x = 0\rangle$ mode is initially populated (the source state is at rest longitudinally).
The emission process conserves the symmetry of the initial two-particle wavefunction. However, the $\delta(x_1 - x_2)$ term precludes transitions into anti-symmetric longitudinal states. Therefore, only the longitudinal state $(\langle x_1| - k_0\rangle\langle x_2|k_0\rangle + \langle x_2| - k_0\rangle\langle x_1|k_0\rangle)/\sqrt{2}$ is possible. For the transverse component of the final wavefunction, let us consider the $\{|L\rangle, |R\rangle\}$ basis. Due to bosonic symmetry, the transverse state is also symmetric with respect to the exchange of transverse coordinates. However,

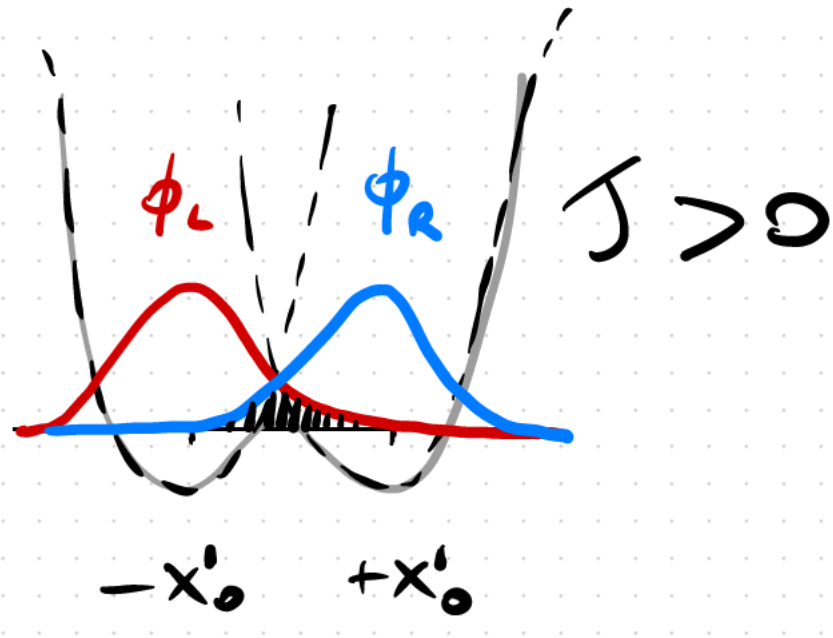

Figure 4.7: Non-negligible tunneling between the two wells.

transitions to $|LR\rangle$ or $|RL\rangle$ are not possible, since:

$$\begin{aligned}\int dy_1 \int dy_2 \int dz_1 \int dz_2 \langle 2|y_1,z_1\rangle\langle 2|y_2,z_2\rangle \delta(y_1-y_2)\delta(z_1-z_2) \\ \times \frac{\langle y_1,z_1|L\rangle\langle y_2,z_2|R\rangle + \langle y_1,z_1|R\rangle\langle y_2,z_2|L\rangle}{\sqrt{2}} \\ = \sqrt{2}\int dy \int dz (\langle 2|y,z\rangle)^2 \langle y,z|L\rangle\langle y,z|R\rangle = 0\end{aligned} \tag{4.18}$$

due to negligible overlap between the states $|L\rangle$ and $|R\rangle$.
The remaining symmetric transverse states are $|\Psi^-\rangle_\perp = (|LL\rangle - |RR\rangle)/\sqrt{2}$ and $|\Psi^+\rangle_\perp = (|LL\rangle + |RR\rangle)/\sqrt{2}$. For a perfectly symmetric trap:

$$\int dy \int dz \langle 2|y,z\rangle^2 \langle y,z|L\rangle^2 = \int dy \int dz \langle 2|y,z\rangle^2 \langle y,z|R\rangle^2, \tag{4.19}$$

hence the matrix element for a transition from $|2\rangle|2\rangle$ to $|\Psi^-\rangle_\perp$ vanishes due to destructive interference. The only non-zero matrix element couples $|2\rangle|2\rangle$ to $|\Psi^+\rangle_\perp$. Taking into account also the longitudinal component $(e^{-ik(x_1-x_2)} + e^{-ik(x_2-x_1)})/\sqrt{2}$, we recover the DTB state $|\Psi_{DTB}\rangle_{(J=0)} = |\Psi^+\rangle_\perp = (|LL\rangle + |RR\rangle)/\sqrt{2}$.

4.3.2 Non-zero tunneling

Let us now suppose that there is some residual (small) non-zero tunneling between the two wells ($J > 0$, see Fig. 4.7). The more general expression for the double twin-atom beam wavefunction is given by:

$$\begin{aligned}|\Psi_{DTB}\rangle \propto \Big[\mathcal{A}(p_{20})M_+ + \mathcal{A}(p_{21})M_-\Big]\Big(|LL\rangle + |RR\rangle\Big) + \\ + \Big[\mathcal{A}(p_{20})M_+ - \mathcal{A}(p_{21})M_-\Big]\Big(|LR\rangle + |RL\rangle\Big),\end{aligned} \tag{4.20}$$

where $p_{20} = \sqrt{(\hbar k)^2 - m\hbar\omega_{20}}$ and $p_{21} = \sqrt{(\hbar k)^2 - m\hbar\omega_{21}}$ are the momenta relative to the two lower-energy states 0 and 1, while $M_\pm = \int \mathrm{d}y \int \mathrm{d}z \, \langle 2|y, z\rangle^2 \Big[\langle y, z|L\rangle^2 + \langle y, z|R\rangle^2 \pm 2 \langle y, z|L\rangle \langle y, z|R\rangle \Big]$.
Also $\mathcal{A}(p_{20}) = \exp\left(-\frac{1}{2}\lambda_T^2 l_J^{-2}\right)\mathcal{A}(p_{21})$, where we introduced the tunneling length $l_J = 1/\sqrt{4mJ}$ and such that $2J = \hbar(\omega_{20} - \omega_{21})$.
Let us first see how we can recover Eq. (4.14) in the limit of zero tunneling $J \to 0$. If $J \simeq 0$, then $M_+ = M_-$ and they can be factored out in Eq. (4.20). Furthermore, the two lowest vibrational states 0 and 1 are degenerate compared to the 2 state and $\omega_{20} = \omega_{21}$ holds true. This means that also $\mathcal{A}(p_{20}) = \mathcal{A}(p_{21})$ holds and the second line of Eq. (4.20) vanishes, thus recovering the expression for the predicted final state discussed in Eq. (4.14).
The switching on of a particular tunneling coupling strength between the two wells has two effects: firstly, it increases the overlap between the left and right well wavefunctions $\phi_{L,R}$ (see also Fig. 4.7). In doing so, since the coefficients $M_{+,-}$ depend on the amount of overlap, these acquire different values and cannot be factored out. Secondly, the vibrational level structure of the double-well potential gets slightly modified, and in particular, the lowest energy levels 0 and 1 become less and less degenerate. In this case, we need to look at Eq. (4.20) to get an insight into how the DTB state can be modified by the turning on of a tunneling process between the two wells. In particular, we do expect an admixture of the states $|LR\rangle, |RL\rangle$ as an outcome. On the other hand, J should not be too large. Otherwise, the lowest energy levels become spectroscopically resolved, and the interference is lost. In Section 6.3 we will see a modified *interference procedure* where we slowly ramp down the final double-well barrier height to slightly increase the tunneling before we switch off the trap and image the atoms.

4.3.3 Extension to a fermionic system

In our present experiment, the source state from which the atom pairs are emitted relies on a Bose-Einstein condensate with a defined longitudinal momentum $k_x = 0$. Moreover, the emitted double twin-atom beams are created by an s-wave scattering process. The same procedure does not apply to a fermionic gas. The atoms in a fermionic source state would have many longitudinal momenta up to the Fermi momentum k_F; hence the total momentum of the emitted atom pairs would not be well defined. Moreover, spin-polarized fermions do not experience s-wave scattering. Thus the collisional process at the basis of the emission of twin beams would be completely different. So a source of fermionic twin atoms would have to look completely different. One can imagine breaking up a bosonic diatomic Feschbach molecule into its fermionic components, as suggested in [74], but imprinting a significant momentum on them would require additional processes like transferring the molecule before the break-up into a higher excited quasi bound state. We could then envision a system that produces twin fermionic atoms in a single waveguide. The spin degree of freedom would replace the double waveguide transverse degree of freedom of our setup and the emitted state would be a maximally entangled spin state $|\Phi^-\rangle = (|\downarrow\rangle_- |\uparrow\rangle_+ - |\uparrow\rangle_- |\downarrow\rangle_+)/\sqrt{2}$.

4.4 Methods

In this Section, we will describe the methods used to treat the experimental raw pictures in Sections 4.4.1 and 4.4.2, and then we outline number-squeezing techniques in Section 4.5.
As for imaging processing, we treat the raw images derived from the Andor camera (.sif) using background level subtraction and etaloning artifacts correction. All the image processing is performed with Matlab-based custom programs written over the years on the Rb2 experiment.
The initial part consists of deriving the correct parameters that allow converting the secondary electron signal from the initial pictures into primary electrons, which can then be converted into the fluorescence photons emitted by the atoms using the multiplicative factor m (photons-per-atom parameter). These initially processed images constitute the starting for further processing considered in the following paragraphs and will be referred to as *raw images*, even if some processing (namely the conversion from secondary to primary electrons) has already taken place[2]. In the following, we describe:

- the typical background and etaloning correction procedure, in Section 4.4.1
- the filtering process, in Section 4.4.2
- how to derive number-squeezing parameters, in Section 4.5

4.4.1 Background and etaloning correction

The raw images containing the fluorescence signal can be further processed. In particular, when observing in a log plot the averaged raw picture (see Fig. 4.8), obtained by many realizations of the same experiment, one can notice two main effects: a gradient-like background level and an etaloning effect. In Fig. 4.9.a, we display a typical gradient-based background subtracting map. This map is obtained for each single shot realization and is derived by fitting the image's contour where no atoms are present. In Fig. 4.9.b, we display the etaloning map used to correct the experimental pictures. This map is derived by normalizing the pattern obtained by the average over many realizations of a very dilute atomic cloud. The normalization is done by imposing that the sum on the signal over the whole matrix is equal to the number of pixels. In this way, dividing any matrix by the etaloning map does not modify the overall mean values but only the relative intensities (signal variance).
These are well-known effects that have been already discussed in detail on previous works dealing with the same imaging system.
The usual image treatment consists of subtracting the gradient-like background and then divide by the etaloning map in Fig. 4.9.b. The etaloning effect is due to the read-out electronics of the camera chip that imprints a wavy pattern on the original signal (it acts as an unwanted Fabry-Perot element).
In Fig. 4.10, we compare the averaged image over 1497 realizations of a typical experiment. Here, the meaning of the experiment is not relevant. Instead, we are interested in the variance and the mean value of the corrected signal on each matrix. The upper row displays the 2-dimensional experimental pictures averaged over the same

[2]The conversion is performed using the information provided by additional images taken with light off. Fitting the histograms of these other pictures allows reconstructing the fluorescence signal [56].

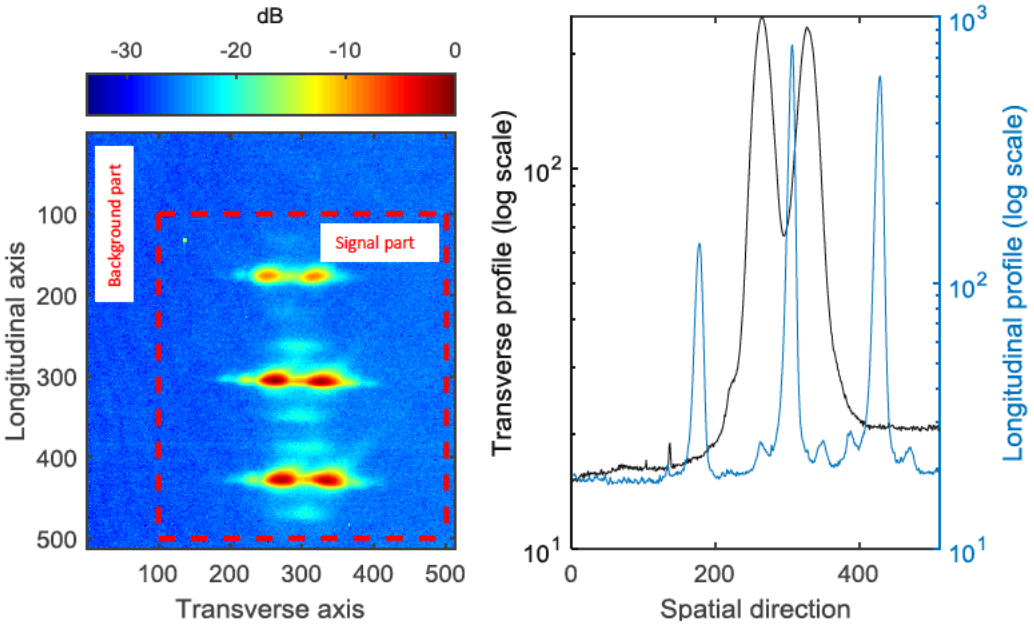

Figure 4.8: On the left part, the averaged raw picture is displayed. Two main zones can be distinguished: a background part, where no atoms are present, and a signal part, where the atoms are. We use the background part to estimate the residual background level and compute the correction map. The image is plotted on a logarithmic scale and normalized by the intensity of the brightest pixel (dB). On the right side, the profiles along the spatial directions of the left image allow identifying the gradient-like residual background level along the transverse direction (black curve) and an almost uniform background level along the plot's vertical axis (longitudinal direction, light blue curve). Barely noticeable on the left picture are etaloning artifacts, characterized by a wavy footprint on the original signal.

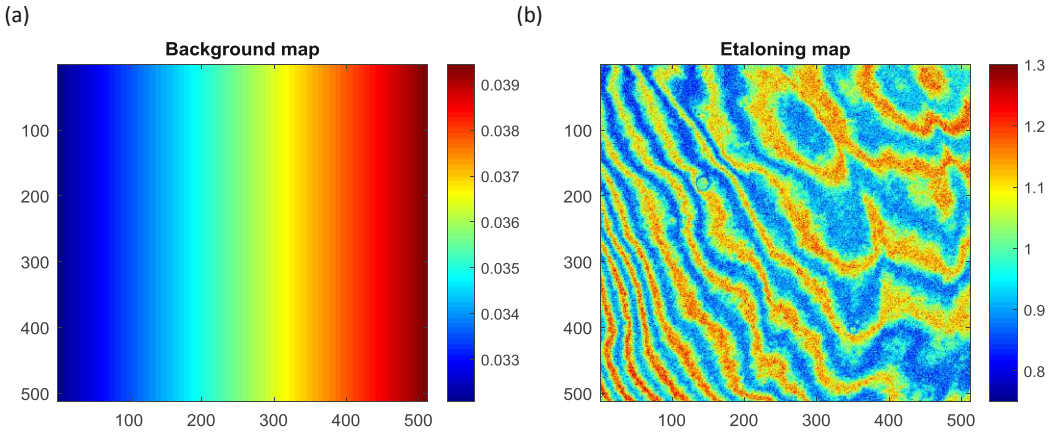

Figure 4.9: (a) First correction map: background correction. This map is used to eliminate the residual background plateau from each experimental raw picture. It is obtained by fitting a linear regression curve to the mean values of the frame of the picture containing no atoms (see the background part in Fig. 4.8). Since there is no significant difference along the plot's vertical direction, we are left with a gradient-like one-dimensional correction along the plot's horizontal axis. The background level correcting map is applied by simple subtraction to the raw image. (b) Second correction matrix: etaloning map. This map is used to attenuate the etaloning artifacts produced by the structure of the read-out electronics in the back-illuminated CCD camera. It is obtained by averaging over many realizations of a dilute atomic cloud that act as a uniform illumination medium for the CCD camera. The residual Gaussian signal profile is subtracted, and the resulting signal is normalized. We divide the background-treated image by the etaloning map.

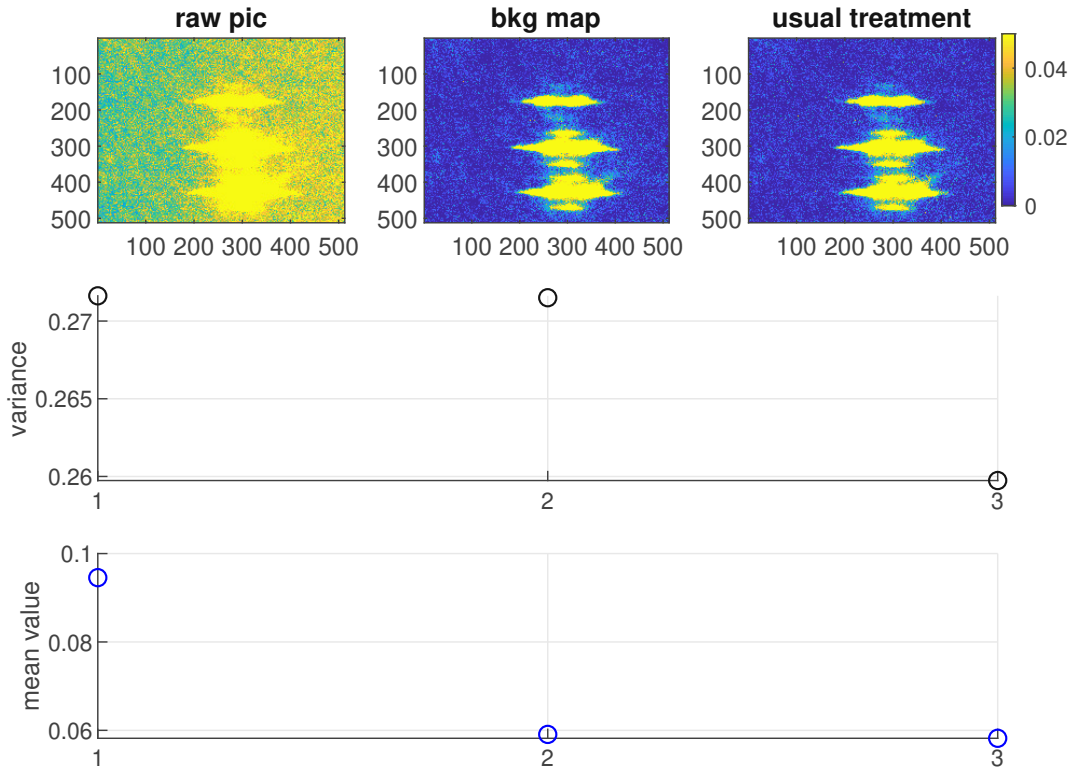

Figure 4.10: Comparison of different image processing methods. From left to right: no treatment, background treatment alone, background and etaloning treatment. On the upper row, the averaged images are displayed. The most striking difference is visible in the color change from the raw to the corrected pictures due to the background subtraction. The same effect can be visualized when plotting the mean value of the signal as a function of the image processing method (last row at the bottom). The etaloning effects can be drastically reduced by dividing the image from the background treatment by the etaloning map in the last column (usual treatment method), as it is clear by looking at the variance plot as a function of the different methods (central row).

number of realizations, where each column correspond to the different image correction methods here taken into consideration. The second row displays the signal variance of the averaged picture obtained with each method. The last row displays the corresponding mean values. Considering the different image processing methods here, the first column (from left to right) refers to the raw signal without any correction. The second column, in the center, refers to the raw signal to which a gradient-like background has been subtracted. The last column, to the right, corresponds to the usual treatment mentioned above: we first apply the gradient-like background subtraction using the matrix in Fig. 4.9.a, and *then* we correct for etaloning effects using the etaloning map in Fig. 4.9.b. As one can see from the 2-dimensional images in the first row and the lowest plot at the bottom, the mean value of the second matrix is drastically reduced compared to the first one, as expected from an image processing method aiming at getting rid of the gradient-like background plateau. We see the effect of the etaloning map of Fig. 4.9.b onto the variance of the signal, the lowest value of which is reached with the usual treatment method using the etaloning map. We can also assume we do not know whether it is better to apply the etaloning map *after* the background subtraction (as in the usual treatment) or *before* the background treatment. Also, it might be interesting to see what happens when, instead of *dividing* each background-treated image by the etaloning map, we instead *multiply* the result by the etaloning map. These different possibilities can be compared with the usual treatment in Fig. 4.11. The plot is conceived similarly to Fig. 4.10, but here we compare the averaged picture obtained from background+etaloning corrected pictures (first column to the left), and the etaloning+background corrected pictures (second column in the center), where the etaloning map is applied *before* the background-subtraction step, and the background+etaloning-as-product (last column to the right), where the etaloning map is *multiplied* instead of *divided*. As we can see from the signal variance plot (second row to the center) and from the mean value plot (last row at the bottom), the etaloning must be applied as a division since when used as multiplication, we obtain larger mean and variance values. Moreover, when comparing the first two methods, already from the 2-dimensional images displayed in the first row on top, it is clear that the etaloning-first method leaves a residual wavy pattern. Moreover, even if the variance is only slightly lower for the usual treatment than the etaloning-first method, the first method does not allow properly subtracting the background level, as it is clear by looking at the corresponding higher mean background level.

In summary, we have seen that the best method to correct for residual background effects and etaloning artifacts is to *first* correct for the background effect using the subtraction map in Fig. 4.9.a, and *then* divide the result by the etaloning map in Fig. 4.9.b.

In the following, the results presented will follow from the analysis of pictures that have been processed using this procedure. Nevertheless, the qualitative results (the presence of a fringe pattern in the $G^{(2)}(k_1, k_2)$ correlation function, for example) do not depend on the correction method used, and they can be obtained using the raw images. This excludes the possibility of emerging the results only from imaging processing-dependent effects.

4.4.2 Filtering and cut-off

Other image processing methods that have been considered in this thesis work and have been used to a certain extent to produce some results of Chapter 5 are the filtering and the cut-off methods.

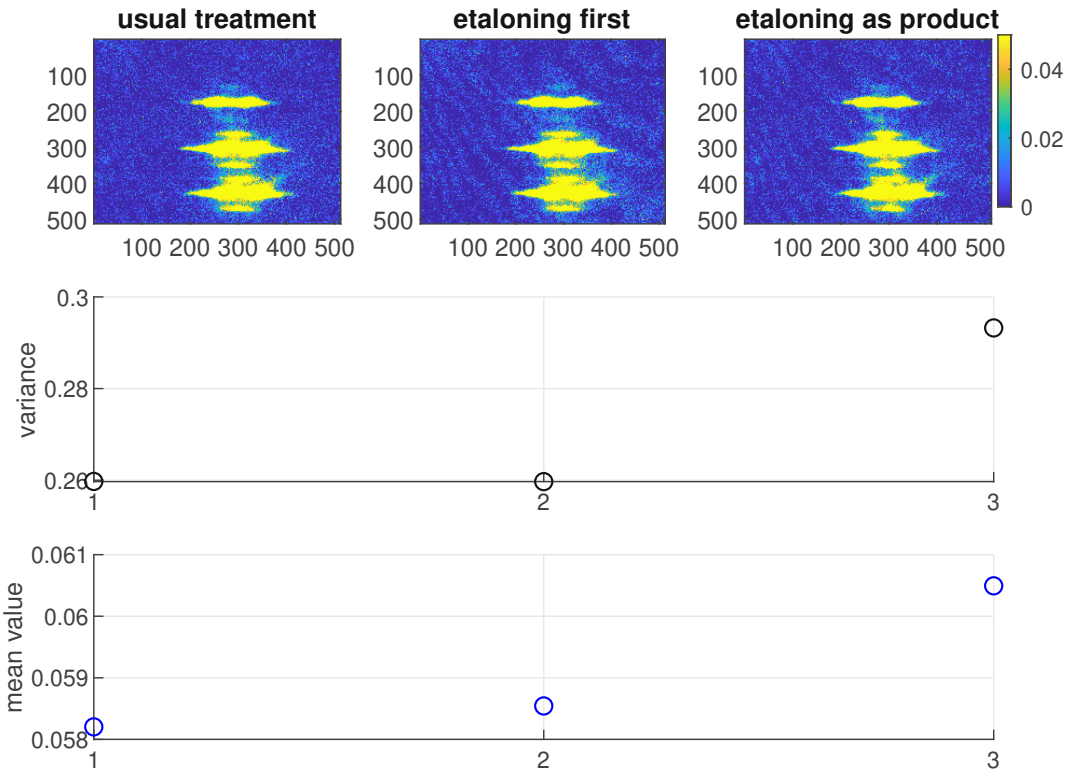

Figure 4.11: Comparison of different image processing methods. From left to right: usual treatment, etaloning first, etaloning as a product. On the upper row, the averaged images are displayed. The most striking difference is visible in the residual etaloning artifacts present in both the last two methods as compared to the usual treatment in the first column. The same effect can be visualized when looking at the variance plot as a function of the different methods (central row). The first method must also be excluded because of the higher mean background value (see the last plot at the bottom).

Filtering The filtering method takes as an input matrix $A(p,q)$ the experimental image treated with the usual treatment explained in Section 4.4.1. It then computes the 2-dimensional discrete convolution $C(j,k) = conv2(A,B)$ operation given by

$$C(j,k) = \sum_p \sum_q A(p,q)B(j-p+1, k-q+1) \tag{4.21}$$

of the input matrix $A(p,q)$ with a 2-dimensional normalized Gaussian envelope, which is given by

$$B(l,m) = \frac{1}{\sqrt{2\pi}\sigma} e^{-\frac{l^2+m^2}{2\sigma^2}}, \tag{4.22}$$

where we set $\sigma = 1$ pxl, and where p and q run over the full image area 512x512 pxl^2. Usually, the signal from an atom will occupy more than one pixel, on average, a 3x3 sub-matrix of nearby pixels [56]; hence, the filtering process smears out the intensity over a larger amount of pixels. It is then convenient to set an intensity threshold to eliminate the signal originating from isolated pixels (mainly noise) from atoms.

Cut-off The cut-off method takes the filtered pictures as input, and it consists of defining an intensity threshold t and then setting all the pixels with intensities lower than t equal to zero intensity. The threshold is chosen by looking at the DTB signal and the background level, as defined in Fig. 4.8 for example. We want to eliminate those pixels whose intensity comes from residual read-out artifacts or camera noise and not significantly diminish or erase atomic signals. It is nevertheless quite arbitrary to define it, and its choice can be justified by looking at the histogram of the leftover signal and noise pixels. In Fig. 4.12, we display the result of filtering alone and filtering followed by a cut-off image processing method, shown with histograms reporting the frequency of a certain pixel intensity event over 100 realizations of the same experiment yielding each time a 512x512 pxl^2 fluorescence intensity matrix, as a function of the image processing method used to treat the images. In this example, we have arbitrarily set the width of the filtering envelope function to $\sigma_{filter} = 1$ pxl, and the cut-off threshold $t_{cut-off} = 0.5$ counts/pxl.

4.5 Number-squeezing parameter

Let us consider a source of atoms that emits N_1 atoms with momentum k_1 and N_2 atoms with opposite momentum $k_2 = -k_1$. Let us also assume a constant total atom number $N_+ = N_1 + N_2$. The atoms could be emitted randomly in the two possible momentum modes or originate from a twin-atom source. Suppose we want to certify that the atoms are coming from a twin-atom source and are always emitted in pairs characterized by opposite momenta. We employ a statistical analysis. Let us suppose that, at the end of an experimental cycle we got N_1 atoms characterized by the momentum k_1 and N_2 atoms with momentum k_2. We then repeat the experiment several times and collect many copies $i = 1 \dots N$ of the variable signal difference N_-^i, where $N_-^i = N_1^i - N_2^i$ for each experimental realization i and we look at the histogram of its distribution[3]. If the atom source generates atoms with opposite momenta that fall *at random* in one of the two outputs with equal probability, the distribution of the signal difference is a *normal* or binomial distribution, centered around the value zero and characterized by a variance $\sigma_b^2 N_- = N_+$. Tossing a fair coin is a possible example of an experiment where the output is either head or tail

[3]In the following, we will drop the index i, but sill consider the variables as statistical quantities, where the mean and the standard deviation have a meaning as referred to the many realizations.

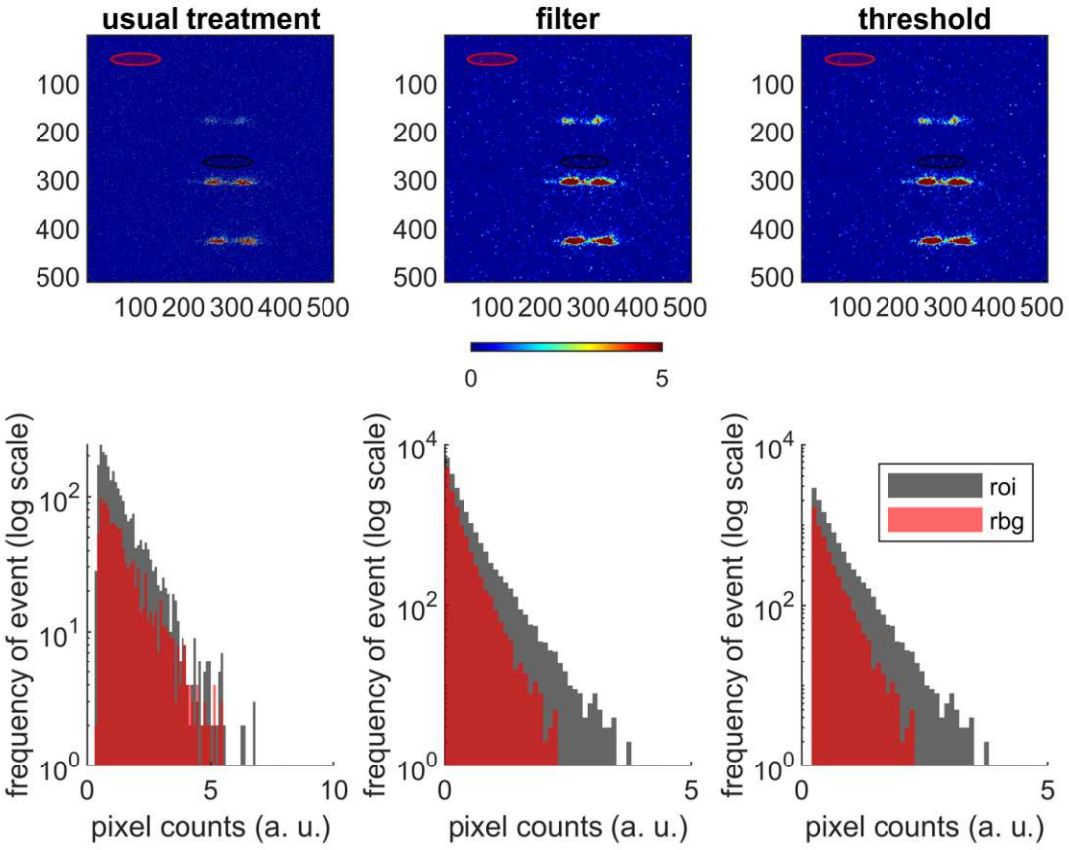

Figure 4.12: Comparison of different image processing methods. From left to right: usual treatment, filtering method, cut-off method. On the upper row, the single-shot images as a function of the method used to compute them are displayed. We identify two region-of-interest (ROI) ellipses: the red one is the ROI corresponding to the background level or rbg; the black one is the ROI of the atomic signal corresponding to one of the two momenta of the DTB atoms or simply ROI. On the lower row, we display the histograms of the pixel intensities within the regions of interest, red for rbg and dark gray for ROI. The histograms are in log scale on the vertical axis. We display a single shot image on the first row, but we have used 100 images corresponding to the same experiment to produce the histograms at the bottom. The filter method uses $\sigma = 1$ pxl. The cut-off method applies an intensity threshold $t = 0.5$ counts/pxl.

with equal probability. On the other hand, if the source is a twin-atom source, then the atom number difference is expected to be characterized by a narrower distribution centered around the value $N_- = 0$, since we here deal with the generation of pairs of atoms, where $N_1 = N_2$ exactly. In this case, we talk about atom number squeezing since the distribution of N_- is *squeezed* with respect to the corresponding binomial distribution having the same total atom number N_+. It is helpful to define a number squeezing parameter ξ^2 as the ratio between the observed variance of the twin pairs and the correspondent binomial variance

$$\tilde{\xi}^2 = \frac{\sigma^2 N_-}{\sigma_b^2 N_-}. \tag{4.23}$$

Experimentally we cannot access the atom number directly, but we measure the number of photons hitting the camera instead. Having considered two boxes 1 and 2 on a typical fluorescence image, we define the sum and difference photon signal relative to the two boxes $S_\pm = S_1 - S_2$, where S_1 (S_2) is the measured fluorescence signal from box 1 (2). If we assume that to each imaged atom correspond exactly m photons, then we can write

$$S_\pm = mN_\pm, \tag{4.24}$$

where $N_\pm$ is the sum or difference atom number relative to the same two boxes. Having assumed m constant, we can derive an expression for the variance of the signal difference $\sigma^2 S_- \equiv \mathrm{var}(mN_-) = m^2\sigma^2 N_-$. Using Eq. (4.24) and the expression $\sigma_b^2 N_- = N_+$ we get

$$\tilde{\xi}^2 \equiv \frac{\sigma^2 N_-}{\sigma_b^2 N_-} \equiv \frac{m^2}{m^2} \cdot \frac{\sigma^2 N_-}{N_+} = \frac{\sigma^2 S_-}{mS_+}. \tag{4.25}$$

To evaluate the average number of photons m scattered by each atom, we compare fluorescence images to absorption images for increasingly larger atomic clouds [75]. From this comparison, we derived $m = 29.4$ for the separation data and $m = 20.7$ for the interference data, meaning each atom generates clusters of around 20-30 photons when crossing the light sheet.

We come now to the discussion on detection noise [56]. The final number of counts created by each photon hitting the camera is a random variable whose statistics are governed by photonic shot noise. On top of the usual shot noise level, there is an additional noise generated by the amplification stage at the electron-multiplication register of the camera. To account for it, the variance due to shot noise gets doubled [76]: $\sigma_{sn}^2 S_- = 2S_+$. A second contribution comes from the background signal $\hat{b}$, which is important when regions with a low signal are considered. Since the background signal is indistinguishable from the actual signal coming from the atomic fluorescence, the same considerations made above apply and $\sigma_{sn}^2 b_- = 2b_+$. We define the total noise contribution to the variance $\sigma_n^2 S_- = \sigma_{sn}^2 S_- + \sigma_{sn}^2 b_-$ and modify the expression for the uncorrected number squeezing to take into account the total noise as

$$\xi^2 = \frac{\sigma^2 S_- - \sigma_n^2 S_-}{\sigma_b^2 S_-}. \tag{4.26}$$

We can then define the minimum value of atom number squeezing ξ_n^2 between the momentum states detectable in our system as

$$\xi_n^2 = \frac{\sigma_n^2 S_-}{\sigma_b^2 S_-} = \frac{2S_+ + 2b_+}{mS_+} \simeq 2/m, \quad \text{for } b_+ \ll S_+. \tag{4.27}$$

Typical values are $\xi_n^2 \simeq 0.07$ (separation data) and $\xi_n^2 \simeq 0.097$ (interference data). The difference can be explained by the different photon-per-atom values p for the two different data sets.
To compute the error on the squeezing parameter ξ^2 and ξ_n^2, we propagate the errors of the quantities that appear in the expressions Eqs. (4.25) and (4.26). We also consider an error on the order of 10% in the determination of the exact photons-per-atom parameter m.

4.5.1 Simulation of emitted DTB pairs

Let us know simulate the emission of double twin-atom pairs in a straightforward scenario. Each emitted atom pair is a twin pair; hence it must have exactly one atom with momentum $-k_0$ labeled as 1 and exactly one atom with momentum k_0 labeled as 2. In this scenario, there are only four possible outcomes of twin pairs in a double-well: $|L_1, L_2\rangle$, $|L_1, R_2\rangle$, $|R_1, L_2\rangle$, $|R_1, R_2\rangle$. In general, the final state is then made of a mixture of those states or, more interestingly, of a coherent superposition (see also Section 4.3).
The populations $\hat{p}_{LL}$, $\hat{p}_{LR}$, $\hat{p}_{RL}$, $\hat{p}_{RR}$[4] corresponding to each of the above mentioned pairs are statistical distributions centered around a mean value $p = \langle \hat{p} \rangle$ and with shot-noise fluctuations (the variance of $\hat{p}$ is equal to its mean value). We assume that we generate N_p total pairs (DTB atoms are $N_a = 2N_p$).
We also assume a population parameter F_i for each of the four pair outcomes $|LL\rangle$, $|LR\rangle$, $|RL\rangle$, $|RR\rangle$ given by:

$$\begin{aligned} F_{LL} &= \cos^2\theta, \\ F_{LR} &= \sin^2\theta, \\ F_{RL} &= \sin^2\theta, \\ F_{RR} &= \cos^2\theta, \end{aligned} \tag{4.28}$$

where $\theta \in [0, \pi/2]$ is a parameter that modifies the population distributions, $\theta = 0$ being the situation where we only emit pairs in the $|LL\rangle$ and $|RR\rangle$ modes, $\theta = \pi/2$ corresponding to the opposite scenario where we only emit $|LR\rangle$ and $|RL\rangle$ pairs. In the case of $\theta = 0$, we do not distinguish whether the emission is coherent as in Eq. (4.14), or totally mixed: both these scenarios will produce a balanced emission of $|LL\rangle$ and $|RR\rangle$ pairs. Similarly, for the other values of θ.
So, the mean and the variance of each pair population is given by

$$\langle \hat{p}_i \rangle = N_p \cdot F_i, \tag{4.29}$$

$$\mathrm{var}(\hat{p}_i) = \langle \hat{p}_i \rangle, \tag{4.30}$$

where $i = \{LL, LR, RL, RR\}$ runs on the four possible outcomes, and where the variance equals the mean value since we assumed shot-noise dominated statistics. Assuming a photon-per-atom parameter $m = 20$ (see Section 3.4.2), the populations $\hat{p}$ in each single-particle mode $|L_1\rangle, |L_2\rangle, |R_1\rangle, |R_2\rangle$ in fluorescence signal can be computed from the pairs with the formulas

$$\begin{aligned} \hat{p}_{L1} &= m \cdot (\hat{p}_{LL} + \hat{p}_{LR}), \\ \hat{p}_{L2} &= m \cdot (\hat{p}_{LL} + \hat{p}_{RL}), \\ \hat{p}_{R1} &= m \cdot (\hat{p}_{RL} + \hat{p}_{RR}), \\ \hat{p}_{R2} &= m \cdot (\hat{p}_{LR} + \hat{p}_{RR}). \end{aligned}$$

[4] We dropped the indices 1,2 since we adopted the notation that the first (second) letter always corresponds to the momentum labeled 1 (2).

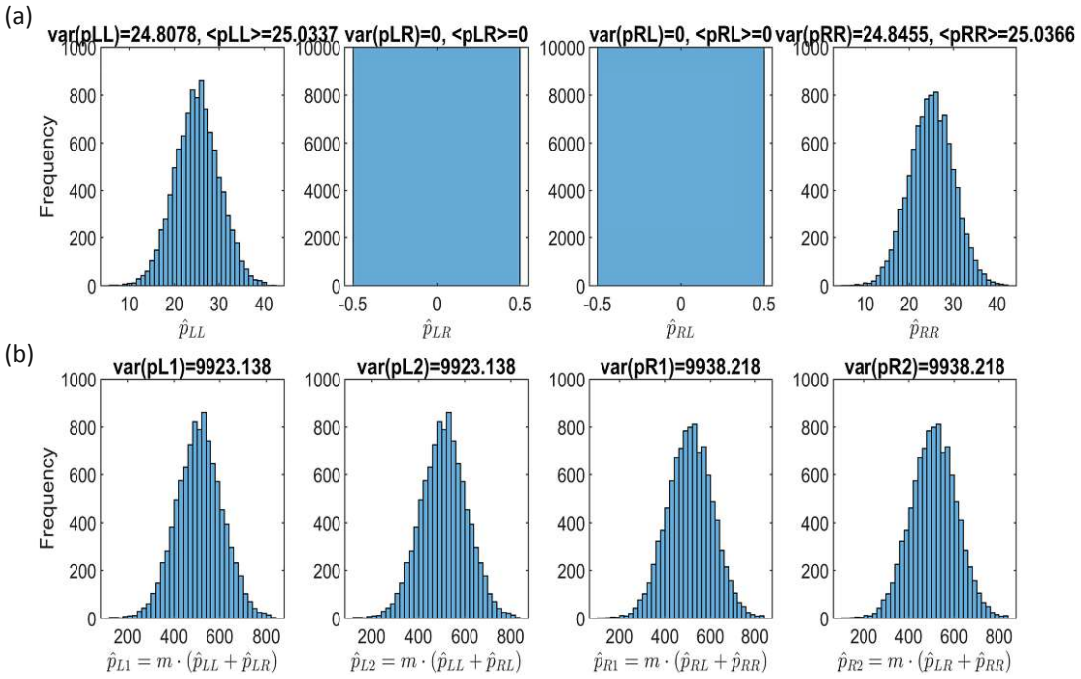

Figure 4.13: Simulation of the emission. (a) Histograms of the pairs of atoms $\hat{p}_i$ emitted in the four emission channels $i = \{LL, LR, RL, RR\}$, assuming a normal distribution dominated by shot-noise fluctuations. We here assume that only LL and RR pairs can be generated (no pairs present in the LR and RL histograms). On top, we reported the calculated mean values and the variances. (b) Histograms of the single-particle populations $\hat{p}_j$ for $j = \{L1, L2, R1, R2\}$. The single-particle population represents the distribution of the number of atoms present in that single-mode channel. To make these histograms we assumed $N_p = 50$, $N_s = 10$k and $m = 20$.

We then let the simulation run for $N_s = 10000$ times and record the distributions of the pair populations. In Fig. 4.13.a we show the histograms of the pair populations (as number of pairs produced), and in Fig. 4.13.b the single-particle mode populations (as fluorescence signal). To make these histograms we assumed $N_p = 50$ total pairs emitted, shot-noise fluctuations of the number of pairs in each channel, the population angle $\theta = 0$ (no pairs emitted in the LR or RL channel), the photon-per-atom parameter $m = 20$, and we acquired $N_s = 10000$ repetitions of the emission process.
Finally, we can compute different atom number-squeezing parameters Section 4.5

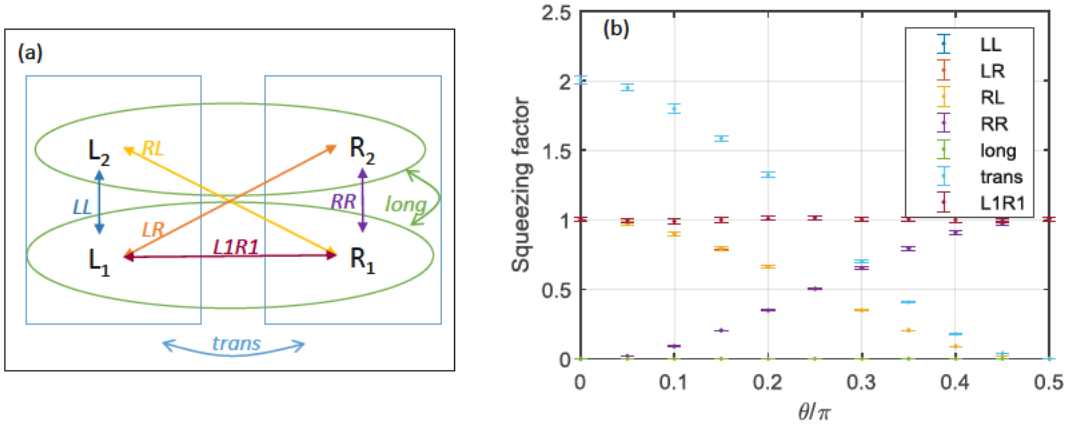

Figure 4.14: (a) Scheme of the two-by-two possible combinations of the signals from the four available single-particle emission channels L_1, L_2, R_1, R_2. (b) Number squeezing parameters calculated using Eq. (4.31) for different values of $\theta \in [0, \pi/2]$ (see Eq. (4.28)).

using the definitions given by:

$$
\begin{aligned}
\xi^2_{LL} &= \frac{\mathrm{var}(\hat{p}_{L_1} - \hat{p}_{L_2})}{m \cdot (\hat{p}_{L_1} + \hat{p}_{L_2})}, \\
\xi^2_{LR} &= \frac{\mathrm{var}(\hat{p}_{L_1} - \hat{p}_{R_2})}{m \cdot (\hat{p}_{L_1} + \hat{p}_{R_2})}, \\
\xi^2_{RL} &= \frac{\mathrm{var}(\hat{p}_{R_1} - \hat{p}_{L_2})}{m \cdot (\hat{p}_{R_1} + \hat{p}_{L_2})}, \\
\xi^2_{RR} &= \frac{\mathrm{var}(\hat{p}_{R_1} - \hat{p}_{R_2})}{m \cdot (\hat{p}_{R_1} + \hat{p}_{R_2})}, \\
\xi^2_{long} &= \frac{\mathrm{var}(\hat{p}_{L_1} + \hat{p}_{R_1} - \hat{p}_{L_2} - \hat{p}_{R_2})}{m \cdot (\hat{p}_{L_1} + \hat{p}_{L_2} + \hat{p}_{R_1} + \hat{p}_{R_2})}, \\
\xi^2_{trans} &= \frac{\mathrm{var}(\hat{p}_{L_1} + \hat{p}_{L_2} - \hat{p}_{R_1} - \hat{p}_{R_2})}{m \cdot (\hat{p}_{L_1} + \hat{p}_{L_2} + \hat{p}_{R_1} + \hat{p}_{R_2})}, \\
\xi^2_{L1R1} &= \frac{\mathrm{var}(\hat{p}_{L_1} - \hat{p}_{R_1})}{m \cdot (\hat{p}_{L_1} + \hat{p}_{R_1})}.
\end{aligned}
\tag{4.31}
$$

In Fig. 4.14.b we show the number-squeezing parameters of Eq. (4.31) as a function of the population angle θ. This plot shows how the squeezing parameter, when applied to the different two-by-two combinations of single-particle populations visualized in Fig. 4.14.a, can be used to distinguish among different emissions. In particular, in the situation where we only generate twin pairs in the even channels LL and RR as in Eq. (4.14), we expect $\xi^2_{LL} = \xi^2_{RR} = \xi^2_{long} = 0$, $\xi^2_{LR} = \xi^2_{RL} = \xi^2_{L1R1} = 1$, and $\xi^2_{trans} = 2$, while if $\theta = \pi/2$, hence we only emit pairs in the odd channels LR and RL, we expect $\xi^2_{LL} = \xi^2_{RR} = \xi^2_{L1R1} = 1$, $\xi^2_{LR} = \xi^2_{RL} = \xi^2_{long} = \xi^2_{trans} = 0$. Even if the squeezing parameter can give useful information related to the emission scenario we deal with, it cannot, in any case, distinguish between an entangled and a totally mixed state, as it only deals with the population terms of the density matrix of the state under investigation.

4.6 Atom-atom correlation analysis

As already pointed out in previous works [18], if we want to characterize a two-particle state we need to look at two-particle properties. In particular, let us look at the atom-atom correlator $G^{(2)}(\eta_1, \eta_2)$ given by:

$$G^{(2)}(\eta_1, \eta_2) = \langle \hat{\Psi}^\dagger(\eta_1)\hat{\Psi}^\dagger(\eta_2)\hat{\Psi}(\eta_1)\hat{\Psi}(\eta_2)\rangle = \mathrm{Tr}[\hat{\rho}\hat{\Psi}^\dagger(\eta_1)\hat{\Psi}^\dagger(\eta_2)\hat{\Psi}(\eta_1)\hat{\Psi}(\eta_2)], \quad (4.32)$$

where $\eta_1(\eta_2)$ is the coordinate of the first (second) atom (it will be the longitudinal momentum in our experiment), and where the n-th atomic field $\hat{\Psi}_n$ can be expressed in the left and right well basis representation $\{|L\rangle, |R\rangle\}$ as:

$$\hat{\Psi}(\eta_n) = \sum_{i=L,R} \Phi_i(\eta_n)\hat{a}_{ni} \quad (4.33)$$

with $\hat{a}_{ni}$ being the annihilation operator for the n-th atom in the mode $|i\rangle$ of wavefunction Φ_i.
It can be shown that the atom-atom correlator can be linked to the elements of the density matrix $\hat{\rho}$ of the two-particle state as:

$$G^{(2)}(\eta_1, \eta_2) = \sum_{i,j,k,l=L,R} \rho_{ijkl}\Phi_i(\eta_1)\Phi_j(\eta_2)\Phi_k^\star(\eta_1)\Phi_l^\star(\eta_2). \quad (4.34)$$

$G^{(2)}(\eta_1, \eta_2)$ is experimentally accessible by looking at the atomic density profiles along the transverse direction at the two longitudinal momenta 1 and 2:

$$G^{(2)}(\eta_1, \eta_2) = \langle n(\eta_1)n(\eta_2)\rangle. \quad (4.35)$$

In principle, by detecting the DTB atoms at different longitudinal momenta, we can gain information on the density matrix by looking at atom-atom density correlations. Practically, it is tough to gain helpful information with this method since it is required, for this analysis to work, to identify the partner of each atom in the twin pair. When we emit, on average, N pairs, it is impossible to know which atom is linked to only which atom thus, the contrast on the fringe patterns of the coherence terms of Eq. (4.39) will decrease automatically by a factor $\sqrt{N}$. Given these intrinsic difficulties, we will show that it was possible to acquire some information from this technique when applied to the momentum space.
If we now focus our attention on the momentum space, we can rewrite Eq. (4.34) as:

$$G^{(2)}(p_1, p_2) = \sum_{i,j,k,l=L,R} \rho_{ijkl}\phi_{ijkl}(p_1, p_2), \quad (4.36)$$

with $\phi_{ijkl}(p_1, p_2) = \Phi_i(p_1)\Phi_j(p_2)\Phi_k^\star(p_1)\Phi_l^\star(p_2)$. The momentum-space wavefunctions of the left $|L\rangle$ and right $|R\rangle$ states are given by:

$$\begin{aligned}\Phi_L(p) &= \mathrm{e}^{-iy_0p/\hbar}\mathcal{A}(p) = [\cos\left(y_0k_y\right) - i\sin\left(y_0k_y\right)]\mathcal{A}(p),\\ \Phi_R(p) &= \mathrm{e}^{iy_0p/\hbar}\mathcal{A}(p) = [\cos\left(y_0k_y\right) + i\sin\left(y_0k_y\right)]\mathcal{A}(p),\end{aligned} \quad (4.37)$$

where y_0 is half the inter-well spacing and k_y the wave number, while $\mathcal{A}(p)$ is the envelope that assures the wavefunctions $\Phi_{L,R}(p)$ are correctly normalized. In the case of a perfectly balanced double-well, the envelope is Gaussian and we get $\mathcal{A}(p) = \mathrm{e}^{-p^2/2\sigma_p^2}\sqrt{2/\sqrt{\pi}\sigma_p}$. We can now rewrite the $\phi_{ijkl}(p_1, p_2)$ wavefunctions in Eq. (4.36) using Eqq. (4.37) to get:

$$\phi_{ijkl}(p_1, p_2) = \mathcal{A}^2(p_1)\mathcal{A}^2(p_2)F_{ijkl}(p_1, p_2), \quad (4.38)$$

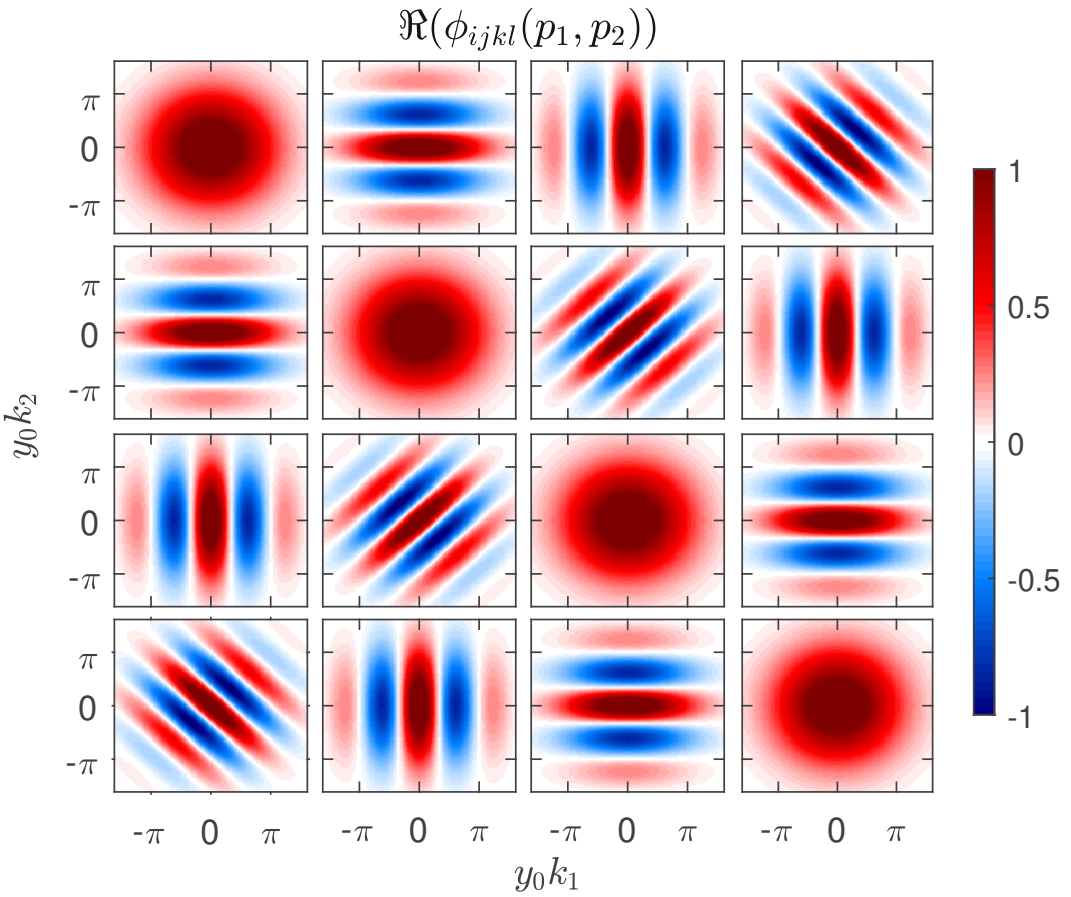

Figure 4.15: Real part of the $\phi_{ijkl}(p_1, p_2)$ functions in Eq. (4.38). The order of the plots follows the one for the F-functions in Eq. (4.39). To generate these plots we assumed the half inter well spacing to be $y_0 = 0.75\ \mu$m and the envelope $\mathcal{A}(p) = \mathrm{e}^{-p^2/2\sigma_p^2}\sqrt{2/\sqrt{\pi}\sigma_p}$, with $\sigma_p = 0.5\ \mu\mathrm{m}^{-1}$.

where $F_{ijkl}(p_1, p_2)$ is given by:

$F_{ijkl}(p_1, p_2)$	LL	LR	RL	RR
LL	1	$\mathrm{e}^{-2iy_0k_2}$	$\mathrm{e}^{-2iy_0k_1}$	$\mathrm{e}^{-2iy_0(k_1+k_2)}$
LR	$\mathrm{e}^{2iy_0k_2}$	1	$\mathrm{e}^{-2iy_0(k_1-k_2)}$	$\mathrm{e}^{-2iy_0k_1}$
RL	$\mathrm{e}^{2iy_0k_1}$	$\mathrm{e}^{2iy_0(k_1-k_2)}$	1	$\mathrm{e}^{-2iy_0k_2}$
RR	$\mathrm{e}^{2iy_0(k_1+k_2)}$	$\mathrm{e}^{2iy_0k_1}$	$\mathrm{e}^{2iy_0k_2}$	1

(4.39)

In Fig. 4.15 we plot the real part of the $\phi_{ijkl}(p_1, p_2)$ functions, assuming $y_0 = 0.75\ \mu$m and a Gaussian envelope with $\sigma_p = 0.5\ \mu\mathrm{m}^{-1}$. In general, if we do not know which state we are generating, all these terms can in principle contribute to the $G^{(2)}(p_1, p_2)$ function (see Eq. (4.36)). Along the main diagonal there are the terms known as *populations*: these terms show up when we emit only two-particle states as LL or RR states, or a mixture of the two. The other terms, known as *coherences*, show interesting fringe patterns. The coherences present oscillations along one momentum coordinate when they involve both the $|L\rangle$ and the $|R\rangle$ mode for the corresponding atom in the twin pair. Therefore, the diagonal ϕ_{LRRL} and anti-diagonal term ϕ_{LLRR}

contribute with diagonal and anti-diagonal fringes, respectively. These terms are unique: the diagonal (anti-diagonal) fringe can only come from the ϕ_{LRRL} (ϕ_{LLRR}) term. The other coherence terms present horizontal or vertical fringes, each term being identical to a second one: $\phi_{LLRL} = \phi_{LRRR}$ and $\phi_{LLLR} = \phi_{RLRR}$.
In the following, we will apply the atom-atom correlator of Eq. (4.35) to our final DTB state, with the goal of extracting helpful information on the underlying density matrix.

Chapter 5

Analysis of the experimental results

The first significant result of this thesis work is demonstrating the state inversion procedure with optimal control techniques. Employing an optimally computed ramp of the dressing rf field shone on the atoms, we were able to efficiently transfer almost all of the atomic population to the desired quantum state (Section 5.1).
The second main result of this work is the demonstration of the generation of twin atoms (atoms that are produced at the same time with opposite momenta) in a double waveguide confinement potential. In Section 5.2 we apply atom number squeezing analysis techniques and show that the twin character is well confirmed (independently of the detection procedure).
However, such a state shows more features than the reduced number of fluctuations corresponding to a twin source. The expected DTB outcome is a maximally entangled quantum superposition of the left and right localized states of the final double-well potential (Section 4.3). In order to characterize such a state, the last result of this thesis work is the realization of a double-slit experiment with only a few DTB pairs.

- Firstly in Section 5.3.1, we apply number-squeezing methods to characterize the emission type and distinguish between possible emission scenarios, as already discussed in Section 4.5.1.

- Secondly in Section 5.3.2, we apply atom-atom second-order correlation techniques and observe two-particle interference effects when the left and right components of the wavefunction are let overlap and interfere.

Such an experiment is the atomic version of the Ou, Mandel experiment using photons. The ideal case for such an experiment would be an even lower number of pairs N_{pair} produced for each experimental realization, ideally $N_{pair} \ll 1$ [20].
In Table 5.1 we summarize all the data sets that will be considered in the following sections.

5.1 Demonstration of the state inversion

We estimate the percentage of atoms transferred to the source state by looking at the evolution of the wave function of the BEC, after the excitation OCT pulse, in time of flight. Suppose the state initialization (see Section 4.2.2) has been successful, and

Table 5.1: Data sets used for the results presented in this thesis. R_p denotes the typical number of realizations with the same settings. m is the photon-per-atom parameter (when relevant).

Label	Date	Scan#	R_p	m	Used in	Description
CARP21	27/04/21	13	5	/	5.1	carpet
SEPAR19	03/09/19	2	798	29.4	5.2, 5.3.1	separation
INTER19	05/09/19	7	1497	20.7	5.2, 5.3.2	interference
INTER21	05/10/21	81	636	21	5.3.2	interference
evINTER21	19/10/21	20	120	27	6.2	time evolution
modINTER21	19/10/21	18	463	27	6.3	modified $G^{(2)}$ pattern

the BEC population has been successfully transferred to the second excited state of the final potential. In that case, the outcome is a constant profile. If more than one eigenstate of the potential is populated, we should observe a beating pattern in the momentum distribution varying with the holding time in the trap. We look at the BEC wavefunction as a function of time to gain information on the efficiency of the state inversion process.
We first simulate the initialization process by assuming a certain initial wavefunction and an initial trap configuration. The external potential produced by the atom chip is approximately given by:

$$\begin{aligned} V(y,t) &= a_0(t) + a_2(t)y^2 + a_4(t)y^4 + a_6(t)y^6, \\ a_n(t) &= \sum_{j=1}^{6} \alpha_j^{(n)} [R_f(t)]^j \text{ for } n = 0,2,4,6, \end{aligned} \tag{5.1}$$

where the time-independent parameters $\alpha_j^{(n)}$ are listed in Table 4.2 in units of kHz/m^n, and $R_f(t)$ is the computed OCT ramp (see Fig. 4.4). We then let the system evolve under the time-dependent GPE of Eq. (4.7). To compute the source state we diagonalize the Hamiltonian of the final potential $V(y,t_f)$. The quality of the transfer is estimated by measuring the overlap of the wavefunction resulting from the GPE propagation of the initial state $\psi(y,t)$ with the source-state wavefunction $\psi_{goal}(y)$. The infidelity parameter is defined as:

$$infidelity(t) = 1 - \int \mathrm{d}y \left| \psi^*_{goal}(y)\psi(y,t) \right|^2. \tag{5.2}$$

The result of such simulation is show in Fig. 5.1.
This procedure also allows us to predict the time evolution of the BEC density both in position and in momentum. In Fig. 5.2 we show the main BEC density time evolution during the OCT ramp and up to 0.5 ms after it, both in position space (upper panel) and in momentum space (lower panel). The ramp was specifically designed to transfer the largest number of atoms to the second excited state of the final double-well confinement (source state). If this goal is achieved, the BEC finds itself in an eigenstate of the Hamiltonian. Thus its evolution must be constant. While during the OCT ramp the BEC wavefunction is changing fast and continuously, after the amplitude ramp has been applied (roughly at 1.42 ms), the evolution of the BEC wavefunction follows a stable pattern (at the same time the infidelity goes to zero, see Fig. 5.1).

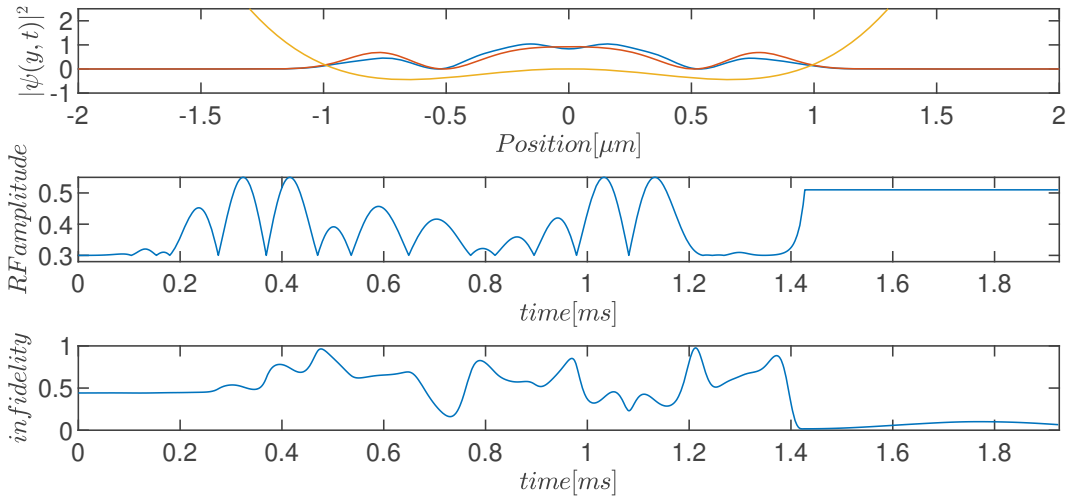

Figure 5.1: Simulation of the time evolution of the main BEC wavefunction (blue curve upper panel) under the influence of the external potential $V(y,t)$ (yellow line, upper panel), driven by the time-dependent OCT ramp parameter $R_f(t)$ (central panel). The infidelity (lower panel) is a measure of the discrepancy between the simulated evolution of the initial BEC wavefunction (blue curve, upper panel) and the target state (orange curve, upper panel). The upper panel photographs the situation at the last time value here shown ($\sim$ 1.9 ms). The ramp of the rf amplitude lasts $\sim$ 1.42 ms.

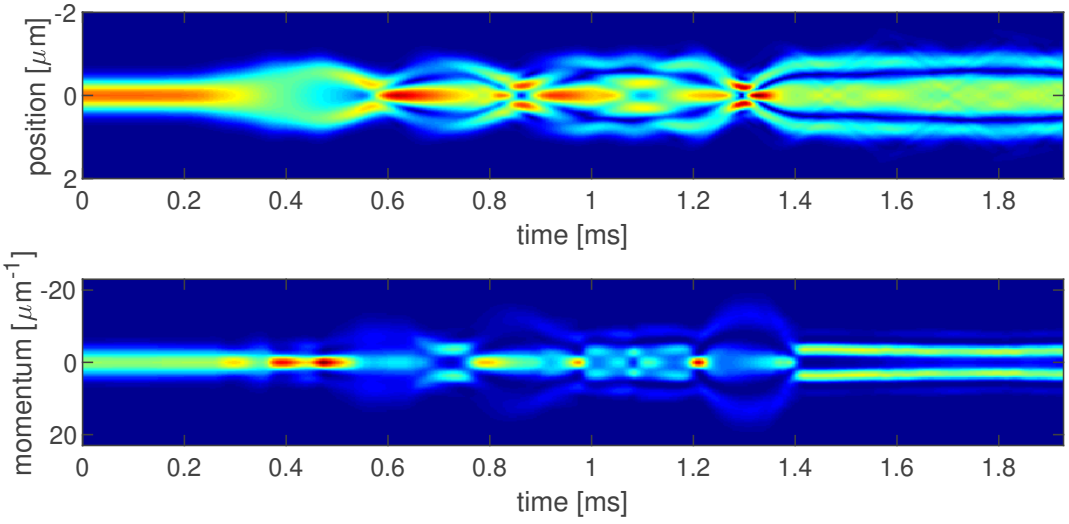

Figure 5.2: Simulation of the time evolution of the main BEC wavefunction during, and up to 0.5 ms after, the OCT ramp. The upper panel shows the evolution in position space. The lower panel, the evolution in momentum space (Fourier transform).

In the experiment, we record the BEC density profile at different times (during and after the OCT ramp has taken place). We then bring all these transverse profiles together in chronological order to reconstruct the time-evolution of the BEC wavefunction and define that as a "carpet". An experimental carpet is shown in Fig. 5.3 (lower panel), where it can be compared with the simulation of the BEC time-evolution in momentum space (upper panel). We need to convert the camera pixels of axis y in momentum space k_y. To do that, we first compute the time-of-flight expansion factor given by:

$$F_{tof} = \frac{\hbar}{m_{Rb87} \cdot t_{tof}} = 32.1530\ \mu m^2, \tag{5.3}$$

where m_{Rb87} is the mass of ^{87}Rb, and where $t_{tof} = 44$ ms. We can then derive the momentum axis as:

$$k_y = (y - y_0) \cdot p_s / F_{TOF}, \tag{5.4}$$

where we defined the center pixel y_0, and where the pixel size $p_s = 4\ \mu$m [56].
We then fit the experimental carpet with a linear combination $\Psi_{guess}(y)$ of different single-particle eigenstates $\psi_i(y)$ up to the sixth order ($i = 6$):

$$\Psi_{guess}(y) = p_2\psi_2(y) + \sum_i e^{i\phi_i}\sqrt{p_i}\psi_i(y) \tag{5.5}$$

where ϕ_i ($i = 0, 1, 4, 6$) are the relative phases and p_i ($i = 0, 1, 2, 4, 6$) are the normalized contributions from the five different states considered. The odd components from the third and fifth-order were excluded from the fit function based on symmetry arguments to reduce the number of free parameters. This is consistent with the transverse symmetry of the experimental data. The main contribution to the experimental profile comes from the second excited state of the double-well potential ($\sim$ 97%), corresponding to the source state. This demonstrates the state inversion using the optimal control engineered sequence.

5.2 Twin-character verification

As already done previously in a single-well [40], we want to apply number-squeezing techniques to the analysis of the twin-atom pairs generated this time with a different excitation ramp (the OCT ramp of Section 4.2.2) in a different confinement landscape (here we deal with a double-well).
We start off by considering two data sets, one related to the *separation procedure* (190903scan2) in Fig. 5.4.(a,c), and the second related to the *interference procedure* (190905scan7) in Fig. 5.4.(b,d). In the separation data set we considered $\approx$ 800 runs, each run with $\approx$ 2000 total atoms, on average 100 of which are DTB atoms (50 pairs); while in the interference procedure we considered $\approx$ 1500 runs, each run with $\approx$ 810 total atoms, on average 24 of which are DTB atoms ($\sim$ 12 pairs). As already mentioned in Section 4.2.3, these two data are obtained with two different detection schemes, as it shows from the averaged images in Fig. 5.4.(a,b).
In the separation procedure, we also project the final DTB state into its left and right well components, while this step is skipped for the interference procedure. Moreover, in the interference procedure, for reasons related to the $G^{(2)}$ analysis, we separated the three m_F states: the same pattern (BEC + DTB emission) is here repeated three times since we separated the three m_F states using a Stern-Gerlach experiment. The two longitudinal states are visible for each m_F component. Nevertheless, both scenarios deal with twin-atom pairs. Hence we can apply a similar twin-character

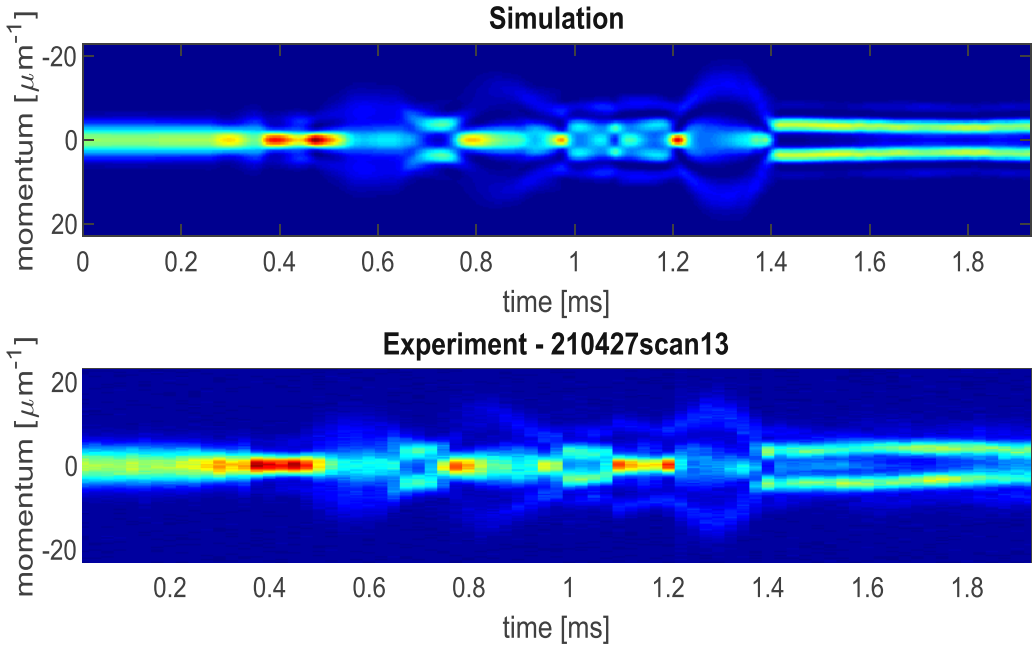

Figure 5.3: Comparison between the simulated time evolution of the BEC density profile in momentum space (upper panel), and the experimental density profile (lower panel). We assumed a pixel size of 4 μm and a time of flight of 44 ms.

revealing analysis to both data sets. In Fig. 5.4.(a) the central brightest signal corresponds to the main BEC. We single out the four single-particle states available for the DTB emission using rectangular boxes (in white) to count how many atoms fell in each single-particle state.
As already explained in previous works [40, 56], the non-classical correlation in the emitted twin-atom beams manifests itself as a sub-binomial distribution of the number imbalance $\hat{n} = \hat{N}_1 - \hat{N}_2$ between atoms detected at $\pm k_0$, where the hat symbol indicates a statistical quantity. The variance of $\hat{n}$ can be expressed as $\mathrm{var}(\hat{n}) = \xi^2 \langle \hat{N} \rangle = \xi^2 N$, where N is the expectation value of the total number $\hat{N} = \hat{N}_1 + \hat{N}_2$ of emitted twin atoms. The noise reduction factor ξ^2 quantifies the suppression of $\mathrm{var}(\hat{n})$ with respect to a binomial distribution, thus the amount of correlation between the populations $\hat{N}_1$ and $\hat{N}_2$ (see also Section 4.5). We do not measure atom numbers directly but fluorescence signals. The relation between the two quantities is given by:

$$\hat{S} = m\hat{N}, \tag{5.6}$$

where m is the photon-per-atom parameter introduce in Section 3.4.2. When dealing with the fluorescence signals $\hat{S}_{1,2} = m\hat{N}_{1,2}$, $\hat{s} \equiv \hat{S}_1 - \hat{S}_2$ and $\hat{S} \equiv \hat{S}_1 + \hat{S}_2$, also the photon-per-atom parameter m becomes relevant, as the definition of squeezing becomes:

$$\tilde{\xi}^2 = \frac{\mathrm{var}(\hat{s})}{m \cdot \langle \hat{S} \rangle} = \frac{\sigma^2 \hat{s}}{m \cdot S}. \tag{5.7}$$

To account for detection noise we introduced in Section 4.5 the noise-corrected squeezing parameter:

$$\xi^2 = \frac{\sigma^2 \hat{s} - \sigma_n^2 \hat{s}}{\sigma_b^2 \hat{s}}. \tag{5.8}$$

In order to confirm the twin character of the emission, we will consider the total

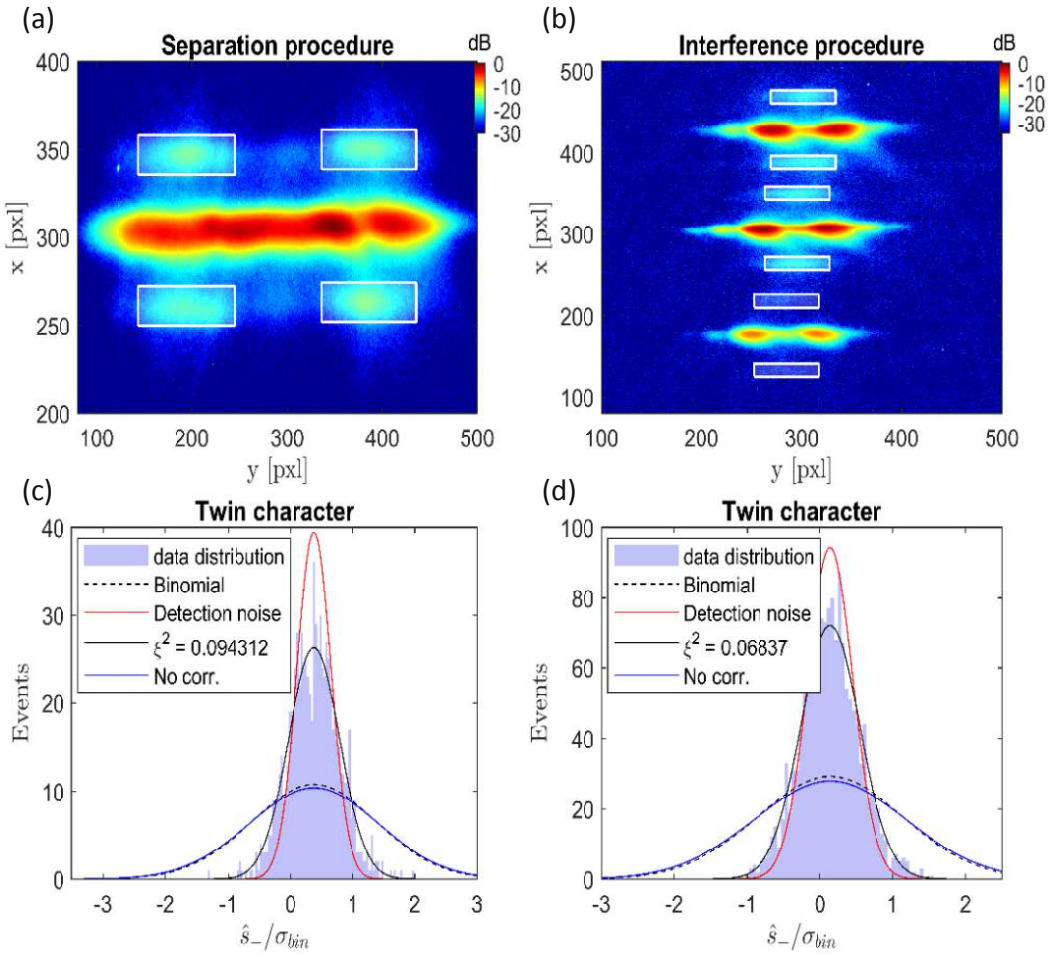

Figure 5.4: Twin character of the DTB emission (a) *Separation scheme*: averaged experimental image in decibel (dB) scale (referenced to the brightest pixel). White boxes define integration regions for counting DTB atoms. (b) *Intereference scheme*: averaged experimental image in dB scale. (c) Twin character histogram of the fluorescence signal difference $\hat{s}$ between the atoms that fell at longitudinal momentum 1 and momentum 2. To do so, we first summed back the signals from the left and right-well states. The data is plotted in fuchsia. Lines represent normal distributions with variances $\sigma_b^2 = mS$ (black, dashed), σ_n^2 (red, solid), $\sigma_b^2 + \sigma_n^2$ (blue, solid), $\xi^2 mS + \sigma_n^2$ with $\xi^2 = 0.09$ (black, solid). (d) Same as in (c) with $\xi^2 = 0.07$. However here, we first need to sum up the signals from the three m_F states.

signal corresponding to the longitudinal momentum $p_1 = -\hbar k_0$ and the total signal relative to the momentum $p_2 = \hbar k_0$. We need to sum back the left and right components in the separation procedure case. This step is unnecessary for the interference procedure, but we need to sum over the three m_F states. We obtain, in both cases, sub-binomial fluctuations that were estimated to be $\xi^2 = 0.09 \pm 0.04$ for the separation procedure, and $\xi^2 = 0.07 \pm 0.04$ for the interference one. In Fig. 5.4.(c,d) we show the histograms of the fluorescence signal difference $\hat{s}$ in units of the binomial standard deviation $\sigma_b = \sqrt{S}$ for the separation scan (c) and the interference one (d). The black curve is a normalized Gaussian using the squeezed variance $\xi^2\sigma_b^2$ as its variance. The blue and dashed black curves use the usual binomial variance instead and differ by the imaging detection noise (red curve).
The same analysis was performed using a more appropriate shape for the white boxes surrounding the single-particle states in Fig. 5.4.(a,b). In Fig. 5.5 we have used ellipses to contour the DTB signal. The values of the number-squeezing parameter we estimated using ellipses instead of rectangular boxes are $\xi^2 = 0.09 \pm 0.04$ for the separation procedure, and $\xi^2 = 0.04 \pm 0.03$ for the interference one.

5.3 Two-particle state identification

We will now provide the experimental evidence that has been collected to prove that the outcome of the double twin-atom beam procedure outlined in Chapter 4 is the maximally entangled state in Eq. (4.14):

$$|\Psi_{DTB}\rangle = \frac{1}{\sqrt{2}}(|L\rangle_- |L\rangle_+ + |R\rangle_- |R\rangle_+), \tag{5.9}$$

which is the archetypal state also used in the EPR paper of 1935 mentioned in Section 2.4. To gain information on the initial state we produce, we perform left and right well separation measurements (also defined as position measurements in Section 4.2.3), where we count how many atoms fell into the left and right well. We then combine this information with left and right well overlap measurements (also defined interference measurements or measurements in momentum space in Section 4.2.3), where we let the qubit freely expand, and we look at atom-atom correlations.
This approach is explained to some extent in [18], and more recently in the paper [77], where we analyzed two data sets, one (190903scan2) collected using the separation procedure, the second one (190905scan7) using the interference procedure.
Here, we intend to go through the analysis of those two data sets in more detail. As already pointed out before, our experiment and, in particular, the available long time of flight for the transverse direction (see Section 3.4.2) allows for measurement of atomic density profiles in both position and momentum space. We define *separation procedure* the experimental procedure that projects the atomic profiles into left and right components, allowing us to count how many atoms fell into the left or right waveguide and then compute the atom number-squeezing among any two signals coming from the four single-particle modes (left-well and momentum 1, right-well and momentum 1, left-well and momentum 2, right-well and momentum 2). This analysis can reveal which particular twin pairs are generated but cannot exclude the possibility of emitting only mixed states (two-particle states that can be factored into products of two single-particle states in a certain representation.) Therefore, in the so-called *interference procedure* we release the atomic qubits from the confinement

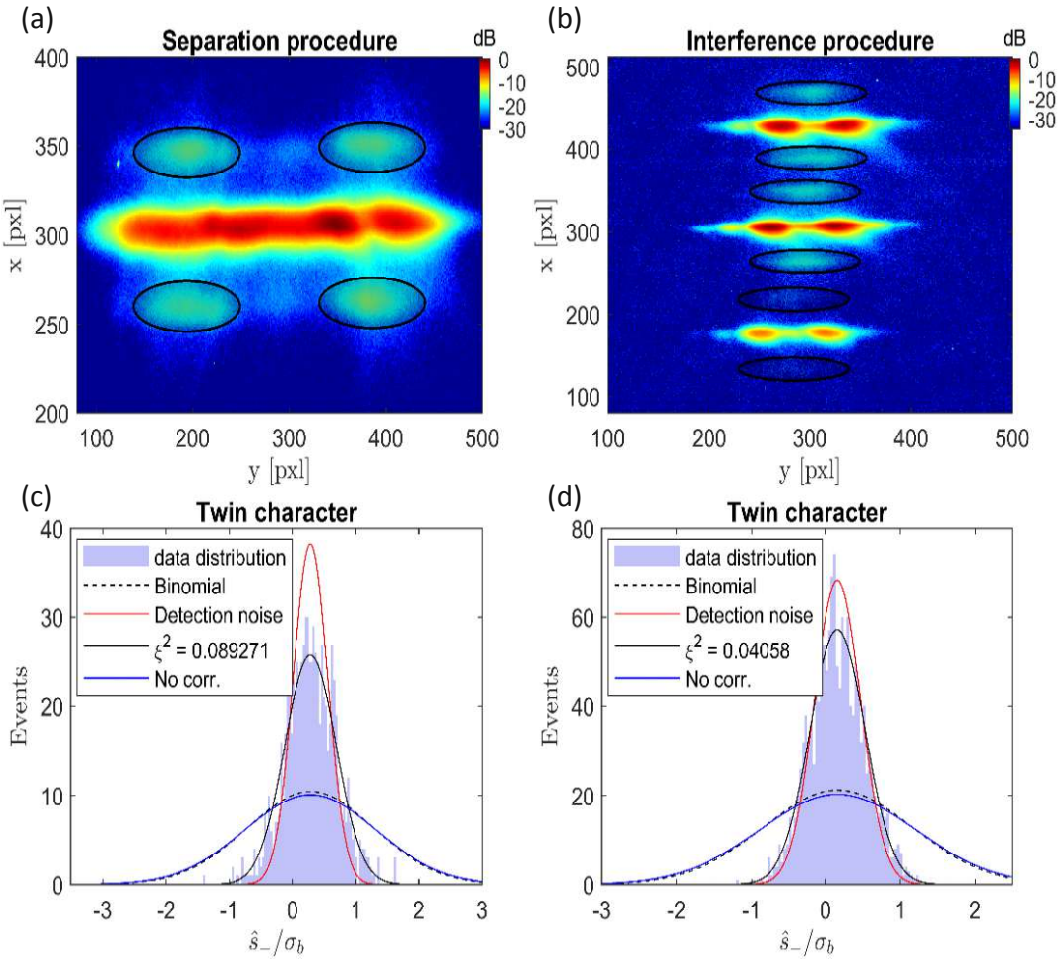

Figure 5.5: Twin character of the DTB emission (a) *Separation scheme*: experimental fluorescence image averaged over 798 experimental runs in dB scale (referenced to the brightest pixel). The central brightest signal corresponds to the main BEC. The four single-particle states available to the DTB emission are surrounded by elliptical boxes (in black), that are used to count how many atoms fell in each single-particle state. (b) *Interference scheme*: experimental fluorescence image averaged over 1497 experimental runs in dB scale. Each run involves $\approx$ 800 total atoms, on average 25 of which are DTB atoms ($\approx$ 12 pairs). The same pattern (BEC + DTB emission) is here repeated three times since we separated the three m_F states using a Stern-Gerlach experiment. The two longitudinal states are visible for each m_F component. (c) Statistics of the signal difference $\hat{s}$. Lines have the same meaning of Fig. 5.4.c with $\xi^2 = 0.09$. (d) Same as in (c) with $\xi^2 = 0.04$.

potential without any transverse momentum kick. Given the long time of flight (44 ms), they transversally expand, overlap, and interfere. A second-order atom-atom correlation analysis will then reveal a coherent superposition between a pair being emitted into the left waveguide and the same pair being emitted into the right one, hence excluding the presence of only mixed states of such twin pairs. Moreover, the specific quantum superposition detected in this experiment is consistent with the predicted zero relative phase between the left and right twin pairs in Eq. (5.9).

5.3.1 Number-squeezing results

The *separation procedure* projects the DTB emission into the four single-particle states $|L_1\rangle, |L_2\rangle, |R_1\rangle, |R_2\rangle$[1] and aims at counting how many atoms belong to each single-particle state. The number-squeezing analysis will then give us information on the two-particle state generated.

After the trap characterization of Section 4.2.1 and the state inversion of Section 4.2.2, the main BEC is ready to generate double twin atoms pairs. Normally, the long time-of-flight combined with the tight transverse y confinement does not allow the in-trap separated atomic components from different waveguides to separate. In order to detect all the four single-particle states, an extra step is then necessary. This extra stage happens with a quick increase of the potential barrier separating the two waveguides. The radiofrequency field parameter $R_f(t)$ of Eq. (4.11) is increased from $R_f(t) = 0.51$ (final double-well potential) to $R_f(t) = 0.81$ in 0.025 ms. Such a rapid increase of the radiofrequency field parameter $R_f(t)$ (and consequently of the potential barrier) results in an extra transverse acceleration that separates the left and right well components. This procedure projects four distinct zones on the final picture and counts the atoms in the two wells separately.

Let us consider the data set labeled SEPAR19 in Table 5.1. The analysis procedure starts with the background and etaloning correction (see Section 4.4.1). The corrected images have very low mean background level (~ 0 counts/pxl) and low mean background variance (~ 0.016 counts^2/pxl).

A typical picture from the *separation procedure* is displayed in Fig. 5.6. Along the vertical axis is the longitudinal wave-number $k_x = p_x/\hbar$, and on the horizontal axis is the transverse wave-number $k_y = p_y/\hbar$. Both axes are expressed in units of the longitudinal momentum $k_0 = \sqrt{2m\omega_y/\hbar}$ (see Section 4.1). The signal at the center in Fig. 5.6.a comes from the main BEC. At the corners of the image one can see the signal from the four single-particle modes $|L_1\rangle, |L_2\rangle, |R_1\rangle, |R_2\rangle$, centered at $k_x = \pm k_0$ and separated into L and R. The four black boxes around them define the integration area. In Fig. 5.6.(b-e) we plot the atom number in a certain single-particle state corresponding to the signal from one of the four black boxes in (a) as a function of the atom number in an another box. When considering signals from only the two left boxes at different momenta (LL) or from only right boxes at different momenta (RR), we see a higher correlation (the corresponding distribution is narrower) than between the signals from left and right boxes mixed (LR and RL). We now want to estimate this effect in a quantitative way applying the number-squeezing techniques of Section 4.5. We will then compare the experimental results with the simulation of the emission of DTB pairs of Section 4.5.1.

The data we analyze consists of many experimental cycles of the same separation procedure outlined in Section 4.2.3. The outcome is made of hundreds of images

[1] L and R stand for left and right well, while 1, 2 refers to the longitudinal momenta $p_{1,2}$ which, as we already saw in Section 4.1, are such that $p_{1,2} = \pm\hbar k_0$.

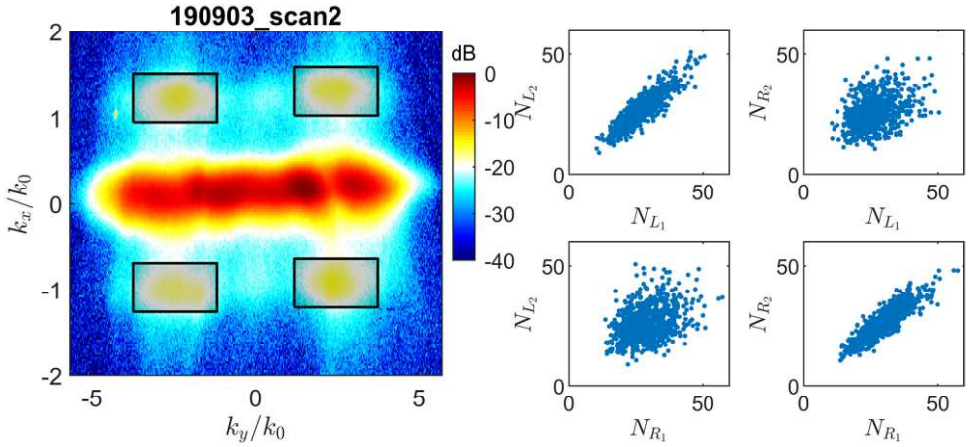

Figure 5.6: Separation procedure (a) Experimental fluorescence image averaged over 798 experimental runs from the SEPAR19 data set (see Table 5.1). Each run involves 2000-2200 total atoms, on average 100 of which are DTB atoms (50 pairs). The brightest central cloud (red) corresponds to the source state (at rest longitudinally), while the emitted DTB atoms are found at $k_x \approx \pm k_0$. The black boxes define the regions used for statistical analysis. (b,c,d,e) Atom number N_{i_1} at momentum 1 versus atom number N_{j_2} at momentum 2 with $i, j = \{L, R\}$. It is possible to visually notice the stronger correlation present in the LL and RR signals, as compared to the odd combination LR and RL. This effect can be estimated quantitatively using number-squeezing techniques. To derive how many atoms fell in each single-particle state we integrated the signal in the black boxes in (a) and divided by the photon-per-atom parameter for this data set $m = 29.4$.

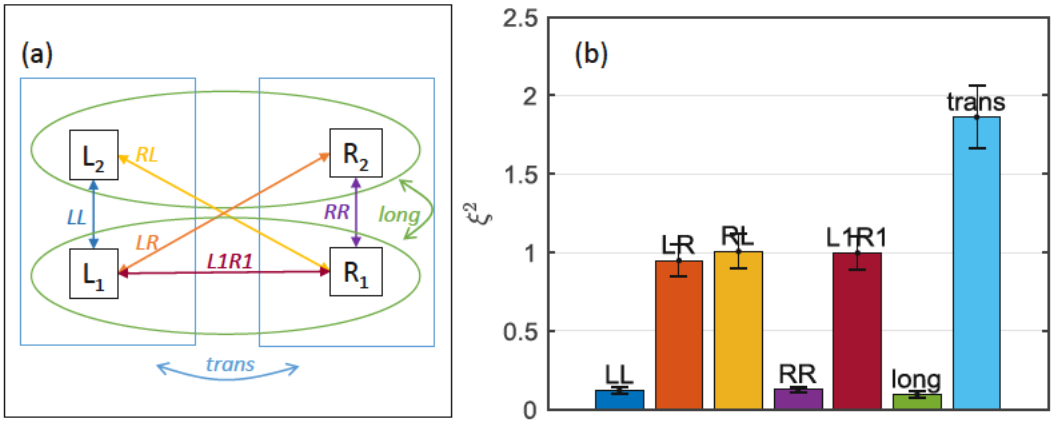

Figure 5.7: Number-squeezing technique applied to the different single-particle modes of the SEPAR19 data set: (a) Scheme of the different relevant combination of two-by-two single-particle modes and definition of the notation used. (b) Number-squeezing parameter estimated using Eq. (5.10) for the different combination of modes of (a). Error bars are given by the standard error of the mean computed using a bootstrapping method. The scenario is compatible with the emission of LL and RR pairs, as explained in Section 4.5.1.

similar to Fig. 5.6.a. From the images, we extract the signals $\hat{S}_{L_1}$, $\hat{S}_{R_1}$, $\hat{S}_{L_2}$, $\hat{S}_{R_2}$ contained in the four black rectangular boxes in Fig. 5.6.a, where the hat-symbol helps reminding us we deal with a statistical quantity.
We then consider the correlations among two signals contained in any pair of the black boxes defined in Fig. 5.6.a and identify each combination with the notation used in the scheme in Fig. 5.7.a. For each combination of two single-particle modes $\hat{s}_1$ and $\hat{s}_2$, where $\hat{s}_- \equiv \hat{s}_1 - \hat{s}_2$ and $\hat{S} \equiv \hat{s}_1 + \hat{s}_2$, we compute the value of the noise-corrected number-squeezing parameter using the definition of Eq. (4.26):

$$\zeta^2 = \frac{\mathrm{var}(\hat{s}_-)}{\sigma_b^2 \hat{s}_-} - \zeta_n^2, \tag{5.10}$$

where $\mathrm{var}(\hat{s}_-)$ represents the variance of the signal difference $\hat{s}_-$ between the two boxes considered, $\sigma_b^2 \hat{s}_- \equiv \hat{S}$ denotes the corresponding binomial variance, m is the photon-per-atom parameter for this data set, and ζ_n^2 the noise contribution to the squeezing parameter, which is given by:

$$\zeta_n^2 \simeq 2/m, \tag{5.11}$$

in the limit of zero mean background level, which is the case for the corrected images from which we extract the DTB signal. For this data set, using the formula Eq. (5.11), we get $\zeta_n^2 = 2/29.4 = 0.068$. To estimate the standard error of the mean relative to the squeezing parameter ζ^2 we adopted the bootstrapping method.
A value of $\zeta^2 < 1$ defines a number-squeezed emission. In Fig. 5.7.b the number-squeezing value ζ^2 is displayed as vertical bars as a function of the different combinations of DTB modes considered in Fig. 5.7.a. The actual values are also expressed in Table 5.2.
We observe that the different combinations of DTB modes can be classified into three groups depending on the value of the number squeezing[2]: (a) $\zeta^2 \approx 0$ for LL, RR,

[2]Refer to Fig. 5.7.a for the definition of the notation used.

Data set	ξ^2_{LL}	ξ^2_{LR}	ξ^2_{RL}	ξ^2_{RR}	ξ^2_{L1R1}	ξ^2_{long}	ξ^2_{trans}	ξ^2_n
SEPAR19	0.12(2)	0.9(1)	1.0(1)	0.13(2)	1.0(1)	0.101(18)	1.8(2)	0.068(3)

Table 5.2: **Number-squeezing** Noise-corrected atom number-squeezing for the relevant combinations of the four single-particle modes visualized in Fig. 5.7.

Data set	ξ^2_{LL}	ξ^2_{LR}	ξ^2_{RL}	ξ^2_{RR}	ξ^2_{L1R1}	ξ^2_{long}	ξ^2_{trans}	ξ^2_n
SEPAR19	0.12(2)	0.9(1)	1.01(11)	0.12(2)	1.0(1)	0.095(18)	1.9(2)	0.068(3)

Table 5.3: **Number-squeezing** Noise-corrected atom number-squeezing using ellipses to contour the DTB zones, as in Fig. 5.5.a, corresponding to the relevant combinations of the four single-particle modes visualized in Fig. 5.7.

long (b) $\xi^2 \approx 1$ for LR, RL, $R1L1$ (c) $\xi^2 \approx 2$ for *trans*. Group (a) refers to correlations between atoms that have opposite longitudinal momenta and belong to the same waveguide (LL or RR) or any of them (*long*). This characteristic defines atoms belonging to the same twin pair (see Section 5.2); hence we find $\xi^2 \ll 1$. Group (b) refers to atoms that either do not belong to the same waveguide (LR and RL) or do not belong to the same twin pair ($R1L1$). In both cases, the signals are uncorrelated, and we find $\xi^2 \approx 1$. The last group (c) contains the combination *trans*, which compares the total signal in the left and in the right waveguide. Given the state in Eq. (5.9), we expect twin *pairs* to be detected either in the left or in the right waveguide, without correlation between these two modes. However, each atom is part of a twin pair, so the *atom* detection is not left-right uncorrelated. In terms of the statistics of individual atoms, we find $\xi^2_{trans} = 2$, as already found when simulating the DTB emission in Section 4.5.1.
In conclusion, if we now compare our results with the simulated values for the squeezing parameter in Section 4.5.1 and in particular with Fig. 4.14, we notice that our findings are in agreement with the values of the squeezing parameter corresponding to a population angle $\theta \approx 0$. This suggests an emission that happens in a state involving mostly $|LL\rangle$ and $|RR\rangle$, a statistical mixture of the two, or a superposition of those two. In order to discriminate between a statistical mixture and a coherent superposition of $|LL\rangle$ and $|RR\rangle$, the number-squeezing technique used so far is useless. In the next section, we will look at atom-atom correlations and two-particle interference effects.
We also applied the same number-squeezing techniques for state identification in a separation procedure using ellipses to contour the DTB zones instead of simple rectangular boxes, as in Fig. 5.5.a. The results for the number-squeezing parameter of the different two-by-two combinations of modes are reported in Table 5.3 for completeness.

5.3.2 Atom-atom correlations

In our experiment, each twin pair can be emitted in either the L or R waveguide. These represent two two-particle quantum paths that interfere with equal amplitude (balanced double-well) when performing an interference measurement procedure, i.e., we avoid imprinting an extra transverse acceleration (see Fig. 4.1.c). Unlike the single-particle case, where an interference pattern is visible already in the mean density in momentum space (one-particle property), in the two-particle case, we need to look at two-particle properties to extract information on the final state [18].

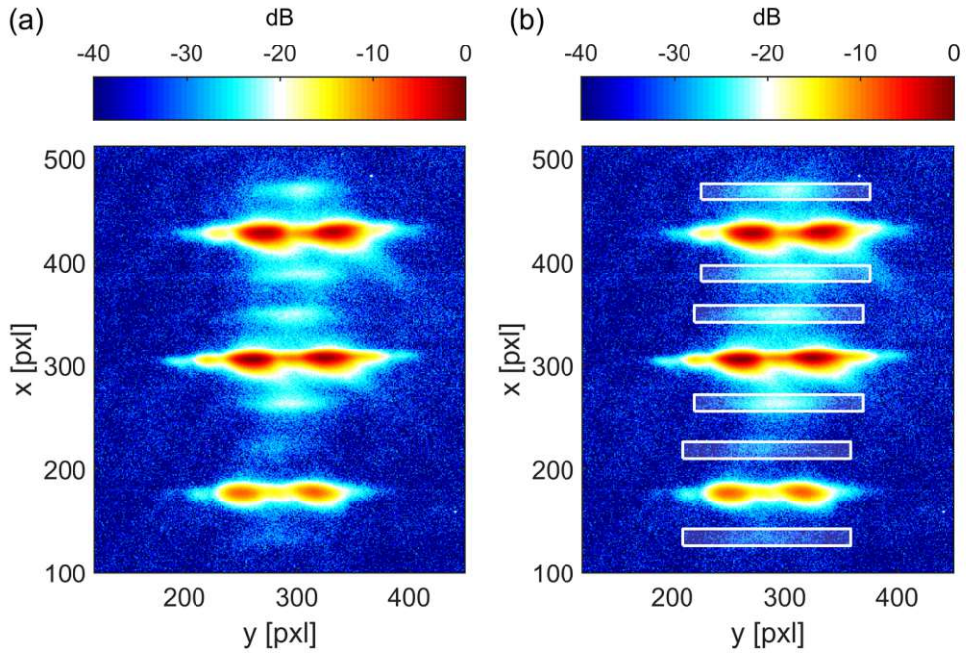

Figure 5.8: Interference procedure (a) Experimental fluorescence image averaged over 1497 experimental runs from the INTER19 data set (see Table 5.1). The image is in logarithmic scale (dB referred to the brightest pixel). Each run involves ≈810 total atoms, on average 24 of which are DTB atoms ($\sim$ 10 pairs). The same pattern (BEC + DTB emission) is here repeated three times since we separated the three m_F states using a Stern-Gerlach experiment. We do not separate left and right states. The two longitudinal states are visible for each m_F component. (b) Same figure as (a). The white boxes define the regions used for statistical analysis. We chose a box with sides equal to $[\mathrm{d}x, \mathrm{d}y] = [16 \times 150]$ pxl^2.

As already discussed in Section 4.6, if the DTB emission preserves the coherence of the quasi-BEC, the underlying density matrix relative to that state can reveal itself in form of a fringe pattern in the atom-atom second-order correlation function $G^{(2)}(p_1, p_2)$ in momentum space. In particular, a state as the one predicted in Eq. (4.14) shows an anti-diagonal fringe pattern (see Fig. 4.15). Maximal contrast requires identifying the partners in each atom pair. In a low-pair emission regime, we emit an average of 10 DTB pairs in each experimental run. Averaging over the many pairs will reduce the contrast in the observed interference.
In this section, we analyze the data named INTER19 in Table 5.1. The analysis procedure starts with the image background and etaloning correction treatments (see Section 4.4.1). For each data set obtained with the interference procedure, we use a Stern-Gerlach separation of the different m_F states to obtain cleaner fringes. In fact, each m_F state undergoes a slightly different time-of-flight trajectory that would result in a transverse relative shift which we would not be able to compensate for had we not separated the different Zeeman substates. Furthermore, since we do not raise the barrier at the end of the sequence in an interference measurement, we expect only the longitudinal $\pm k_0$ separation but no L/R separation. A typical picture from the *interference procedure* is displayed in Fig. 5.8. Along the vertical axis is the longitudinal direction in units of the camera pixels, and on the horizontal axis is the transverse direction (equivalent to the double-well axis). The three repeated patterns in Fig. 5.6 come from the aforementioned Stern-Gerlach separation of the three

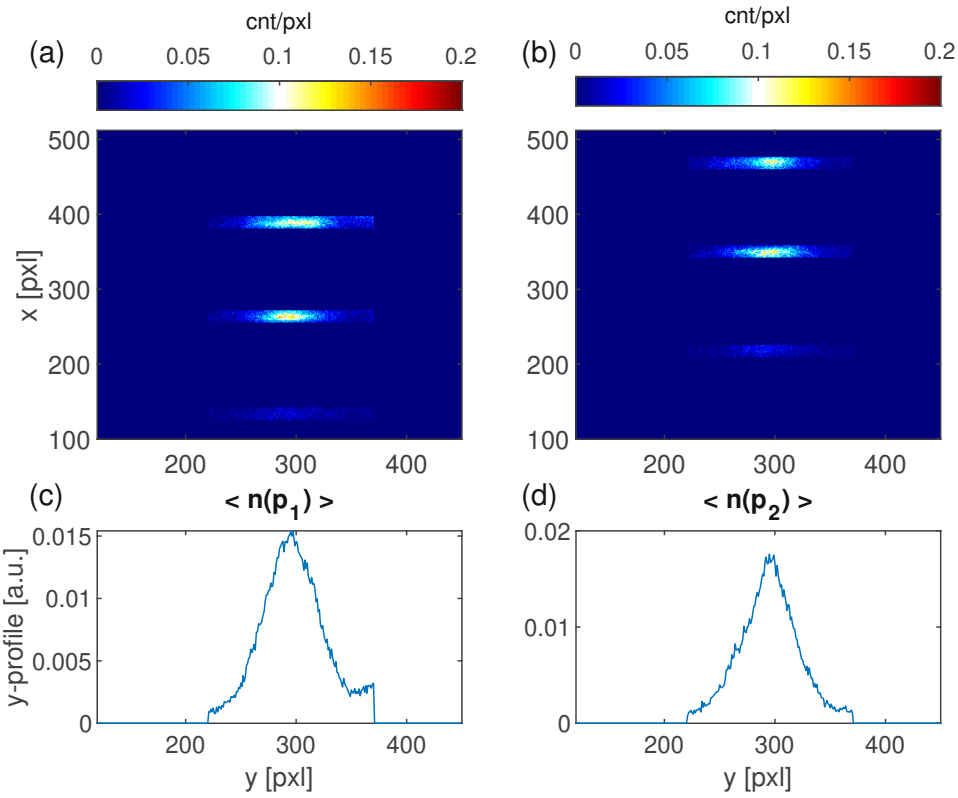

Figure 5.9: Recomposing the three m_F density profiles (a) The image shows the DTB signal from the averaged picture corresponding to the longitudinal momentum 1, after the three m_F states were aligned with the respect to the central one. The shifts were by 6 pxl for the upper m_F state, and by 11 pixels for the lower m_F state. (b) DTB signal from the averaged picture corresponding to momentum 2. (c) Density profile $\langle n_(p_1)\rangle$ corresponding to momentum 1, from the averaged image, normalized to the total fluorescence counts. (d) Density profile $\langle n_(p_2)\rangle$ corresponding to momentum 2, from the averaged image, normalized to the total fluorescence counts.

m_F states of the $F = 1$ state of ^{87}Rb. There is a brighter signal at the center for each pattern from the main BEC and two clouds at different longitudinal locations, symmetrically to the main BEC (at zero momentum longitudinally): the double twin-atom signal, centered around the expected longitudinal momentum. In Fig. 5.6.b we show the rectangular boxes chosen to contour the DTB zones (two for each m_F state). In Section 5.2, we integrated the signal in each box for each experimental run and computed the atom-number squeezing parameter relative to this data set.
We will now derive the density profiles at the two longitudinal modes $n(p_1)$ and $n(p_2)$. We integrate the DTB signal along the longitudinal axis and recompose the profiles by adding up from the three m_F states, keeping the signals relative to each momentum class separated. Each m_F state is also slightly misaligned along the y transverse direction, so we shift them properly before summing them. This procedure is exemplified in Fig. 5.9, where it is applied to the averaged images (a,b) for visualization purposes. In reality, we apply this technique to the single-shot images, as prescribed by the definition of Eq. (4.35). In Fig. 5.9.(a,b), we separate the DTB signal from the rest of the image and aligned the different m_F states with respect to the central one. In Fig. 5.9.(c,d), we plot the density profiles relative to the two longitudinal momenta. Once the signals from the DTB zones have been organized

into two separate density profiles $n(p_1)$ and $n(p_2)$, corresponding to the longitudinal modes, we can evaluate $G^{(2)}(p_1, p_2)$, using Eq. (4.35). Firstly, we will slightly modify the notation of the density profiles to clarify that they are functions of the transverse momentum:

$$n(p_1) = n(k_y, -k_0), \tag{5.12}$$
$$n(p_2) = n(k'_y, +k_0), \tag{5.13}$$

where we replaced the momentum p with the corresponding wave-number $k_y = p/2\pi\hbar$. Using this notation, we can rewrite Eq. (4.35) as:

$$G^{(2)}_{exp}(k_y, k'_y) = \frac{\langle n(k_y, -k_0) n(k'_y, +k_0)\rangle}{\langle n(k_y, -k_0)\rangle \cdot \langle n(k_y, +k_0)\rangle}. \tag{5.14}$$

In Fig. 5.10 we show the result of the calculation over 1497 experimental runs. First of all, the wave-number k_y is re-scaled by the half inter-well spacing $y_0 = 0.75\ \mu$m, hence $K = y_0 k_y$ is a dimensionless quantity. Figg. 5.10.(a,d) show the normalized averaged density profiles $\langle n(K, \pm k_0)\rangle$ from the two longitudinal momenta. The normalization condition we imposed reads:

$$\sum_{K_{min}}^{K_{max}} \langle n(K)\rangle dK = 1. \tag{5.15}$$

As already mentioned in Section 4.6, for the two profiles we expect a Gaussian profile with an envelope function given by $\mathcal{A}^2(K) = \mathrm{e}^{-(K-K_0)/\sigma_K^2}/\sqrt{\pi}\sigma_K$ (in case of a perfectly balanced double-well). The fit function we used is given by $F_G(K) = A_0\mathcal{A}^2(K) + B_0$, where $A_0 \sim 0.5$ represents an amplitude factor and $B_0 \sim 0.3$ [a.u.] is an offset (maybe due to residual fluorescence counts). The fit functions are displayed in red in Figg. 5.10.(a,d). From the fit, we extracted the extension $\sigma_K \sim 0.4$ of the Gaussian envelopes.
In Fig. 5.10.b, we show the product of the averaged profiles in (a) and (d). In Fig. 5.10.c we plot the $G^{(2)}(k_y, k'_y)$ profile. The pattern is reminiscent of the anti-diagonal fringe in Fig. 4.15.
To compare theory with experiment, we assume two density matrices ρ_1 and ρ_2 which in the $\{L, R\}$ basis representation are given by:

$$\rho_1 = \frac{1}{2}\begin{pmatrix} 1 & 0 & 0 & 1 \\ 0 & 0 & 0 & 0 \\ 0 & 0 & 0 & 0 \\ 1 & 0 & 0 & 1 \end{pmatrix}, \quad \rho_2 = \frac{1}{2}\begin{pmatrix} 1 & 0 & 0 & 0.3 \\ 0 & 0 & 0 & 0 \\ 0 & 0 & 0 & 0 \\ 0.3 & 0 & 0 & 1 \end{pmatrix}. \tag{5.16}$$

Knowing the density matrices, we then apply Eq. (4.36) to find the corresponding theoretical $G^{(2)}_{th}$ pattern. In Fig. 5.11, we compare the theoretical $G^{(2)}_{th}$ patterns related to the ρ_1 and ρ_2 matrices [(Fig. 5.11.(a,b)], with the experimental $G^{(2)}_{exp}$ pattern obtained from the analysis of the current data set (Fig. 5.11.c).
It seems plausible that the state ρ_1 (or ρ_2) are the ones we produce in our DTB scheme. The main drawback of our system is the poor contrast of the fringe pattern in Fig. 5.11.c. One possible explanation for the low contrast of the fringe pattern is the many pairs emitted at the same time, which makes it impossible to identify each atom's twin. Moreover, the multi-pair emission regime generates higher-order emission terms, as we will explain in Section 6.1. Even decreasing the average number of emitted pairs, we may not be able to detect those single pairs: our EMCCD

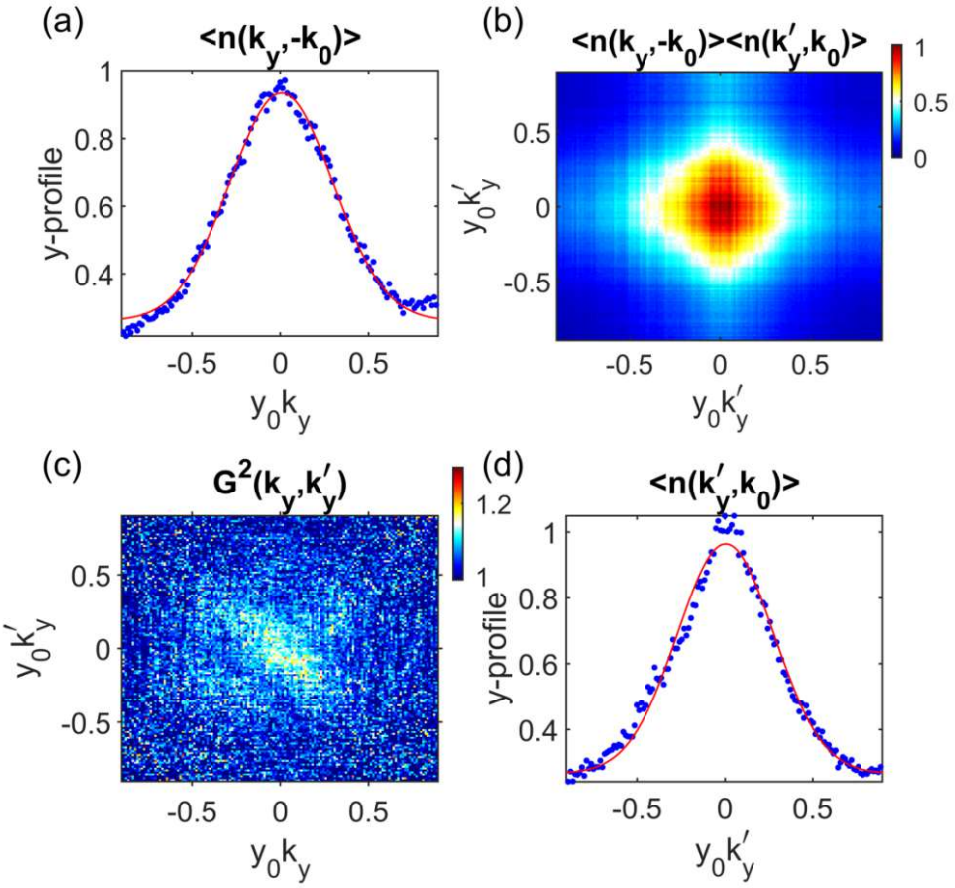

Figure 5.10: Second order correlation function $G^{(2)}(k_y, k'_y)$ of atomic profiles within twin pairs as a function of transverse momentum after long time-of-flight. (a) Averaged atomic profile relative to the atoms within the twin pairs with longitudinal momentum $-k_0$. (b) Product of the averaged atomic profiles from the two different longitudinal momentum classes $\pm k_0$. (c) Second order correlation function $G^{(2)}_{exp}(k_y, k'_y)$. The axes are re-scaled by the half inter-well distance $2y_0 = 1.3\ \mu$m. (d) Averaged atomic profile relative to the atoms within the twin pairs with longitudinal momentum $+k_0$.

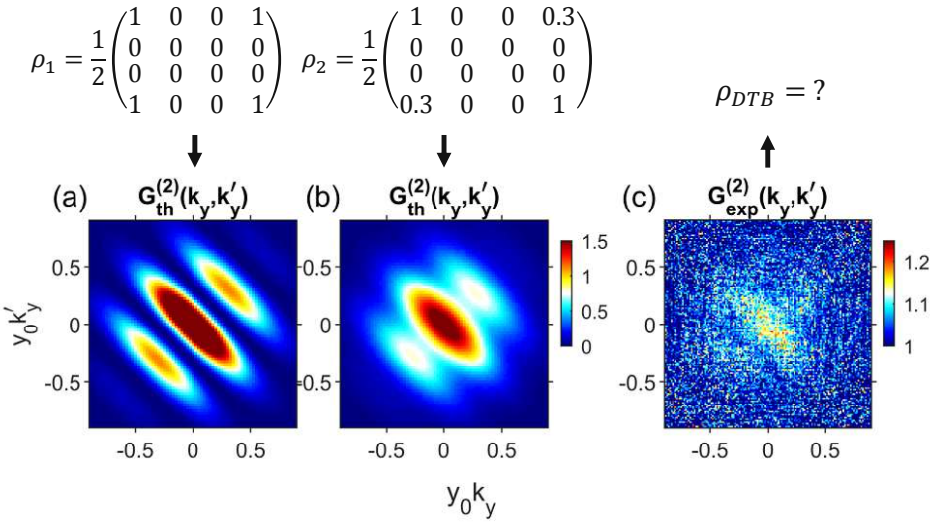

Figure 5.11: $G^{(2)}(k_y, k'_y)$: theory vs experiment comparison. (a) Simulated $G^{(2)}_{th}(k_y, k'_y)$ pattern that assumes a density matrix ρ_1. In order to evaluate the $G^{(2)}_{th}(k_y, k'_y)$ pattern, we used Eq. (4.36). (b) Simulated $G^{(2)}_{th}(k_y, k'_y)$ pattern that assumes a density matrix ρ_2. (c) Experimental $G^{(2)}_{exp}(k_y, k'_y)$ pattern evaluated from Eq. (5.14) using the experimental atomic profiles.

light-sheet detector is not capable of reliably discriminating between single-atom signal and detection noise (mainly CIC or clock-induced charges, multiplied at the electron-multiplication stage [55]).
In the following, we will see how we can estimate the level of contrast of the experimental fringe pattern.

Attempt to estimate of the contrast of the fringe pattern

The $G^{(2)}_{exp}(k_y, k'_y)$ fringe pattern in Fig. 5.11.c would allow, once properly fitted, to extract information on the initial two-particle state [18]. In particular, when the main pattern contains anti-diagonal or diagonal fringes, as in our system, full tomography is possible. The main difficulty of this state reconstruction method, proposed for our system in the paper [18], is represented by the poor contrast of the fringe pattern of Fig. 5.11.c, which makes it hard to fit any function to it.
In order to fit the anti-diagonal profile of the $G^{(2)}_{exp}(k_y, k'_y)$ pattern, we first fit the anti-diagonal profile of the $\langle n(k_y, -k_0)\rangle \cdot \langle n(k_y, +k_0)\rangle$ pattern with a non-linear least squares method using a Lorentzian envelope function $F_L(k_y) = A_0 \cdot \exp\left(-(k_y - B_0)^2/C_0^2\right) + D_0$.

$$\begin{aligned} A_0 &= 0.8085(0.8027, 0.8143) \\ B_0 &= 0.003529(0.001748, 0.005309) \\ C_0 &= 0.5691(0.5632, 0.575) \\ D_0 &= -0.04781(-0.05233, -0.04329) \end{aligned} \tag{5.17}$$

Once we know the envelope function, we can fit the averaged anti-diagonal profile

of the $G^{(2)}_{exp}(k_y, k'_y)$ pattern using the fit function $F_{fit} = F_{fit}(\tilde{K})$ given by:

$$F_{fit}(\tilde{K}) = F_L(\tilde{K}) \cdot E_0 \left[\cos\left(\frac{2\pi \cdot 2(\tilde{K} - K_0)}{F_0} \right) + G_0 \right] + H_0, \tag{5.18}$$

where the envelope is fixed from the previous fit, G_0 and H_0 are two vertical offsets, K_0 is a horizontal offset, F_0 is a fringe spacing amplitude factor, while E_0 defines the contrast of the fringe pattern. The factor 2 within the cosine function comes from the specific $G^{(2)}_{exp}(k_y, k'_y)$ pattern relative to the anti-diagonal pattern in Fig. 4.15. The coefficients of the fit (with 95% confidence bounds) are:

$$\begin{aligned} E_0 &= 0.0346(0.02964, 0.03956) \\ F_0 &= 1.322(1.251, 1.393) \\ G_0 &= 0.1189(0.1105, 0.1274) \\ H_0 &= 1.017(1.012, 1.022) \\ K_0 &= -0.01693(-0.03225, -0.001607). \end{aligned}$$

In particular, the fringe spacing factor being $F_0 = 1.25 - 1.39$ would mean that the measured fringe spacing is between 25% up to 39% larger than expected for a perfect match between the simulated and the experimental final double-well potentials. The estimated inter-well distance is $d_{exp} = 2y_0/E_0 = 1$ μm, which would be 0.3 μm smaller than for the simulated double-well potential (wells more coupled in the experiment compared to simulation). However, the information that one can extract from the fit can only be trusted proportionally to the level of contrast we can achieve: the measured contrast of the fringe pattern for this data set is as low as $C_0 = 0.035 \pm 0.005$. One can also define the visibility $\mathcal{V}$ of the measured fringe pattern from the fit function F_{fit} as given by:

$$\mathcal{V} = \frac{max(F_{fit}) - min(F_{fit})}{max(F_{fit}) + min(F_{fit})} \simeq 0.051. \tag{5.19}$$

The measured contrast and visibility are too low (a few percent only) to judge the fringe spacing factor too confidently.
As a final plot, in Fig. 5.12 we display the results of the fit of the anti-diagonal fringe of the $G^{(2)}_{exp}(k, k')$ pattern, together with the Lorentzian fit of the anti-diagonal cut along the $\langle n(\hat{k}_y, -k_0) n(\hat{k}_y, k_0) \rangle$ pattern.
We perform a parallel analysis on the same data set using ellipses to contour the DTB signal instead of rectangular boxes. The results are similar and are summarized in Fig. 5.13.

A more recent data set

We repeated the interference analysis for a more recent data set named INTER21 in Table 5.1, obtained with the same procedure as for INTER19. The analysis follows the same steps as before in Section 5.3.2, but we here used an elliptical definition for the DTB boxes, as it was closer to the real shape of the DTB signal. A similar fringe pattern was obtained, confirming the previous results. We summarize the results of this data set in Fig. 5.14.

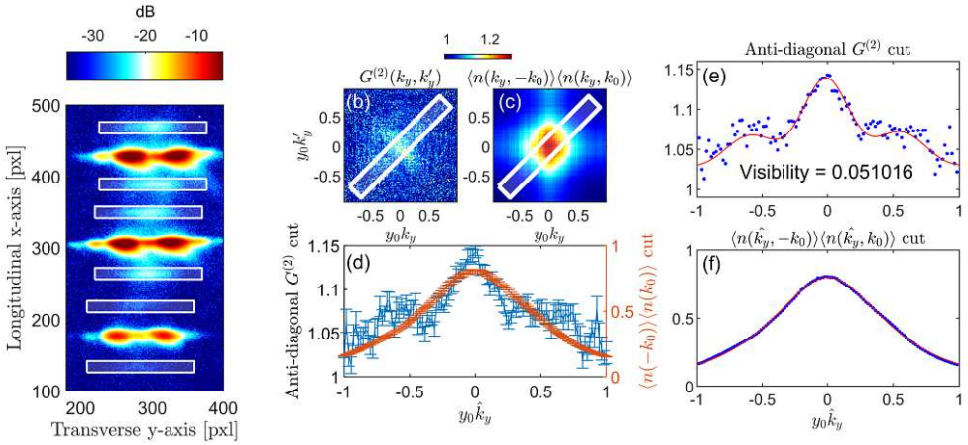

Figure 5.12: Summary of the results from the data set labeled INTER19 obtained using rectangles to contour the DTB signal. (a) Fit of the averaged anti-diagonal cut of $G^{(2)}_{exp}(k_y,k'_y)$. As fit function, we used a damped cosine where the contrast of the fringe E_0, the offsets G_0 and H_0 and K_0, and the correction factor to the fringe spacing F_0 are fit parameters. The contrast of the fringe pattern from the fit is estimated to be $C_0 = 0.034 \pm 0.005$ and its visibility $\mathcal{V} = 0.051$. (b) Fit of the corresponding anti-diagonal slice of $\langle n(\hat{k}_y,-k_0)n(\hat{k}_y,k_0)\rangle$. As fit function, we used a Lorentzian envelope.

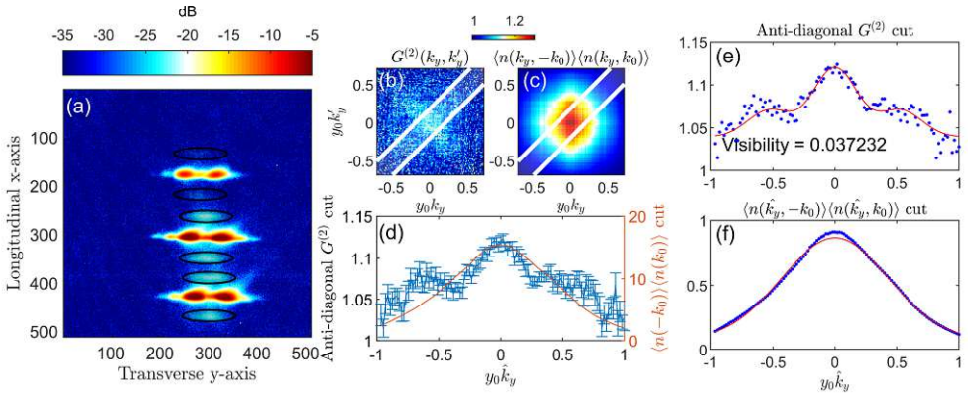

Figure 5.13: Summary of the results from the data set labeled INTER19 obtained using ellipses to contour the DTB signal. (a) Averaged corrected image from 1497 single-shot images with the same settings. The roi zones used for the correlation analysis are visible as black ellipses. (b) $G^{(2)}(k_y,k'_y)$ pattern computed as atom-atom correlation among the integrated transverse profiles withing the ellipses in (a) after we summed back the three m_F states. (c) $\langle n(\hat{k}_y,-k_0)n(\hat{k}_y,k_0)$ pattern. We highlight as white rectangular boxes the regions used to extract the averaged $G^{(2)}(k_y,k'_y)$ profile. (d) Mean anti-diagonal $G^{(2)}(k_y,k'_y)$ profile (light blue data) and mean $\langle n(\hat{k}_y,-k_0)n(\hat{k}_y,k_0)$ cut (orange data). (e) Fit of the averaged anti-diagonal cut of the $G^{(2)}(k_y,k'_y)$ pattern. As fit function we use a damped cosine, where the contrast of the fringe C_0, the vertical offsets D_0 and F_0, and the correction factor to the fringe spacing E_0 are fit parameters. The contrast of the fringe pattern from the fit is estimated to be $C_0 = 0.042 \pm 0.006$ and its visibility $\mathcal{V} = 0.05$. (f) Fit of the corresponding anti-diagonal slice of the $\langle n(\hat{k}_y,-k_0)n(\hat{k}_y,k_0)$ pattern. As fit function we employed a Gaussian envelope.

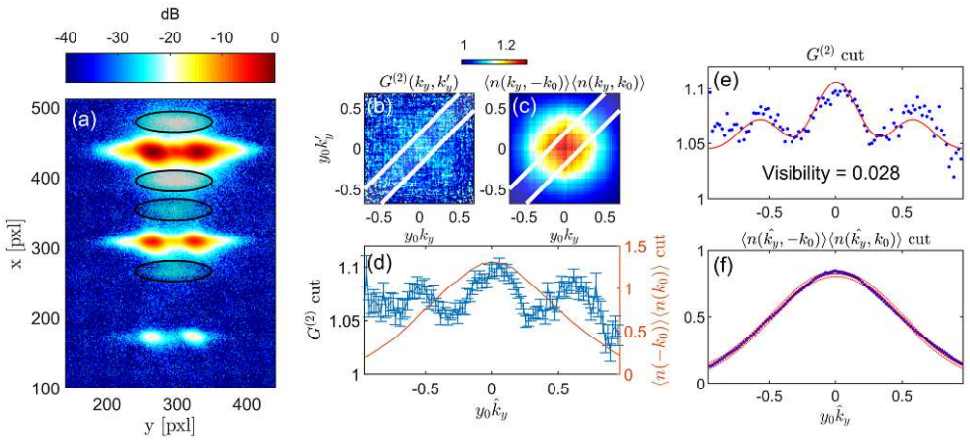

Figure 5.14: Summary of the results from the data set labeled INTER21 obtained using ellipses to contour the DTB signal. (a) Averaged corrected image from 636 single-shot images with the same settings. The roi zones used for the correlation analysis are visible as black ellipses. The lower m_F state had low enough population, so we excluded it from the rest of the analysis. (b) $G^{(2)}(k_y, k'_y)$ pattern computed as atom-atom correlation among the integrated transverse profiles withing the ellipses in (a). (c) $\langle n(\hat{k}_y, -k_0)n(\hat{k}_y, k_0)$ pattern. We highlight as white rectangular boxes the regions used to extract the averaged $G^{(2)}(k_y, k'_y)$ profile. (d) Mean anti-diagonal $G^{(2)}(k_y, k'_y)$ profile (light blue data) and mean $\langle n(\hat{k}_y, -k_0)n(\hat{k}_y, k_0)$ cut (orange data). (e) Fit of the averaged anti-diagonal cut of the $G^{(2)}(k_y, k'_y)$ pattern. As fit function we used a damped cosine, where the contrast of the fringe C_0, the vertical offsets D_0 and F_0, and the correction factor to the fringe spacing E_0 are fit parameters. The contrast of the fringe pattern from the fit is estimated to be $C_0 = 0.027 \pm 0.011$ and its visibility $\mathcal{V} = 0.028$. (f) Fit of the corresponding anti-diagonal slice of the $\langle n(\hat{k}_y, -k_0)n(\hat{k}_y, k_0)$ pattern. As fit function we employed a Gaussian envelope.

Chapter 6

Future directions

It is interesting to consider here a few questions arising naturally from the analysis of the data sets in Chapter 5. First of all, we always assumed that many single pairs are emitted, but we also showed that we could not record single pairs in our experiment but rather 10 or 50 on average at a time. For this reason, in Section 6.1 we investigate the more general solution to the emission process. Then we look at the particular scenario of emitting two pairs simultaneously.
The second question that might arise has to do with time evolution: how do the atom-atom correlations evolve with time? In Section 6.2 we show a data set that gives a hint towards a somehow counterintuitive direction.
The last but important question relates to the $G^{(2)}$ pattern: is there a way, given our current setup, to modify the current scheme in such a way that we produce a different DTB state? Would a different DTB state then give rise to a modified $G^{(2)}$ pattern as expected (see the discussion in Section 4.3.2)? We consider this situation in 6.3.

6.1 Multi twin-atom pair states

The twin atoms are produced in pairs with opposite momenta $\vec{p}_1 = -\vec{p}_2$ with $|\vec{p}_1| = |\vec{p}_2| = \hbar k_0$, where $1, 2$ are the two longitudinal modes available due to energy and momentum conservation, which in the following we will represent with $\pm$ sign. We can write the corresponding two-mode squeezed Hamiltonian as:

$$H_{2M} \propto a_0 a_0 (a_-^\dagger a_+^\dagger + \text{h.c.}) = N_0 (a_-^\dagger a_+^\dagger + \text{h.c.}), \tag{6.1}$$

where $a_\pm$ are the annihilation operators for the two momenta modes $1, 2$ mentioned above. The time-evolution operator is given by (we are omitting the operator symbols):

$$U(t) = \exp(-itH_{2M}/\hbar) \propto \sum_m c_m (a_-^\dagger a_+^\dagger)^m. \tag{6.2}$$

In addition to the scenario above, two transverse modes L and R are available to the twin pairs in the double-well configuration, enabling an additional degree of freedom for the generation of twin-atom pairs. In particular, each pair travels along either the left L, the right R waveguide, or in a superposition of those. The generalized two-mode squeezed Hamiltonian reads:

$$H_{2MDW} = H_{2M}^L + H_{2M}^R \propto N_0 (a_-^{L,\dagger} a_+^{L,\dagger} + a_-^{R,\dagger} a_+^{R,\dagger} + \text{h.c.}), \tag{6.3}$$

where $a_\pm^L$ are the annihilation operators of the two momenta modes for the left waveguide and $a_\pm^R$ are the annihilation operators for the right one.

The DTB state at any later time $|\psi(t)\rangle = U(t)\,|0\rangle$ is then given by:

$$\begin{aligned}|\psi(t)\rangle &= \exp(-itH_L/\hbar)\exp(-itH_R/\hbar)\,|0\rangle = \\ &= (c_0^L\,|00\rangle_L + c_1^L\,|11\rangle_L + c_2^L\,|22\rangle_L + \ldots)(c_0^R\,|00\rangle_R + c_1^R\,|11\rangle_R + c_2^R\,|22\rangle_R + \ldots) = \\ &= c_0^L c_0^R\,|00\rangle_L\,|00\rangle_R + \\ &+ c_0^L c_1^R\,|00\rangle_L\,|11\rangle_R + c_0^R c_1^L\,|00\rangle_R\,|11\rangle_L + \\ &+ (2c_1^L c_1^R\,|11\rangle_L\,|11\rangle_R) + c_0^L c_2^R\,|00\rangle_L\,|22\rangle_R + c_2^L c_0^R\,|22\rangle_L\,|00\rangle_R + \ldots \end{aligned} \tag{6.4}$$

In the previous chapters, we only considered the possibility of emitting "many" single pairs of the type $c_0^L c_1^R\,|00\rangle_L\,|11\rangle_R + c_0^R c_1^L\,|00\rangle_R\,|11\rangle_L \sim |LL\rangle + |RR\rangle$. This scenario found a theoretical justification in Section 4.3 and, most importantly, experimental proofs in both the number-squeezing analysis of Section 5.3.1 and in atom-atom correlations in Section 5.3.2. However, the average number of pairs we emit (10 pairs on average in INTER19, INTER21, and up to 50 in SEPAR19) forces us to include other terms of Eq. (6.4) in the analysis. In particular, as the first more significant correction and as an outline and motivational push for further development of both theory and experimental confirmations, we will consider the possibility of emitting two pairs at a time.
Let us start with the state $\left|\psi_{2pair}\right\rangle$ describing four atoms altogether:

$$\left|\psi_{2pair}\right\rangle \propto |22\rangle_L + |22\rangle_R\,, \tag{6.5}$$

which describes the superposition of two twin pairs traveling along the left and the right waveguide at the same time.

6.1.1 Number-squeezing

In the simulation of the emission process in Section 4.5.1 that led to the number-squeezing results shown in Fig. 4.14, we have only assumed that each emitted pair is a twin-atom pair. Still, we have nowhere assumed anything on whether each pair is emitted alone or simultaneously in a bunch of two pairs at a time. Therefore, the results obtained in Fig. 4.14 are valid also for any state of the type:

$$|\psi_{DTB}\rangle \propto \left|N_pN_p\right\rangle_L + \exp(-i\theta)\left|N_pN_p\right\rangle_R\,, \tag{6.6}$$

where we indicated with $N_p = 1, 2, 3\ldots$ the number of simultaneously emitted pairs. Hence, the number-squeezing results discussed in Section 5.3.1 are compatible with the state of Eq. (6.5).

6.1.2 Atom-atom correlation

It is noteworthy to look at what we expect for a $G^{(2)}$ pattern in the case of the state in Eq. (6.5). To do that we start again from the definition of $G^{(2)}(\eta_1, \eta_2)$ given in Eq. (4.32) for a single pair. We want to generalize it to the situation of two twin-atom pairs labeled A and B:

$$\begin{aligned}G^{(2)}(\eta_1,\eta_2) = \langle\hat{\Psi}^\dagger(\eta_1)\hat{\Psi}^\dagger(\eta_2)\hat{\Psi}(\eta_1)\hat{\Psi}(\eta_2)\rangle = \\ \langle\hat{\phi}_B^\dagger(\eta_1)\hat{\phi}_A^\dagger(\eta_1)\hat{\phi}_B^\dagger(\eta_2)\hat{\phi}_A^\dagger(\eta_2)\hat{\phi}_A(\eta_1)\hat{\phi}_B(\eta_1)\hat{\phi}_A(\eta_2)\hat{\phi}_B(\eta_2)\rangle\end{aligned} \tag{6.7}$$

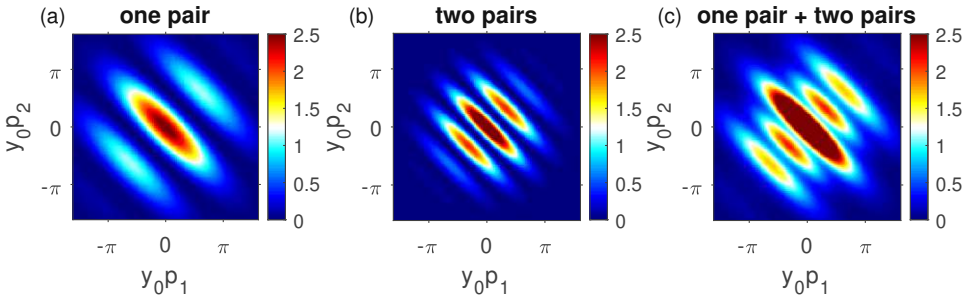

Figure 6.1: Superposition of two pairs: effect on $G^{(2)}(p_1, p_2)$ (a) Simulated $G^{(2)}_{th}(p_1, p_2)$ pattern that assumes coherent superposition of one left pair and one right pair. (b) Simulated $G^{(2)}_{th}(p_1, p_2)$ pattern that assumes coherent superposition of two left pairs and two right pairs (c) Sum of (a) and (b).

where $\hat{\Psi}(\eta) = \hat{\phi}_A(\eta)\hat{\phi}_B(\eta)$ and $1, 2$ refer to the atoms within each twin pair. In terms of the left L and right states R each pair can be written as a superposition:

$$\hat{\phi}_A = \sum_{i=L,R} \psi_i \hat{a}_i \tag{6.8}$$

$$\hat{\phi}_B = \sum_{j=L,R} \psi_j \hat{a}_j \tag{6.9}$$

where $\hat{a}_{L,R}$ are the annihilation operators for the corresponding transverse mode. Also we can then rewrite Eq. (6.7) in terms of those L, R modes to get:

$$G^{(2)}(\eta_1, \eta_2) = \sum_{ijkl,mnlp=L,R} \psi_i(\eta_1)\psi_j(\eta_2)\psi_k(\eta_1)\psi_l(\eta_2)\psi^\star_m(\eta_1)\psi^\star_n(\eta_2)\psi^\star_l(\eta_1)\psi^\star_p(\eta_2)\rho_{ijkl,mnlp} \tag{6.10}$$

which is a complicated formula that in the most general case would require a 16×16 matrix to represent the F-functions defined in Eq. (4.39).
Here, we perform the calculations relative to the simple state in Eq. (6.5), where there is a coherent superposition between two left pairs and two right pairs. In this simple case there are only four terms contributing to the $G^{(2)}(p_1, p_2)$ pattern:

$$\phi_{2L2L} = \phi_L(p_1)\phi_L(p_2)\phi_L(p_1)\phi_L(p_2)\phi^\star_L(p_1)\phi^\star_L(p_2)\phi^\star_L(p_1)\phi^\star_L(p_2) \tag{6.11}$$

$$\phi_{2L2R} = \phi_L(p_1)\phi_L(p_2)\phi_L(p_1)\phi_L(p_2)\phi^\star_R(p_1)\phi^\star_R(p_2)\phi^\star_R(p_1)\phi^\star_R(p_2) \tag{6.12}$$

$$\phi_{2R2L} = \phi_R(p_1)\phi_R(p_2)\phi_R(p_1)\phi_R(p_2)\phi^\star_L(p_1)\phi^\star_L(p_2)\phi^\star_L(p_1)\phi^\star_L(p_2) \tag{6.13}$$

$$\phi_{2R2R} = \phi_R(p_1)\phi_R(p_2)\phi_R(p_1)\phi_R(p_2)\phi^\star_R(p_1)\phi^\star_R(p_2)\phi^\star_R(p_1)\phi^\star_R(p_2) \tag{6.14}$$

such that

$$G^{(2)}(p_1, p_2) = \frac{1}{2}(\phi_{2L2L} + \phi_{2L2R} + \phi_{2R2L} + \phi_{2R2R}). \tag{6.15}$$

In Fig. 6.1.b we plot the results of the calculation and compare it with (a) the coherent superposition of a pair to the left and the same pair to the right and (c) the sum of the $G^{(2)}$'s for the two previous situations. This analysis shows that the results of our atom-atom correlation are compatible with the generation of more than one single pair at a time, given the coherent superposition among the left and right components. We are more inclined to believe that we see the superposition effects of a multi-twin-atom pair state rather than many single pairs effects only. Only a better understanding of the phenomena that tend to reduce the fringe contrast would help us narrow down the actual DTB state we produce.

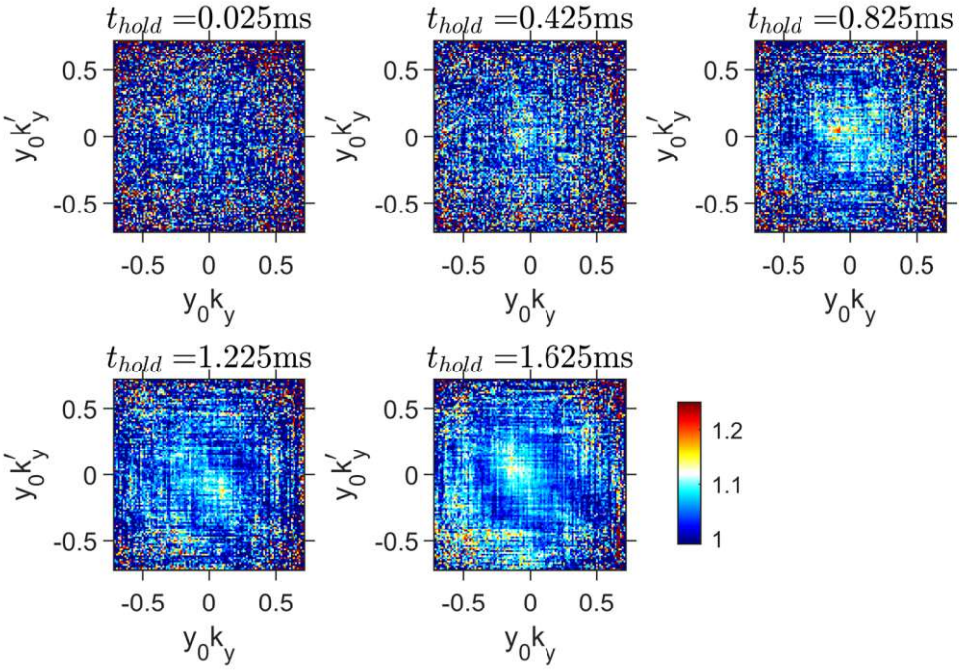

Figure 6.2: $G^{(2)}$ pattern evolution. The evINTER21 data set contains 120 images at each time t_{hold} and five time instants from 25 μs up to 1.625 ms after the the DTB sequence in steps of 0.4 ms.

6.2 Evolution of the DTB state

In the previous data sets we always referred to the shortest in-trap holding time possible, which for our setup is 25 μs. We here present the analysis of the data set labeled evINTER21 in Table 5.1 where we let the state evolve and measure at five different time instants corresponding to increasing in-trap holding time t_{hold}. For each time, we collected only 120 experimental realizations, which is not enough statistics to be able to see a signal in $G^{(2)}$ for the low-atom regime at $t_{hold} < 1$ ms but is enough to see a hint of a modification of the $G^{(2)}$ pattern as the in-trap holding time increases. The fact that the signal in the $G^{(2)}$ function seems to become more evident as the average number of emitted pairs increases appears at odds with our initial assumption of the emission of only a few pairs. If the experimental $G^{(2)}$ pattern was only produced by single pairs events, then it would grow larger as fewer pairs are emitted. The experimental $G^{(2)}$ pattern might instead emerge from multi twin-atom states as discussed in Section 6.1 rather than from many single pairs copies as we initially assumed.

6.3 Example of a modified $G^{(2)}$ pattern

In this section i will present data labeled modINTER21 in Table 5.1 relative to a slightly modified experimental procedure, that is pictured in Fig. 6.3. For the first part (a-c), the main BEC undergoes the same procedure as in Fig. 4.1. After the excitation via OCT ramp based rf dressing, instead of switching off the confinement, we perform a linear ramp of the rf amplitude towards decreasing values. In Fig. 6.3.d we see the rf amplitude ramping down from $R_f(t_1) = 0.491$ to $R_f(t_2) = 0.47$, where we indicated as t_1 the instant at the end of the OCT ramp and $t_2 - t_1$ is the duration

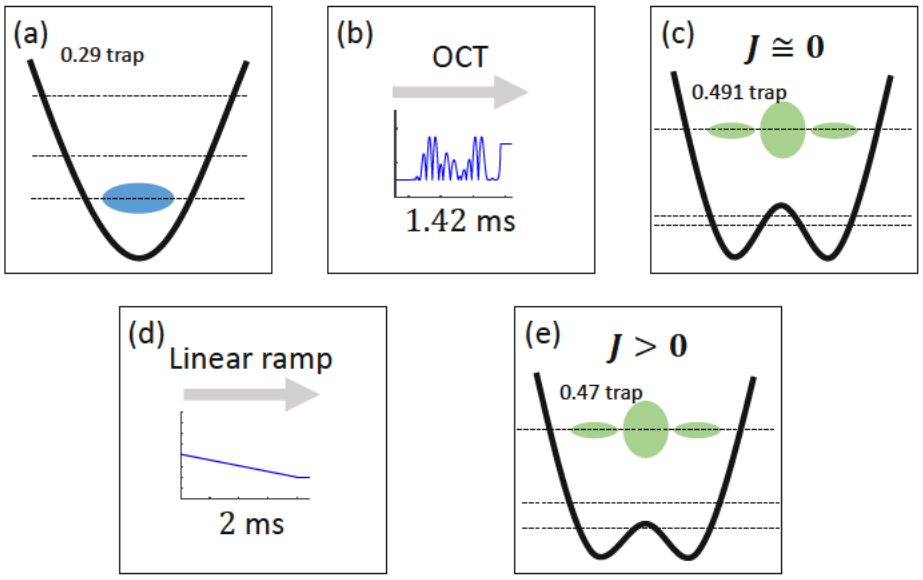

Figure 6.3: Sketch of the experimental procedure leading to a modified $G^{(2)}$ pattern. (a) We start at time t_0 with a slightly dressed single-well potential, where we produce our BEC that sits in the lowest vibrational state (light blue). (b) We then ramp the amplitude of the dressing rf field following the OCT ramp trajectory till time t_1. (c) The BEC now sits in the second excited state of a double-well potential (green), and is the source state for the emission of DTB pairs. (d) We then perform a linear ramp of the rf amplitude till time t_2, leading to a less de-coupled double-well potential. The tunneling coupling $J > 0$. The linear ramp lasts $t_2 - t_1 = 2$ ms and the amplitude of the rf field goes from $R_f(t_1) = 0.491$ to $R_f(t_2) = 0.47$. (e) The final double-well is held for the minimum time, then the confinement is switched off and the DTB pairs, together with the main BEC, undergo free fall and detection.

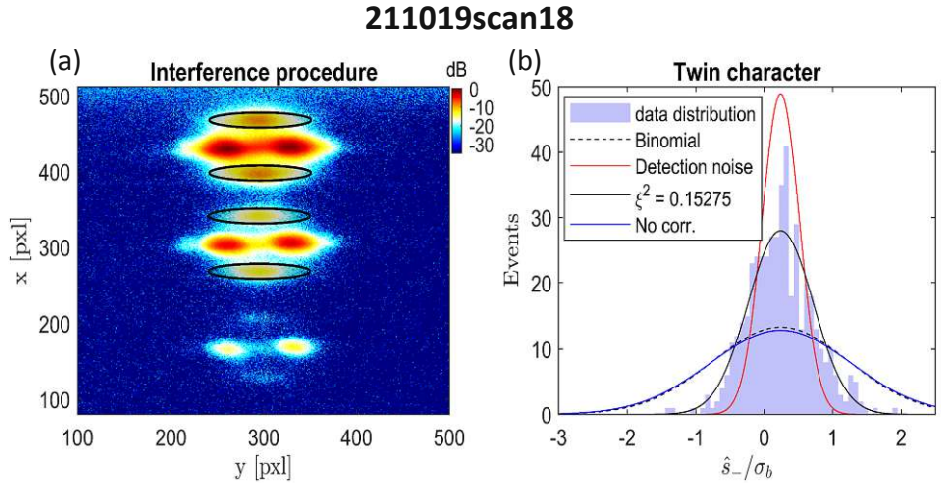

Figure 6.4: Modified interference procedure (a) Experimental fluorescence image averaged over 463 experimental runs obtained with the modified interference procedure sketched in Fig. 6.3. The image is in logarithic scale (dB referred to the brightest pixel). Each run involves ~ 895 total atoms, on average 100 of which are DTB atoms (~ 50 pairs). The same pattern (BEC + DTB emission) is here repeated three times since we separated the three m_F states using a Stern-Gerlach experiment. We do not separate left and right states. The two longitudinal states are visible for each m_F component. The black ellipses define the integration region for counting the DTB pairs. We exclude the lowest m_F that has negligible signal. (b) Statistics of the signal difference $\hat{s}$ between the momentum states 1 and 2. Lines have the same meaning of Fig. 5.4.c with $\xi^2 = 0.15$.

of the last linear ramp. Step (d) modifies the double-well confinement. In particular, as it decreases the value of the rf dressing amplitude, it also decreases the height of the barrier, thus bringing the left and right wells closer to each other. (add simulation values). Finally, in Fig. 6.3.e we switch off the trap and the same free fall and detection stages as in Section 4.2.3 follow. We here performed only an interference type of measurement.

The expected outcome of the measurement is the DTB state of Eq. (4.14)

The analysis of the data starts with background and etaloning correction of each image, as in Section 4.4.1. We then center ellipses with semi-axes size of 55×10 pxl^2 on the DTB signal, two for each m_F state[1]. In Fig. 6.4.a we show the averaged image in a logarithmic scale in dB units referred to the brightest pixel. We superimposed ellipses (black curves) around the DTB emission that define the integration regions to count the twin atoms on the same image. From the fluorescence signal difference between the momentum states $\hat{s} = \hat{S}_1 - \hat{S}_2$ we can plot a histogram, as shown in Fig. 6.4.b. The lines have the same meaning as in Fig. 5.4.c. In particular, the noise corrected squeezing parameter for this data set was $\xi^2 = 0.15 \pm 0.05$, so the emission statistics are sub-binomial as expected.

We now look at the atom-atom correlation analysis of Section 4.6, similarly to what already discussed in Section 5.3.2. In Fig. 6.5.b, we show the product of the averaged profiles $\langle n_1 \rangle \cdot \langle n_2 \rangle$, where $n_1 = n(k_y, -k_0)$ and $n_2 = n(k_y, +k_0)$ are also separately plotted in Fig. 6.5.(a,d). In Fig. 6.5.c we plot the $G^{(2)}(k_y, k'_y)$ profile. This time the experimental pattern is not reminiscent of the anti-diagonal fringe in Fig. 4.15, but can

[1] We excluded the lowest m_F as it gave rise to negligible DTB signal.

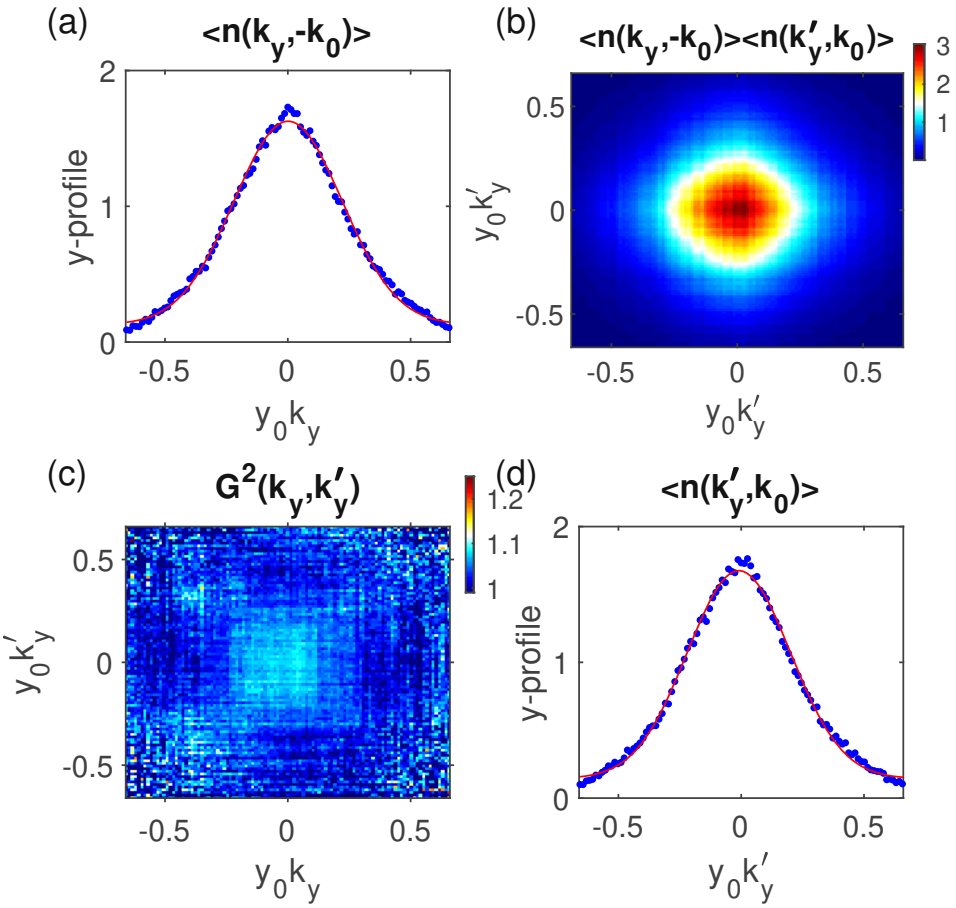

Figure 6.5: Second order correlation function $G^{(2)}(k_y, k'_y)$ of atomic profiles within twin pairs as a function of transverse momentum after long time-of-flight. (a) Averaged atomic profile relative to the atoms within the twin pairs with longitudinal momentum $-k_0$. (b) Product of the averaged atomic profiles from the two different longitudinal momentum classes $\pm k_0$. (c) Second order correlation $G^{(2)}(k_y, k'_y)$. The axes are re-scaled by the half inter-well distance $2y_0 = 1.3$ μm. (d) Averaged atomic profile relative to the atoms within the twin pairs with longitudinal momentum $+k_0$.

be related to an admixture with other states as expected by.. (see Igor's calculations).

To compare theory with experiment, we assume two density matrices ρ_3 and ρ_4 which in the $\{L, R\}$ basis representation are given by:

$$\rho_3 = \frac{1}{4}\begin{pmatrix} 1 & 0 & 0 & 1 \\ 0 & 1 & 1 & 0 \\ 0 & 1 & 1 & 0 \\ 1 & 0 & 0 & 1 \end{pmatrix}, \quad \rho_4 = \frac{1}{4}\begin{pmatrix} 1 & 0 & 0 & 1 \\ 0 & 1 & 0.5 & 0 \\ 0 & 0.5 & 1 & 0 \\ 1 & 0 & 0 & 1 \end{pmatrix}. \tag{6.16}$$

Both density matrices include LR and RL populations and some coherence terms, but in ρ_4 the contribution of the coherence terms $RLLR$ and $LRRL$ to the total state is smaller than in ρ_3 (half value). Knowing the density matrices, we then apply Eq. (4.36) to find the corresponding theoretical $G^{(2)}_{th}$ pattern. In Fig. 6.6, we compare the theoretical $G^{(2)}_{th}$ patterns related to the ρ_3 and ρ_4 matrices [(Fig. 6.6.(a,b)], with the experimental $G^{(2)}_{exp}$ pattern obtained from the analysis of the current data set

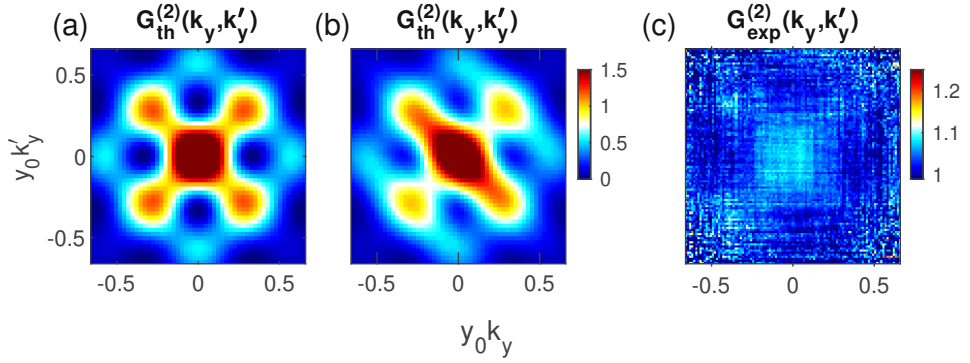

Figure 6.6: Second order correlation function $G^{(2)}(k_y, k'_y)$: theory vs experiment comparison. (a) Simulated $G^{(2)}_{th}(k_y, k'_y)$ pattern that assumes a density matrix ρ_3 (see text), computed via Eq. (4.36). (b) Simulated $G^{(2)}_{th}(k_y, k'_y)$ pattern that assumes a density matrix ρ_4. (c) Experimental $G^{(2)}_{exp}(k_y, k'_y)$ pattern evaluated from Eq. (5.14) using the experimental atomic profiles relative to this data set.

(Fig. 6.6.c). The experimental pattern shown in Fig. 6.6.c is somewhat reminiscent of the $G^{(2)}$ pattern of Fig. 6.6.a relative to the state ρ_3 in Eq. (6.16). However, any more quantitative statement would require a much higher contrast.

6.4 Conclusions

Our experiments show a path toward a quantitative demonstration of entanglement for propagating atom beams as proposed in [18]. To achieve this goal, we would need to increase the contrast of the two-particle interference significantly. We believe that the loss of visibility is due to the superposition of different $G^{(2)}$ patterns linked to the multi-pair states produced in the current regime.
A limit worth mentioning is that of very low emission. On average, in this case, much less than one atom pair is produced at every round, and the contribution from other multi-pair states is negligible. Unfortunately, the current detection scheme does not allow exploring this case due to the poor signal-to-noise ratio in the single-atom detection regime. A newer EMCCD camera should be installed that can detect single atoms.
As shown in the modified procedure, we can manipulate our state by increasing the tunneling coupling within the double-well. We also believe it is possible to apply a phase shift to the propagating DTBs by tilting the double-well potential to introduce an energy difference between the left and right well states, as in [73]. As an alternative procedure, one could implement Bragg deflectors as in [16, 20] to rotate the state after its generation. Furthermore, we explored only a few procedures to emit double twin-atom beams. The method implemented in Section 6.3 shows a hint of possible engineering of an atom Bell state since the original DTB state was rotated by a simple modification of the double-well confinement, which could lead to more sophisticated procedures to generate, modify and detect any two-particle state in the left and right basis in the near future. In particular, optimal control techniques could open doors to more advanced state manipulation.
As a more general outlook, we see a huge potential in exploring non-linear matter-wave optics for atoms propagating in waveguides and integrated matter-wave circuits. The processes behind the twin-atom emission are closely related to the matter-

wave equivalents of parametric amplification and four-wave mixing. We envision the development of non-linear matter-wave quantum optics where, possibly, the creation of entangled atom-laser beams in twin-beam emission above the threshold would be one directly accessible example.

Publications

The following publication is related to this thesis:

- Borselli, F., Maiwöger, M., Zhang, T., Haslinger, P., Mukherjee, V., Negretti, A., Montangero, M., Calarco, T., Mazets, I., Bonneau, M., Schmiedmayer, J. (2021). Two-particle interference with double twin-atom beams. Physical Review Letters, 126(8), 083603.

Bibliography

[1] Ryszard Horodecki, Paweł Horodecki, Michał Horodecki, and Karol Horodecki. Quantum entanglement. *Reviews of modern physics*, 81(2):865, 2009.

[2] Michael A Nielsen and Isaac Chuang. Quantum computation and quantum information, 2002.

[3] Albert Einstein, Boris Podolsky, and Nathan Rosen. Can quantum-mechanical description of physical reality be considered complete? *Physical review*, 47(10):777, 1935.

[4] Remi Geiger and Michael Trupke. Proposal for a quantum test of the weak equivalence principle with entangled atomic species. *Physical Review Letters*, 120(4):043602, 2018.

[5] Antonio Acín, Immanuel Bloch, Harry Buhrman, Tommaso Calarco, Christopher Eichler, Jens Eisert, Daniel Esteve, Nicolas Gisin, Steffen J Glaser, Fedor Jelezko, et al. The quantum technologies roadmap: a european community view. *New Journal of Physics*, 20(8):080201, 2018.

[6] Vittorio Giovannetti, Seth Lloyd, and Lorenzo Maccone. Advances in quantum metrology. *Nature photonics*, 5(4):222–229, 2011.

[7] Luca Pezze, Augusto Smerzi, Markus K Oberthaler, Roman Schmied, and Philipp Treutlein. Quantum metrology with nonclassical states of atomic ensembles. *Reviews of Modern Physics*, 90(3):035005, 2018.

[8] Sheila Elizabeth Dwyer. *Quantum noise reduction using squeezed states in LIGO*. PhD thesis, Massachusetts Institute of Technology, 2013.

[9] Catxere A Casacio, Lars S Madsen, Alex Terrasson, Muhammad Waleed, Kai Barnscheidt, Boris Hage, Michael A Taylor, and Warwick P Bowen. Quantum-enhanced nonlinear microscopy. *Nature*, 594(7862):201–206, 2021.

[10] Gerd Leuchs and Dagmar Bruss. *Quantum information: from foundations to quantum technology applications*. John Wiley & Sons, 2019.

[11] H Jeff Kimble. The quantum internet. *Nature*, 453(7198):1023–1030, 2008.

[12] Johannes Kofler, Mandip Singh, Maximilian Ebner, Michael Keller, Mateusz Kotyrba, and Anton Zeilinger. Einstein-podolsky-rosen correlations from colliding bose-einstein condensates. *Physical Review A*, 86(3):032115, 2012.

[13] KV Kheruntsyan, J-C Jaskula, P Deuar, Marie Bonneau, Guthrie B Partridge, Josselin Ruaudel, Raphaël Lopes, Denis Boiron, and Christoph I Westbrook. Violation of the cauchy-schwarz inequality with matter waves. *Physical review letters*, 108(26):260401, 2012.

[14] Raphael Lopes, Almazbek Imanaliev, Alain Aspect, Marc Cheneau, Denis Boiron, and Christoph I Westbrook. Atomic hong–ou–mandel experiment. *Nature*, 520(7545):66–68, 2015.

[15] Jan Peise, I Kruse, K Lange, Bernd Lücke, Luca Pezzè, Jan Arlt, Wolfgang Ertmer, Klemens Hammerer, Luis Santos, Augusto Smerzi, et al. Satisfying the einstein–podolsky–rosen criterion with massive particles. *Nature communications*, 6(1):1–8, 2015.

[16] Pierre Dussarrat, Maxime Perrier, Almazbek Imanaliev, Raphael Lopes, Alain Aspect, Marc Cheneau, Denis Boiron, and Christoph I Westbrook. Two-particle four-mode interferometer for atoms. *Physical review letters*, 119(17):173202, 2017.

[17] DK Shin, BM Henson, SS Hodgman, Tomasz Wasak, J Chwedeńczuk, and AG Truscott. Bell correlations between spatially separated pairs of atoms. *Nature communications*, 10(1):1–7, 2019.

[18] Marie Bonneau, William J Munro, Kae Nemoto, and Jörg Schmiedmayer. Characterizing twin-particle entanglement in double-well potentials. *Physical Review A*, 98(3):033608, 2018.

[19] J.-C. Jaskula, M. Bonneau, G. B. Partridge, V. Krachmalnicoff, P. Deuar, K. V. Kheruntsyan, A. Aspect, D. Boiron, and C. I. Westbrook. Sub-poissonian number differences in four-wave mixing of matter waves. *Phys. Rev. Lett.*, 105:190402, Nov 2010.

[20] Robert J Lewis-Swan and KV Kheruntsyan. Proposal for a motional-state bell inequality test with ultracold atoms. *Physical Review A*, 91(5):052114, 2015.

[21] Wolfgang Pauli. On the connection between the completion of electron groups in an atom with the complex structure of spectra. *Zeitschrift für Physik*, 31:765, 1925.

[22] Louis De Broglie. *Recherches sur la théorie des quanta*. PhD thesis, Migration-université en cours d'affectation, 1924.

[23] Claude Cohen-Tannoudji and David Guéry-Odelin. Advances in atomic physics: an overview. 2011.

[24] Pierre C Hohenberg. Existence of long-range order in one and two dimensions. *Physical Review*, 158(2):383, 1967.

[25] Vanderlei Bagnato and Daniel Kleppner. Bose-einstein condensation in low-dimensional traps. *Physical Review A*, 44(11):7439, 1991.

[26] Franco Dalfovo, Stefano Giorgini, Lev P Pitaevskii, and Sandro Stringari. Theory of bose-einstein condensation in trapped gases. *Reviews of modern physics*, 71(3):463, 1999.

[27] Mike H Anderson, Jason R Ensher, Michael R Matthews, Carl E Wieman, and Eric A Cornell. Observation of bose-einstein condensation in a dilute atomic vapor. *science*, 269(5221):198–201, 1995.

[28] Kendall B Davis, M-O Mewes, Michael R Andrews, Nicolaas J van Druten, Dallin S Durfee, DM Kurn, and Wolfgang Ketterle. Bose-einstein condensation in a gas of sodium atoms. *Physical review letters*, 75(22):3969, 1995.

[29] N Bogoliubov. On the theory of superfluidity. *J. Phys*, 11(1):23, 1947.

[30] DS Petrov, Dimitri M Gangardt, and Gora V Shlyapnikov. Low-dimensional trapped gases. In *Journal de Physique IV (Proceedings)*, volume 116, pages 5–44. EDP sciences, 2004.

[31] Fabrice Gerbier. Quasi-1d bose-einstein condensates in the dimensional crossover regime. *EPL (Europhysics Letters)*, 66(6):771, 2004.

[32] Maxim Olshanii. Atomic scattering in the presence of an external confinement and a gas of impenetrable bosons. *Physical review letters*, 81(5):938, 1998.

[33] Christophe Mora and Yvan Castin. Extension of bogoliubov theory to quasi-condensates. *Physical Review A*, 67(5):053615, 2003.

[34] Isabelle Bouchoule, Karen V Kheruntsyan, and GV Shlyapnikov. Interaction-induced crossover versus finite-size condensation in a weakly interacting trapped one-dimensional bose gas. *Physical Review A*, 75(3):031606, 2007.

[35] MD Lee, SA Morgan, and K Burnett. The gross-pitaevskii equation and higher order theories in one-dimensional bose gases. *arXiv preprint cond-mat/0305416*, 2003.

[36] EGM Van Kempen, SJJMF Kokkelmans, DJ Heinzen, and BJ Verhaar. Interisotope determination of ultracold rubidium interactions from three high-precision experiments. *Physical review letters*, 88(9):093201, 2002.

[37] Jun John Sakurai and Eugene D Commins. Modern quantum mechanics, revised edition, 1995.

[38] R Ghosh and Leonard Mandel. Observation of nonclassical effects in the interference of two photons. *Physical Review Letters*, 59(17):1903, 1987.

[39] Daniel M Greenberger, Mike A Horne, and Anton Zeilinger. Multiparticle interferometry and the superposition principle. *Physics Today*, 46:22–22, 1993.

[40] Robert Bücker, Julian Grond, Stephanie Manz, Tarik Berrada, Thomas Betz, Christian Koller, Ulrich Hohenester, Thorsten Schumm, Aurélien Perrin, and Jörg Schmiedmayer. Twin-atom beams. *Nature Physics*, 7(8):608–611, 2011.

[41] Robert Bücker, Aurélien Perrin, Stephanie Manz, Thomas Betz, Ch Koller, Thomas Plisson, Jörg Rottmann, Thorsten Schumm, and Jörg Schmiedmayer. Single-particle-sensitive imaging of freely propagating ultracold atoms. *New Journal of Physics*, 11(10):103039, 2009.

[42] John S Bell. On the einstein podolsky rosen paradox. *Physics Physique Fizika*, 1(3):195, 1964.

[43] Alain Aspect, Jean Dalibard, and Gérard Roger. Experimental test of bell's inequalities using time-varying analyzers. *Physical review letters*, 49(25):1804, 1982.

[44] Wolfgang Tittel, Jürgen Brendel, Hugo Zbinden, and Nicolas Gisin. Violation of bell inequalities by photons more than 10 km apart. *Physical Review Letters*, 81(17):3563, 1998.

[45] Gregor Weihs, Thomas Jennewein, Christoph Simon, Harald Weinfurter, and Anton Zeilinger. Violation of bell's inequality under strict einstein locality conditions. *Physical Review Letters*, 81(23):5039, 1998.

[46] Daniel Salart, Augustin Baas, Cyril Branciard, Nicolas Gisin, and Hugo Zbinden. Testing the speed of 'spooky action at a distance'. *Nature*, 454(7206):861–864, 2008.

[47] Marissa Giustina, Marijn AM Versteegh, Sören Wengerowsky, Johannes Handsteiner, Armin Hochrainer, Kevin Phelan, Fabian Steinlechner, Johannes Kofler, Jan-Åke Larsson, Carlos Abellán, et al. Significant-loophole-free test of bell's theorem with entangled photons. *Physical review letters*, 115(25):250401, 2015.

[48] Lynden K Shalm, Evan Meyer-Scott, Bradley G Christensen, Peter Bierhorst, Michael A Wayne, Martin J Stevens, Thomas Gerrits, Scott Glancy, Deny R Hamel, Michael S Allman, et al. Strong loophole-free test of local realism. *Physical review letters*, 115(25):250402, 2015.

[49] Mohammad Lamehi-Rachti and Wolfgang Mittig. Quantum mechanics and hidden variables: A test of bell's inequality by the measurement of the spin correlation in low-energy proton-proton scattering. *Physical Review D*, 14(10):2543, 1976.

[50] Mary A Rowe, David Kielpinski, Volker Meyer, Charles A Sackett, Wayne M Itano, Christopher Monroe, and David J Wineland. Experimental violation of a bell's inequality with efficient detection. *Nature*, 409(6822):791–794, 2001.

[51] Bas Hensen, Hannes Bernien, Anaïs E Dréau, Andreas Reiserer, Norbert Kalb, Machiel S Blok, Just Ruitenberg, Raymond FL Vermeulen, Raymond N Schouten, Carlos Abellán, et al. Loophole-free bell inequality violation using electron spins separated by 1.3 kilometres. *Nature*, 526(7575):682–686, 2015.

[52] Wenjamin Rosenfeld, Daniel Burchardt, Robert Garthoff, Kai Redeker, Norbert Ortegel, Markus Rau, and Harald Weinfurter. Event-ready bell test using entangled atoms simultaneously closing detection and locality loopholes. *Physical review letters*, 119(1):010402, 2017.

[53] Stephanie Manz. Density correlations of expanding one-dimensional bose gases. 2010.

[54] Thomas Betz. Phase correlations of coupled one-dimensional bose gases. 2011.

[55] Robert Bücker. *Fluorescence imaging of ultracold atoms*. PhD thesis, Diploma thesis, Heidelberg, 2008.

[56] Robert Bücker. *Twin-atom beam generation in a one-dimensional Bose gas*. PhD thesis, Techische Universität Wien, 2013.

[57] Tarik Berrada. *Mach-Zehnder interferometry with interacting Bose-Einstein condensates in a double-well potential*. PhD thesis, 2014.

[58] Daniel Adam Steck. Rubidium 87 d line data. 2001.

[59] Igor Lesanovsky, Thorsten Schumm, S Hofferberth, L Mauritz Andersson, Peter Krüger, and Jörg Schmiedmayer. Adiabatic radio-frequency potentials for the coherent manipulation of matter waves. *Physical Review A*, 73(3):033619, 2006.

[60] Thorsten Schumm, S Hofferberth, L Mauritz Andersson, Stefan Wildermuth, Steffen Groth, I Bar-Joseph, Jörg Schmiedmayer, and Peter Krüger. Matter-wave interferometry in a double well on an atom chip. *Nature physics*, 1(1):57–62, 2005.

[61] S Wildermuth, P Krüger, C Becker, M Brajdic, S Haupt, A Kasper, R Folman, and J Schmiedmayer. Optimized magneto-optical trap for experiments with ultracold atoms near surfaces. *Physical Review A*, 69(3):030901, 2004.

[62] Ron Folman, Peter Kruger, Jörg Schmiedmayer, Johannes Denschlag, and Carsten Henkel. Microscopic atom optics: from wires to an atom chip. *arXiv preprint arXiv:0805.2613*, 2008.

[63] S Hofferberth, Igor Lesanovsky, B Fischer, J Verdu, and Jörg Schmiedmayer. Radiofrequency-dressed-state potentials for neutral atoms. *Nature Physics*, 2(10):710–716, 2006.

[64] David A Smith, Simon Aigner, Sebastian Hofferberth, Michael Gring, Mauritz Andersson, Stefan Wildermuth, Peter Krüger, Stephan Schneider, Thorsten Schumm, and Jörg Schmiedmayer. Absorption imaging of ultracold atoms on atom chips. *Optics express*, 19(9):8471–8485, 2011.

[65] RJ Lewis-Swan and KV Kheruntsyan. Atomic twin beams and violation of a motional-state bell inequality from a phase-fluctuating quasicondensate source. *Physical Review A*, 101(4):043615, 2020.

[66] Tommaso Caneva, Tommaso Calarco, and Simone Montangero. Chopped random-basis quantum optimization. *Phys. Rev. A*, 84:022326, Aug 2011.

[67] Daniel F Walls and Gerard J Milburn. *Quantum optics*. Springer Science & Business Media, 2007.

[68] Tommaso Caneva, Tommaso Calarco, and Simone Montangero. Chopped random-basis quantum optimization. *Phys. Rev. A*, 84:022326, 2011.

[69] Sandrine van Frank, Antonio Negretti, Tarik Berrada, Robert Bücker, Simone Montangero, J-F Schaff, Thorsten Schumm, Tommaso Calarco, and Jörg Schmiedmayer. Interferometry with non-classical motional states of a bose–einstein condensate. *Nature communications*, 5(1):1–6, 2014.

[70] Sandrine van Frank, Marie Bonneau, Jörg Schmiedmayer, Sebastian Hild, Christian Gross, Marc Cheneau, Immanuel Bloch, Thomas Pichler, Antonio Negretti, Thommaso Calarco, et al. Optimal control of complex atomic quantum systems. *Scientific reports*, 6:34187, 2016.

[71] Igor Lesanovsky, Thorsten Schumm, S Hofferberth, L Mauritz Andersson, Peter Krüger, and Jörg Schmiedmayer. Adiabatic radio-frequency potentials for the coherent manipulation of matter waves. *Physical Review A*, 73(3):033619, 2006.

[72] GJ Milburn, J Corney, Ewan M Wright, and DF Walls. Quantum dynamics of an atomic bose-einstein condensate in a double-well potential. *Physical Review A*, 55(6):4318, 1997.

[73] Marine Pigneur, Tarik Berrada, Marie Bonneau, Thorsten Schumm, Eugene Demler, and Jörg Schmiedmayer. Relaxation to a phase-locked equilibrium state in a one-dimensional bosonic josephson junction. *Physical review letters*, 120(17):173601, 2018.

[74] Bo Zhao, Zeng-Bing Chen, Jian-Wei Pan, Jörg Schmiedmayer, Alessio Recati, Grigory E Astrakharchik, and Tommaso Calarco. High-fidelity entanglement via molecular dissociation in integrated atom optics. *Physical Review A*, 75(4):042312, 2007.

[75] Marine Pigneur. *Non-equilibrium Dynamics of Tunnel-Coupled Superfluids: Relaxation to a Phase-Locked Equilibrium State in a One-Dimensional Bosonic Josephson Junction*. Springer Nature, 2020.

[76] AG Basden, CA Haniff, and CD Mackay. Photon counting strategies with low-light-level ccds. *Monthly notices of the royal astronomical society*, 345(3):985–991, 2003.

[77] F Borselli, M Maiwöger, T Zhang, P Haslinger, V Mukherjee, A Negretti, S Montangero, T Calarco, I Mazets, M Bonneau, and J. Schmiedmayer. Two-particle interference with double twin-atom beams. *Physical Review Letters*, 126(8):083603, 2021.